Advances in Edge-Diffraction Modeling for Virtual-Acoustic Simulations

Paul Thomas Calamia

A Dissertation
Presented to the Faculty
of Princeton University
in Candidacy for the Degree
of Doctor of Philosophy

Recommended for Acceptance
By the Department of
Computer Science

Advisor: Thomas Funkhouser

June 2009

Abstract

In recent years there has been growing interest in modeling sound propagation in complex, three-dimensional (3D) virtual environments. With diverse applications for the military, the gaming industry, psychoacoustics researchers, architectural acousticians, and others, advances in computing power and 3D audio-rendering techniques have driven research and development aimed at closing the gap between the auralization and visualization of virtual spaces. To this end, this thesis focuses on improving the physical and perceptual realism of sound-field simulations in virtual environments through advances in edge-diffraction modeling.

To model sound propagation in virtual environments, acoustical simulation tools commonly rely on geometrical-acoustics (GA) techniques that assume asymptotically high frequencies, large flat surfaces, and infinitely thin ray-like propagation paths. Such techniques can be augmented with diffraction modeling to compensate for the effect of surface size on the strength and directivity of a reflection, to allow for propagation around obstacles and into shadow zones, and to maintain sound-field continuity across reflection and shadow boundaries. Using a time-domain, line-integral formulation of the Biot-Tolstoy-Medwin (BTM) diffraction expression, this thesis explores various aspects of diffraction calculations for virtual-acoustic simulations.

Specifically, we first analyze the periodic singularity of the BTM integrand and describe the relationship between the singularities and higher-order reflections within wedges with open angle less than 180°. Coupled with analytical approximations for the BTM expression, this analysis allows for accurate numerical computations and a continuous sound field in the vicinity of an arbitrary wedge geometry insonified by a point source. Second, we describe an edge-subdivision strategy that allows for fast diffraction calculations with low error relative to a numerically more accurate solution. Third, to address the considerable increase in propagation paths due to diffraction, we describe a simple procedure for identifying and culling insignificant diffraction components during a virtual-acoustic simulation. Finally, we present a novel method to find GA components using diffraction parameters that ensures continuity at reflection and shadow boundaries.

Acknowledgments

This thesis is the product of contributions from many people, and I hope to acknowledge everyone that has helped or participated in the process that got me to this point. My sincere apologies to anyone whom I have forgotten.

First and foremost I would like to thank Tom Funkhouser for his advising, mentoring, and patience. My path through Princeton was long, and I doubt it was the one that he expected, but I am grateful for his constant input and support. Many, many thanks to Peter Svensson, who is not only a member of my committee but has become a great friend and colleague as well over the course of my doctoral studies. I am also grateful to Perry Cook for his support and interest in my work, and to Szymon Rusinkiewicz and Adam Finkelstein for participating in my committee and providing valuable feedback. I regret that my short stay at Princeton prevented me from working with and learning more from them.

Starting graduate studies in computer science ten years after my last undergraduate CS class was difficult, and I doubt I would have made it through my first years at Princeton without the help and friendship of my classmates in the Graphics and Sound Group. Many thanks to Benedict Brown, Nathaniel Dirkson, Matthew Hibbs, Misha Kazhdan, Jason Lawrence, Digeo Nehab, Joshua Podolak, Phil Shilane, and Ge Wang.

During my thirteen months in Trondheim, the acoustics community (the Acoustics Group in the Dept. of Electronics and Telecommunications, SINTEF, and the Centre for Quantifiable Quality of Service in Communication Systems) at NTNU made my stay both enjoyable and stimulating. Tusen tak til Profs. Hefeng Dong, Jens Hovem, Ulf Krisitiansen, Peter Svensson (again), Jan Tro, and Erik Vigran, Drs. Odd Pettersen and Gunnar Taraldsen, and Aslak Bjerkvik, Snorre Farner, Viggo Henriksen, Nao Hodoshima, Arne Jenssen, Magne Larsen, Audun Solvang, Bård Støfringsdal, and Sigurd Saue. Dawn Behne also became a good friend and was a constant source of support and insight into the Norwegian way of life. I hope I can return their hospitality some day.

Parts of this thesis were done in collaboration with Tom Funkhouser, Ben Markham, and Peter Svensson, and to them I am particularly grateful. In addition, I have had the pleasure of interacting with a number of people active in related research over the last seven years, and I would like to thank Tapio Lokki, Ville Pulkki, Jason

Summers, Rendell Torres, and Nicolas Tsingos for helpful comments, critiques, and stimulating discussions. From my time at Rensselaer Polytechnic Institute, I would like to thank Jonas Braasch for being a good friend and colleague, as well as Joseph Digerness, Ben Markham, and Cheuk Wa Yuen who made my advising duties particularly rewarding.

Funding is of course a critical aspect of any graduate work, and for financial support I am indebted to the Department of Computer Science for a one-year fellowship, the Norway-America Association for two Norwegian Marshall Fund Awards during my stay at NTNU, and the National Science Foundation (grant CCR-0093343).

Support and love from my family have been constant throughout this process and critical to its success. My father and sister have always been there to lean on and complain to when times were tough, and provided praise when things went well, probably more than I deserved. I can't thank my wonderful wife Kimberley enough; she has borne the good and the bad with endless patience and made innumerable sacrifices during this journey. And finally, thank you to my beautiful daughter Amelie who never fails to bring a smile to my face.

Thank you all.

For Amelie

Contents

Abstract iii

1 Introduction **1**

1.1 Research Context 1

1.2 Contributions 4

1.3 Outline 5

2 Background and Related Work **6**

2.1 Modeling Techniques 6

2.1.1 Wave-Based Techniques 7

2.1.2 Geometrical-Acoustics Techniques 9

2.1.3 Hybrid Methods 14

2.1.4 Validation 15

2.1.5 Auralization: Software and Systems 17

2.2 Edge Diffraction 17

2.2.1 Exact Methods 18

2.2.2 Approximate and Asymptotic Methods 19

2.2.3 Diffraction Modeling in Room Acoustics 20

3 The Biot-Tolstoy-Medwin Diffraction Formulation **23**

3.1 Introduction 23

3.2 The Original Biot-Tolstoy Diffraction Expression 24

3.3 Medwin's Modifications 26

3.4 The Line-Integral Formulation 27

3.5 From Continuous Time to Discrete Time 29

3.6 A Frequency-Domain Formulation 30

3.6.1 Previous Frequency-Domain BTM Expressions 31

3.6.2 The Line-Integral Frequency-Domain Formulation 31

3.6.3 Relationship to the Contour-Integral Solution for the Infinite Wedge . . . 32
3.6.4 Sample Calculations . . . 35
3.7 Numerical and Experimental Validation . . . 38
3.7.1 Comparison to Measurements . . . 38
3.7.2 Comparison to Other Numerical Techniques . . . 42
3.8 Limitations . . . 42

4 Diffraction Singularities at Reflection and Shadow Boundaries 44
4.1 Introduction . . . 44
4.2 Singular Behavior of the Diffraction Integrand . . . 45
4.2.1 Singularities Related to the Direct Sound and First-Order Specular Reflections . . . 45
4.2.2 Singularities Related to Higher-Order Specular Reflections . 47
4.2.3 Example Calculations . . . 49
4.3 Analytical Approximations to Address Zone-Boundary Singularities 52
4.3.1 Approximating the Diffraction Integrand . . . 52
4.3.2 Limits of Integration . . . 53
4.3.3 Approximation for the Symmetric Case . . . 54
4.3.4 Approximation for the Asymmetric Case . . . 55
4.3.5 Limit Value for the Approximations . . . 57
4.3.6 Application of the Approximation to the Frequency-Domain Formulation . . . 58
4.4 Summary . . . 59

5 Reducing Diffraction Computation Time with Edge Subdivision 61
5.1 Introduction . . . 61
5.2 Edge Subdivision Strategies . . . 62
5.2.1 Subdivision into Sample-Aligned Segments . . . 62
5.2.2 Subdivision into Evenly Sized Segments . . . 64
5.2.3 Hybrid Subdivision Strategy . . . 66
5.3 Calculation Parameters . . . 67
5.3.1 Size of the Alignment Zone . . . 67
5.3.2 Segment Size . . . 67
5.3.3 Numerical Integration Technique . . . 68
5.4 Results . . . 68

5.4.1 Calculations for a Single Edge . . . 68
5.4.2 Calculations for an Array of Rectangular Panels . . . 70
5.5 Summary . . . 74

6 Diffraction Culling in Virtual-Acoustic Simulations 77
6.1 Introduction . . . 77
6.2 Methodology . . . 80
6.2.1 Simulation Scenarios . . . 80
6.3 Culling by Amplitude Rank . . . 83
6.3.1 Hall 1: Visible Sources on Stage . . . 85
6.3.2 Hall 2: Occluded Sources in the Pit . . . 90
6.4 Culling by Proximity to a Zone Boundary . . . 93
6.4.1 Hall 1: Visible Sources on Stage . . . 96
6.4.2 Hall 2: Occluded Sources in the Pit . . . 99
6.5 Discussion . . . 102
6.6 Summary . . . 104

7 Integration of Edge Diffraction and Geometrical-Acoustics Modeling 106
7.1 Introduction . . . 106
7.2 Integrated Modeling Approach . . . 107
7.2.1 Direct-Sound Occlusions . . . 108
7.2.2 First-Order Specular Reflections . . . 109
7.3 Discussion . . . 114
7.3.1 Accuracy . . . 114
7.3.2 Efficiency . . . 115
7.4 Summary . . . 115

8 Conclusions and Future Work 116
8.1 Summary of Contributions . . . 116
8.2 Future Work . . . 118
8.2.1 Direct Extensions of This Thesis . . . 118
8.2.2 Novel Simulation Techniques . . . 119

Bibliography 122

List of Figures

3.1 Infinite 3D wedge geometry and cylindrical coordinate system. . . . 24
3.2 Finite 3D wedge geometry and cylindrical coordinate system. 28
3.3 2D view of sample-aligned edge segments. 30
3.4 Geometry for the frequency-domain BTM example calculations. . . 35
3.5 Numerical validation of the frequency-domain BTM formulation. . . 36
3.6 Comparison of time-domain and frequency-domain BTM calculations for a finite edge. 37
3.7 Variation of diffration magnitude spectrum with edge length. 38

4.1 Example geometry for the four basic singularity cases. 46
4.2 Onset diffraction amplitude as a function of the receiver angle. . . . 50
4.3 Example geometry showing the behavior at a second-order reflection boundary. 51
4.4 Impulse responses for the example in Figure 4.3. 51

5.1 Sample-aligned edge subdivision. 63
5.2 Example values used for multi-sample distribution. 64
5.3 Multi-sample distribution with and without slope correction. 65
5.4 2D view of hybrid edge subdivision. 66
5.5 Results for the single-edge subdivision example. 69
5.6 Panel-array geometry used to evaluate hybrid edge-subdivision. . . 71
5.7 Maximum spectral error for various hybrid subdivision cases. 73
5.8 Impulse responses for the panel-array example. 75
5.9 Spectra and spectral error for the panel-array example. 76

6.1 Growth in propagation paths due to diffraction. 78
6.2 Geometry of Hall 1 with no interior occlusions. 81
6.3 Geometry of Hall 2 with occluded sources in the orchestra pit. . . . 82

6.4 Relationship between diffraction ranking by maximum amplitude and by total energy. 84
6.5 Maximum spectral error over all source/recevier pairs for various rank-based culling cases in the Hall 1 model. 85
6.6 Smoothed spectra of source materials for auralization-based subjective tests. 87
6.7 Listening-test results for rank-based culling in the Hall 1 model. . . 89
6.8 Maximum spectral error over all source/recevier pairs for various rank-based culling cases in the Hall 2 model. 92
6.9 Peak diffraction amplitude as a function of the receiver angle. . . . 94
6.10 Variation in diffraction-IR onset amplitude with culling threshold. . 95
6.11 Maximum spectral error over all source/receiver pairs for various zone-boundary culling cases in the Hall 1 model. 97
6.12 Listening-test results for zone-boundary culling in the Hall 1 model. 98
6.13 Maximum spectral error over all source/receiver pairs for various zone-boundary culling cases in the Hall 2 model. 101

7.1 Finding direct-sound occlusions with diffraction parameters. 110
7.2 Confirming a specular reflection with diffraction parameters. 111
7.3 Finding the reflection point on a surface. 113

List of Tables

4.1 Geometrical-acoustics components associated with the four $\nu\varphi_i$ angles at $2n\pi$ for $n = 0, 1, 2, 3$. 48

5.1 Parameters for the 5 fastest processing times for each S/R pair with maximum spectral error less than 1 dB. 74

6.1 Responses for the subjective tests of rank-based culling. 91
6.2 Comparison of rank-based culling and zone-boundary culling for Halls 1 and 2. 96
6.3 Responses for the subjective tests of zone-boundary culling. 100

Chapter 1

Introduction

In recent years there has been growing interest in modeling sound propagation in complex, three-dimensional (3D) virtual environments. With diverse applications for the military, the gaming industry, psychoacoustics and speech researchers, architectural acousticians, and others, advances in computing power and 3D audio-rendering techniques have driven research and development aimed at closing the gap between the auralization and visualization of virtual spaces. While simulations based on accurate solutions of the wave equation still remain computationally prohibitive for many applications, current CPU speeds coupled with the use of efficient algorithms and data structures now allow for interactive simulation rates in complex virtual environments using approximate solutions.

1.1 Research Context

In the field of architectural acoustics, software for the prediction of room impulse responses and various standardized parameters extracted from them (*e.g.* Reverberation Time, Clarity, and Center Time [108]) has been available for approximately 20 years, and various programs such as CATT Acoustic [52], Odeon [38] and EASE [1] are now widely used throughout the acoustics-consulting industry to predict the acoustical characteristics of unbuilt spaces and to quantify the acoustical effects of architectural modifications in renovation projects. More recently, acousticians also have started to rely on auralizations from these programs, *i.e.* audible renderings

of simulated sound fields, to listen to unbuilt spaces and subjectively verify design decisions.

In psychoacoustic and related research, there is interest in the ability to test various human listening abilities in well defined and controlled acoustic environments. It is possible to achieve these environments through virtual-acoustic modeling: impulse responses can be computed for virtual spaces with the desired reverberation time or reflection pattern, for example, and convolved with noise, speech, or other signals for use in subjective listening tests. Such a process has been applied specifically to the study of sound localization [294], auditory target detection [296], and speech intelligibility [293] among other listening tasks, and simulation systems have been designed for general psychoacoustic experimentation as well [19, 289].

Virtual environments also can be used for training purposes, and the inclusion of accurate spatial audio in immersive simulations has been shown to provide a more complete sense of presence and realism [69]. Virtual training may be used, for example, when the real-life task or environment is impractical or too dangerous to recreate, and thus one common user of such a training technique is the military. Communication and auditory localization in adverse acoustic conditions and/or complex environments are common subjects of study, and they are addressed at numerous research facilities such as the Environment for Auditory Research that is associated with the Visual and Auditory Processes Branch of the Human Research and Engineering Directorate at the US Army Research Laboratory, and the Human Effectiveness Directorate of the US Air Force Research Laboratory.

The rapid rise in popularity of computer gaming also has played a major role in the development of technology for acoustic simulations in virtual environments. Increases in processing power coupled with the affordability and popularity of multichannel audio systems for home theater have led to a dramatic increase in the desire for (and the ability to provide) complex and perceptually plausible 3D audio "soundtracks" for games. Specifications for 3D game audio are maintained by the Interactive Audio Special Interest Group of the MIDI Manufacturers Association [178], and additional resources and recommendations are provided by the Audio Engineering Society's Technical Committee on Audio for Games [10]. For game-audio programmers, Microsoft's DirectSound [177] and XAudio [176], Creative Labs' EAX (Environmental Audio eXtensions) [49], and the Open Audio Library [50] are among the various tools that provide for spatialized sound with features such as source

processing with head-related transfer functions, early reflections and reverberation based on geometric and material properties of environments, and occlusion effects for partially and/or totally obstructed direct and/or reflected propagation paths.

The process to create virtual-acoustic simulations has six main steps.[1] A user must: obtain a 3D model of the environment, perhaps through the use of a CAD program or laser scanning of an existing space, that includes material properties related to the acoustic absorption, reflection, and scattering behavior of the model's surfaces; define the characteristics of the source(s) and receiver(s) within the space, such as location, spatial extent, directivity, and spectral content; determine the valid propagation paths from each source to each receiver; construct an impulse response (IR), which encodes the arrival time, strength, spectrum, and possibly the incoming direction of the sound-field component associated with each path;[2] convolve the IR with synthesized sound or an anechoic recording; auralize the result of the convolution using loudspeakers or headphones. The end product is then an auditory event that, when the various simulation steps are carried out with sufficient accuracy, is perceptually similar to or perhaps even indistinguishable from that which would have occurred for a listener physically present in the modeled space.

Although there is significant research focused on various aspects of this simulation pipeline, of particular interest to this thesis are the third and fourth steps: determining the valid propagation paths between a source and a receiver, and constructing an impulse response from them. These paths may involve free-field propagation (the direct sound), as well as one or more instances of specular reflection, non-specular scattering, diffraction, and/or transmission through a surface. Certain simulation methods, specifically those referred to as "wave-based" techniques, can include all of these propagation phenomena, but their computational complexity, which grows prohibitively with frequency, renders them usable only for small spaces and low frequencies. As an alternative, methods based on geometrical-acoustics (GA) assumptions, *i.e.* that the acoustic wavelength is vanishingly small which allows for the simulation of the propagation of sound to mimic that of the propagation of light through the use of infinitely thin rays, are widely used where more timely results

[1] The third step, explicitly finding the propagation paths from the source to the receiver, is necessary only for certain modeling techniques, typically those based on geometrical acoustics. Wave-based techniques such as the Boundary Element method generate a transfer function or an impulse response directly without such a decomposition of the simulated sound field.

[2] It also is possible to operate in the frequency domain and construct a transfer function, which can be converted into an impulse response if necessary using the inverse Fourier transform.

are expected or needed and the associated errors are assumed to be acceptable. GA techniques do not include diffraction implicitly, and the errors associated with this omission may take various forms including incorrect strength and/or direction of reflections, or the absence of propagation around occluders and into shadow zones. It is the explicit addition of diffraction to GA techniques, with the goal of correcting these errors and improving the physical accuracy and perceptual realism of virtual-acoustic simulations, which is the main subject of this thesis.

1.2 Contributions

In this thesis we describe a number of advances related to edge-diffraction modeling within GA-based virtual-acoustic simulations. In particular, we make the following research contributions.

- First, using a line-integral edge-diffraction formulation, we explore the singular behavior of the integrand that occurs for receivers near GA reflection and shadow boundaries, and specifically describe the relationship between the periodicity of the singularity and the related GA terms. This singularity is necessary to compensate for the GA discontinuities at the boundaries and maintain sound-field continuity, and thus its proper numerical treatment is critical for physically accurate simulations.

- Second, we evaluate three edge-subdivision strategies to provide discrete-time impulse responses from continuous-time, line-integral diffraction formulations. We show that by understanding the singularities mentioned above in terms of the effect they have on the diffraction amplitude and the geometry of a source-edge-receiver diffracted path, it is possible to reduce diffraction computation times dramatically with limited error by concentrating the computational demands of more accurate numerical-integration techniques on the portion of an edge that contributes the most diffracted energy, and allow for relaxed accuracy for segments with smaller contributions.

- Third, we address the combinatorial increase in computational complexity of virtual-acoustic simulations when diffracted paths are included. Through objective and subjective analysis, we show that only a small subset of diffracted paths must be processed to maintain high levels of numerical and, with certain

source material, perceptual accuracy. In addition, we describe a method to predict the significance of diffraction components before they are fully computed, allowing the weak ones to be culled from a simulation before they are fully processed.

- Fourth, we describe a novel time-domain method for virtual-acoustic modeling that smoothly integrates GA and edge-diffraction components. Specifically, we use parameters generated for the diffraction calculations to identify surfaces that give rise to specular reflections and/or that occlude the direct-sound path. This approach is particularly well suited for use with receivers at or near reflection and shadow boundaries, where the proper combination of GA and diffraction components is essential to ensure a continuous sound field across the boundary.

1.3 Outline

The remainder of this thesis is organized as follows. Background information and related work on virtual-acoustic simulations and diffraction modeling are provided in Chapter 2. Chapter 3 outlines the development of the Biot-Tolstoy-Medwin (BTM) diffraction formulation that is used throughout this thesis, and also addresses numerical and experimental validation. Chapter 4 describes the singularities present in the BTM expression (which are common to other diffraction expressions as well) which occur for receivers at reflection and shadow boundaries, and are particularly important to the following two chapters. Chapter 5 discusses various edge-subdivision techniques that can be used to compute discrete-time diffraction impulse responses from the original continuous-time BTM expression, and Chapter 6 addresses the identification and culling of insignificant diffraction components from virtual-acoustic simulations. Chapter 7 describes a novel method to integrate edge-diffraction calculations with geometrical-acoustics modeling, and Chapter 8 provides conclusions and suggestions for future work.

Chapter 2

Background and Related Work

In order to establish the proper context for the remainder of this thesis, this chapter summarizes the related work in the field of acoustic modeling, with a particular focus on room acoustics, as well as specific methods and applications of diffraction computation. The Biot-Tolstoy-Medwin diffraction formulation, which is employed throughout the remainder of this thesis, is mentioned only briefly here but covered in detail in Chapter 3.

2.1 Modeling Techniques

Methods for simulating acoustic wave propagation are the focus of a significant body of research, and they commonly are divided into two major groups: wave-based techniques, and geometrical-acoustics (GA) techniques. The former attempt to simulate acoustic fields through numerical solutions of the wave equation, typically by means of discretization of a space or its boundaries. Such methods implicitly include the wave characteristics of sound propagation such as interference and diffraction, and thus provide a "complete" solution. However, this completeness comes with a high computational cost. The latter methods, based on geometrical acoustics, make the assumption of asymptotically high frequencies, which allows for simplified models of propagation, reflection, scattering, etc. This enables methods that provide faster solutions, but grosser approximations. An open question, partially addressed in this thesis, is how to bridge the gaps in accuracy and speed of these two simulation approaches.

2.1.1 Wave-Based Techniques

Wave-based simulation techniques, which attempt to solve the wave equation (with the necessary boundary conditions) directly through spatial and/or temporal discretization, are typically further subdivided into frequency-domain and time-domain methods (although some methods have formulations in both domains). The former includes the Finite-Element and Boundary-Element Methods (FEM and BEM, respectively), while the latter comprises the Finite-Difference Time-Domain Method (FDTD) and the Digital Waveguide Mesh (DWM) approach.

The FEM [295] and BEM [29, 42] allow for numerical solution of the wave equation (with given boundary conditions and source functions) throughout a simulation domain through discretization; the discretization allows for the underlying partial differential equation to be reformulated as a series of linear algebraic equations and solved accordingly. The FEM uses volumetric elements to discretize the domain itself, and with the typical assumption of a time-harmonic signal leads to solutions of the Helmholtz equation. The BEM employs discrete surface elements for the solution of the wave equation in the form of the Helmholtz-Kirchhoff (HK) integral equation. The HK integral is the mathematical formulation of Huygens' Principle, and gives the acoustic field at a point as a function of the pressure and normal particle velocity at the surrounding surfaces. With either the FEM or BEM, a broadband solution (transfer function) must be built up from a collection of single-frequency calculations.

For these methods, the discretization is subject to constraints based on the bandwidth of interest, with a typical rule of thumb suggesting 6 to 10 computation nodes per wavelength. The resulting matrices grow quickly with frequency, and thus for interior acoustic problems the FEM and BEM are typically restricted to small computational domains or low frequencies. Examples in room acoustics for the former are given in [48, 70, 135, 179, 200] and for the latter in [89, 209, 251]. These methods also can be used to find solutions to the exterior acoustic scattering problem, with BEM-based studies of reflecting and diffusing panels being the primary focus related to room acoustics [46, 47, 98]. A time-domain formulation of the BEM has also seen some use in 3D interior problems [66, 96] and in modeling acoustic scattering from thin, rigid plates [124] and diffusing surfaces [97].

Time-domain modeling methods are attractive for applications in room acoustics for a number of reasons. First, they allow for direct evaluation of sound fields and individual components thereof through visual inspection of an impulse response. Second, standardized room-acoustics parameters, such as reverberation time, which are used for qualitative and quantitative analysis of rooms, are extracted from impulse responses rather than transfer functions. Finally, time-domain calculations can yield high-bandwidth results without the need for multiple computation passes. Given these advantages, significant research has been applied to wave-based modeling methods that operate in the time domain, specifically the finite-difference time-domain method and the digital waveguide mesh method.

As its name suggests, the FDTD approach approximates the temporal and spatial derivatives in the wave equation with finite differences. A volumetric grid must be fit to the interior of the modeled space (with grid spacing dictated by Nyquist theorem applied to the highest frequency of interest), and the pressure time history at a specific point or points can be modeled through alternating updates of pressure and particle velocity at the grid points. While the representation of complex, broadband boundary conditions can be difficult with the FDTD method, it has been the focus of significant work in room-acoustics modeling for the past decade [27, 163, 218, 219, 220, 253].

The DWM method also involves a grid for spatial and temporal sampling of the simulated sound field. In this case, the grid is constructed with bi-directional delay lines connected with so-called "scattering junctions." These junctions are used to model the desired boundary conditions, and also serve as points at which sound pressure can be introduced to the system (*i.e.* source locations), and points at which the pressure time-history (*i.e.* impulse responses) can be monitored. The DWM method has played a prominent role as a technique for physical modeling of sound sources such as musical instruments [241] and the human voice [184], and also is well used as a tool for modeling room acoustics in 2D and 3D virtual environments [73, 121, 185, 186, 187, 226, 227, 231, 232, 278]. An excellent overview of the method and summary of related work can be found in [188].

2.1.2 Geometrical-Acoustics Techniques

Geometrical-acoustics modeling techniques are based on the assumption of asymptotically high frequencies, and as such consider sound propagation only along straight, ray-like paths. Wave/surface interactions are confined to infinitesimal points at ray/surface intersections, and simulation accuracy is achieved only when surfaces are large compared to wavelength. The simplest of GA methods include only specular reflections, but the overlap of the range of audible wavelengths with the dimensions of surfaces in typical virtual-acoustic environments, as well as the inability to model surface roughness and other fine-scale geometric details, require some form of (non-specular) wave scattering to be modeled to obtain accurate simulation results. In a recent paper, Siltanen *et al.* [238] have shown that the common GA modeling methods can be generalized with an integral "acoustic rendering" equation (in the spirit of Kajiya's rendering equation for global illumination in computer graphics [117]), but the methods are addressed separately here.

2.1.2.1 The Image-Source Method

The image-source method (ISM) involves the recursive mirroring of a sound source about the reflecting planes in a virtual environment to find valid specular reflection paths between that source and one or more receiver positions. Allen and Berkley [2] are often cited as the first to use the ISM in room acoustics (1979), although their main contribution was related to the description of a computer-based algorithm for the method rather than a truly novel application. Various authors described its use in room acoustics analysis previously, for example see [20, 90, 91, 210], and Eyring [74] employed it in the development of his classic reverberation-time formula as early as 1930.

Allen and Berkley [2] considered only rectangular rooms with real-valued, angle-independent and frequency-independent absorption coefficients (mainly to study the perception of reverberation effects on speech), and much research since has addressed these and other limitations. This includes the extension of the method to rooms of arbitrary shape [21], various techniques to improve computational efficiency [133, 139, 152, 168, 281], and simulating interference effects through the use of complex superposition [55, 249, 290].

Despite its limitations, the image-source method is arguably the most widely used GA simulation method (albeit most often as one component in a hybrid method as described in Section 2.1.3 below), particularly for modeling early reflections that are critical for perceptual accuracy, and it continues to be the subject of research. Recent enhancements to the method itself include computational acceleration with the use of binary space partitions [235] and multipole expansion [68], and further study has been applied to the prediction of reverberation time from energy-decay functions derived from ISM simulations [153, 154].

As is noted in [2] and more rigorously established elsewhere (*e.g.* see [129]), the common use of *point* image sources is strictly correct only for ideal (Neumann or Dirichlet) boundary conditions and certain geometries. For finite surfaces with exposed edges, and wedges formed by the intersection of planar surfaces, the image-source method can be combined with edge-diffraction calculations for improved accuracy, and this is discussed in depth in Chapters 3 - 7.

2.1.2.2 Ray and Particle Tracing

Ray tracing, also a popular method for image rendering in computer graphics (*e.g.* see [182]), is a GA technique used to sample the infinite number of sound propagation paths between a source and a receiver in an enclosed space. A large number of rays is released from a source, with their directions determined either deterministically or (more typically) stochastically to cover the desired source-directivity pattern, and they are traced through the geometry following linear paths between reflections from surfaces. The reflection direction can be specular, or can be determined with the use of a scattering model to simulate diffusive surfaces. Arrivals are detected with the use of finite-volume receivers due to the numerical problems associated with finding line/point intersections in 3D space.

Early use of ray tracing in room acoustics considered only specular reflections, and focused on the analysis of irregular spaces for which statistical approaches (*e.g.* predictions of reverberation time with the Sabine or Eyring equations) and modal analysis was inappropriate and/or difficult. For example, Allred and Newhouse [3, 4] described the use of ray tracing (with randomly chosen initial ray directions) to find the mean free path (mfp) of various parallelepipeds whose dimensions caused the mfp to deviate from the statistical value $4V/S$ (V = volume, S = surface

area). They also employed ray tracing to evaluate the effectiveness of absorbers as a function of the shape of a room and the absorbers' positions within it. Krokstad *et al.* [140] applied the method (with deterministic ray directions) to the analysis of early-sound distribution in halls of various shapes. In later work, Schroeder [236] discussed ray-tracing simulations in 2D spaces with specular and diffuse reflections, as well as the use of auralization based on ray-tracing results to study subjective aspects of room acoustics and reverberation. Wayman and Vanyo [286] extended Schroeder's work to 3D models, and compared reverberation times extracted from their simulations to statistical predictions and measurements in small classrooms.

Continued research in acoustic ray tracing addressed the variance of the results with changes in the number of rays used and with stochastic ray directions [141], and potential detection errors related to finite-volume receivers and inadequate spatial sampling [155]. Also considered were specific algorithmic details related to basic implementations [142] and auralization [147], as well as applications to specific room types such as "fitted" industrial spaces with numerous reflecting and scattering objects within them [199]. More recent work has addressed the effects of various receiver models on the detection of rays [114, 291], and ray-tracing implementations on computer graphics hardware [112, 216].

One benefit of ray tracing over the image-source method is the ability to include diffuse reflections, whose importance in acoustic simulations has been discussed by various researchers [54, 104, 149, 282]. Diffuse reflections caused by surface roughness, impedance changes, and/or finite surface dimensions exist in most real-world environments, but can be difficult to simulate exactly. The typical approach to model diffuse reflections in a ray-tracing context is to assign a random-incidence scattering coefficient [45, 109, 284] to each surface, and use it to direct rays in non-specular directions with the overall spatial distribution of energy obeying Lambert's Law [146]. Alternatives to this have also been described, for example by Embrechts [72] who uses the Kirchhoff approximation along with statistical roughness properties of a surface to determine the directions of diffusely reflected rays.

Various authors also have described acoustic-simulation methods based on tracing particles rather than rays. In some cases the distinction is superficial: as with ray tracing, sound particles are injected into a virtual space from a source, traced through the environment with specular and/or diffuse reflections at surfaces, and intersections of their paths are detected with a receiving volume [65, 244, 245].

However, related techniques variously known as "sonel mapping" [118, 119, 120] and "phonon tracing" [17, 61, 62, 63, 175] are based on the graphics rendering technique known as photon mapping [113]. With these methods, particle/surface intersections are stored in a spatial data structure such as a *kd*-tree. After the particle tracing is complete, rays from a receiver position are used to probe the sonel or phonon map, *i.e.* the geometry, and calculate incoming acoustic energy through estimates of the particle density near ray/surface intersections.

2.1.2.3 Beam and Cone Tracing

Like ray and particle tracing, beam and cone tracing techniques also are methods used in acoustic modeling with a history in computer graphics [100]. Rather than infinitely thin rays, volumetric beams or cones, with triangular, polygonal, or circular cross sections, are traced through a virtual environment to find propagation paths from a source to a receiver. These methods offer a number of improvements over ray tracing and the ISM. In regard to the former, they allow for the full coverage of space surrounding a source position, thus eliminating the detrimental effects of aliasing (spatial undersampling), and the finite spatial extent of beams and cones permits the use of point receivers, so false detections due to finite receiver volumes also are eliminated. In regard to the ISM, beam and cone tracing can be used to accelerate the detection of valid, visible image sources by efficiently identifying possible sequences of reflecting surfaces.

Early beam-tracing results in acoustics are due to Lewers [157], who employed triangular beams (allowing for full, non-overlapping coverage of the 4π steradians around a source) whose reflection behavior was governed by the intersection of their center axis with surfaces in the virtual environment. The surface-reflection history of each beam that intersected a receiver was used to identify visible image sources and thus valid specular reflections. A similar approach was presented by Farina [75, 76, 77, 78], although upon beam/receiver intersection he computed a beam's contribution to the simulated impulse response directly rather than search for the associated image source. Monks *et al.* [181] and Stephenson [246] used exact beam/surface intersections for trimming and splitting beams at reflecting surfaces (as did Drumm and Lam [67] somewhat later), but dealt with the associated growth in the number of beams to trace differently. The former limited their tracing to low

reflection orders, and the latter used a spatial quantization approach to "re-unify" beams with similar trajectories.

Further advances in beam tracing are described by Funkhouser *et al.* [83, 85], whose use of binary-space partitioning (similar to that used later in [235] to accelerate the ISM) and a precomputed "beam tree" data structure allow for interactive simulation rates for moving receivers. Tsingos *et al.* [271] extended this system to include edge diffraction. Antonacci *et al.* [6, 7, 8, 9] use similar data structures, along with additional precomputed visibility information based on dual-space representations of 2D or 2.5D environments, to provide interactive beam-tracing simulations with a moving source or a moving receiver. Laine [148] describes various optimization for faster beam-tracing simulations, and Chandak *et al.* [37] use hierarchical, quad-tree-based subdivision of four-sided frusta (beams) to compute approximate beam/surface intersections for fast simulations.

Cone tracing [5] with beams of circular cross section also has been employed for acoustic simulations, typically with reflections based on the interaction of a cone's center ray with reflecting surfaces. The popular commercial modeling software CATT Acoustic uses various methods including cone tracing for its calculations [52, 53, 252]. An important limitation with cone tracing is the inability to cover the full sphere around a source without gaps or overlapping cones. The former results in possible missed propagation paths and the latter with multiple detections, although this can be addressed with a Gaussian weighting across the cone faces to account for the overlap [279].

2.1.2.4 Radiosity

Radiosity [94, 237] is yet another acoustic modeling technique with parallels in computer graphics. In its original (acoustic) form it modeled only the diffuse exchange of sound energy between surface patches [144, 145]; specular reflections were omitted from acoustic radiosity simulations that generated results similar to those using ray tracing with purely diffuse (Lambertian) reflections [151]. Improvements on the basic algorithm were given by Tsingos and Gascuel [273, 274] who borrowed hierarchical patch subdivision from similar global-illumination methods [237], and by LeBot [150] who altered the underlying integral equation to include specular

reflections (apparently without knowledge of similar and earlier work in computer graphics, *e.g.* by Immel *et al.* [107] and Rushmeier and Torrance [217]).

Additional radiosity results in acoustics have been presented by Hodgson and Nosal [105, 191, 192] who describe computational enhancements, validation through comparison with analytical solutions for spherical spaces, and further comparisons to ray tracing with diffuse reflections in cubic enclosures. Muehleisen and Beamer [183] present steady-state sound-pressure level predictions based on radiosity and compare them to ray-tracing predictions and measured results from classrooms.

2.1.3 Hybrid Methods

Various aspects of the simulation methods described above suggest a hybrid approach to acoustic modeling. Accordingly, many commercial and research systems employ multiple techniques to generate accurate broadband results over long time scales. The crossover from one method to another is typically defined in terms of temporal or spectral boundaries, but also may be related to differences in reflection behavior such as that between specular and diffuse components of a sound field.

A time-based separation of simulation methods is perhaps the most common. The density of reflections in a room impulse response (IR) grows quadratically with time [147], and a distinction is often made between the sparse early reflections and the dense late reverberation [51, 283]. The former can be largely specular, and are critical for perceptual accuracy in terms of loudness and spatial aspects of a simulated sound field. Late reflections are less important to model correctly on an individual basis, and only the overall temporal, spectral, and spatial characteristics of the late reverberation portion of an IR must be simulated properly. As such, a technique such as the image-source method, perhaps accelerated with beam tracing, which guarantees the detection of all specular reflections up to a specified order, is preferred for the early reflections. Reverberation can then be modeled statistically or with ray tracing, with relaxed accuracy constraints allowing for lower computational complexity. "Temporal hybrids" of this nature are used in commercial software such as Odeon [38] and CATT Acoustic [52] as well as various research systems [156, 230]. An alternative hybridization of the ISM and ray tracing involves using the latter to acceleration detection of image sources visible from a receiver. This technique was

originally described by Vorländer [281] and has been used in numerous simulation systems [101, 189, 243].

Computational complexity is the main factor in the decision to use hybrid simulation techniques with spectral cutoffs. Wave-based methods can provide accurate results at low frequencies, but the multiple-nodes-per-wavelength and/or Nyquist requirements make high-frequency simulations impractical. This constraint has led to hybrids combining low-frequency BEM calculations with high-frequency, GA-based calculations from CATT [251], as well as combinations of DWM simulations with ray tracing [186, 233].

The final hybridization is based on the separate calculation of specular and diffuse reflections. While ray tracing, for example, can be used to simulate both, many other methods are restricted to one or the other. This has led to various combinations of the ISM or beam tracing (for specular) with radiosity (for diffuse) [67, 136, 157, 247].

2.1.4 Validation

Validation of acoustic-modeling results also has been addressed widely in the literature, typically through comparisons of parameters extracted from measured and simulated impulse responses, such as reverberation time, clarity and others defined in the ISO 3382 standard [108], rather than of the impulse responses themselves. Many such comparisons have been described, *e.g.* see [86, 93, 205, 214, 215], although a series of three "Round Robins on Room Acoustical Computer Simulation" led by the Physikalisch-Technische Bundesanstalt (PTB) Braunschweig generated the most systematic validation results for GA simulations [22, 23, 24, 25, 282].

Each of the three Round Robins addressed a different space (a speech auditorium, a concert hall, and a recording studio), and was open to participation from both developers and users of various modeling programs. Participants were provided with a modeling scenario (sometimes including only a verbal description of room dimensions and surface properties, while other times including a 3D model with specific absorption and scattering coefficients) and asked to report back with parameter values from their simulations that were compared to measured data. Accuracy (or error) was measured in terms of just-noticeable-difference limen for octave-band values of the parameters. Assuming accurate input data and a user's familiarity

and competence with the software, the conclusions reached by the PTB researchers were:

- Results at low frequencies are hindered by the lack of wave phenomena such as diffraction, as well as the lack of phase information due to the use of real-valued surface absorption coefficients rather than complex surface impedances;[1]
- Middle-frequency and high-frequency parameters can be simulated accurately, *i.e.* typically within one just-noticeable difference of measured values;
- Diffuse reflections are critical to model, and the typically used Lambertian scattering is, while physically unrealistic, sufficient for accurate parametric results;
- Increased level of geometric detail does not improve simulation results due to the high-frequency assumptions of GA modeling techniques, but intelligent use of scattering coefficients applied to large flat surfaces is sufficient to simulate the scattering effects of the missing details.

Rather than compare parameters from measurements and simulations in complex environments, Tsingos *et al.* [268] describe the validation of their beam-tracing system through the direct comparison of impulse responses obtained from a simple box geometry. Thorough measurements of surface, source, and receiver properties were also collected and incorporated into their simulations to limit the number of unknown factors affecting the results. They report high accuracy for their simulations in terms of agreement with measured IRs, although no quantitative error analysis is provided. They also show the importance of diffraction in acoustic simulations through measured and modeled IRs for a receiver occluded from the source.

Validation attempts have also been made for wave-based acoustic modeling. Sakuma *et al.* [221, 222] describe a collection of benchmark problems for wave-based simulations, accessible from a web site [262], with a round-robin comparison of results. While widespread use of the benchmarks does not seem to have occurred yet, accurate FEM and BEM results for the given interior problems have been described [123, 198].

[1]The importance of including phase in acoustic simulations is also discussed by Suh and Nelson [249].

2.1.5 Auralization: Software and Systems

Acoustic modeling may be used for a variety of purposes, some of which require the auralization, or rendering audible, of simulation results. An excellent overview of the underlying principles is given by Kleiner *et al.* [134], and a more recent survey with broad coverage of acoustic modeling and auralization has been published by Vorländer [283].

In short, and as described in Chapter 1, auralization typically involves convolving a simulated or measured impulse response with an anechoic source signal, and rendering the result through headphones or loudspeakers to reproduce the simulated or measured sound field. Ideally, this process should reproduce temporal, spectral, and spatial aspects of the sound field for a perceptually accurate, immersive auditory experience. Capturing and reproducing the spatial characteristics of a sound field are topics of considerable current interest, for example with the development and use of spherical microphone arrays [56, 95, 174, 196, 206], and various 3D rendering techniques [57, 173].

Auralization is carried out with simulated IRs by commercially available room-acoustic modeling programs such as CATT Acoustic [52], Odeon [38, 189] and EASE/EARS [1, 234]. In addition, various other systems also exist for virtual acoustic simulations and auralization, with applications in psychoacoustics research [19, 289], military training [81], and research in virtual reality [156, 228, 230].

Auralization of diffraction also has been discussed by Torres *et al.* [265] and Tsingos *et al.* [271]. In addition, the diffraction modeling results described in later chapters of this thesis have been subject to limited perceptual evaluation through simple auralization with omni-directional impulse responses (see Sections 6.3.1.2 and 6.4.1.2).

2.2 Edge Diffraction

Edge-diffraction is a common component in studies of acoustic wave propagation. Both interior and exterior problems can contain geometry, such as multi-scale roughness or source-occluding surfaces, whose reflection and/or scattering behavior is not well modeled by geometrical-acoustics techniques. When wave-based simulations

or analyses are not feasible, explicit diffraction calculations can be used alone or combined with GA results to provide increased accuracy. Applications can be found in many areas of acoustics including noise-barrier performance [71, 143, 169, 172], room acoustics [60, 201, 263, 265], radiation from loudspeakers [213, 259, 280], exploration seismology [16, 103, 267], and scattering from the ocean surface and bottom [58, 80, 126].

In this thesis we are interested mainly in the application of diffraction modeling to simulations of room acoustics, specifically environments with occluders and geometric elements whose dimensions can be comparable to or smaller than the wavelengths of interest. In such cases, diffraction calculations can correct for the high-frequency approximation inherent in GA modeling techniques to allow for: deviations from pure specular reflections; sound propagation into shadow zones; and smooth, continuous sound fields at reflection and shadow boundaries. All of these factors are important not only for physical accuracy, but also to achieve perceptual realism when auralizing sound fields for virtual-acoustic simulations.

The general edge-diffraction problem deals with the geometry of a wedge, and considers diffraction from the intersection of the two planar wedge faces. The classical problem of diffraction from an infinite wedge of arbitrary angle illuminated or insonified by spherical waves has various solutions dating back to 1915.[2] These solutions may be exact or approximate/asymptotically correct, and are given in either the time-domain or the frequency domain. Most derivations are made with the assumption of ideal surface properties for the faces of the wedge, *e.g.* perfectly conducting surfaces in the electromagnetic case, or perfectly hard (rigid) or soft surfaces (Neumann or Dirichlet boundary conditions, respectively) for the acoustic case. The following sections describe some of these methods and provide further examples of their application.

2.2.1 Exact Methods

Macdonald [166], Oberhettinger [195], Bowman and Senior [28], and Pierce [208] all present frequency-domain, contour-integral expressions for diffraction from an infinite rigid wedge insonified by a time-harmonic point source. (Pierce's expression,

[2] Earlier diffraction expressions exist, but for more restricted cases such as that for the diffraction of plane waves from a hard, thin screen (half plane) given by Sommerfeld in 1896 [242].

in somewhat modified form, is given in Equation 3.15 in Section 3.6.3.) While exact, their formulations do not lend themselves to simple evaluation and as such are used mainly as reference solutions for comparison with other methods (which we do in Section 3.6.3), or are employed in simplified (non-exact) form, *e.g.* see [207, 280].

As mentioned above in the context of modeling techniques, time-domain calculations are sometimes preferred over frequency-domain methods, for example when an impulse response is desired for processing or when broadband results require impractical, multiple iterations of a monochromatic frequency-domain solution. For such cases, the Biot-Tolstoy-Medwin method [18, 169] provides the exact diffraction impulse response from an infinite wedge insonified by a point source, and its reformulation by Svensson *et al.* [258] gives the exact solution for first-order diffraction from a finite edge as a line integral along that edge. The latter of these is employed throughout the remainder of this thesis, and Chapter 3 provides a detailed description of the method, including its derivation, applications, and validation.

2.2.2 Approximate and Asymptotic Methods

As described above in the context of the BEM, the Helmholtz-Kirchhoff integral gives the pressure at a point as an integral over the surrounding surfaces. Through a simplification known as the Kirchhoff approximation (KA), in which the pressure and particle velocity on each surface element are approximated with the values that would exist if the surface was infinite in extent, the HK integral can be solved to yield the diffracted components of a sound field. The Maggi-Rubinowicz transformation of the simplified HK integral gives the diffraction as a "boundary wave" emanating from a diffracting edge, *i.e.* an integral along the edge [26]. Trorey [266, 267], Embleton [71], and Sakurai and Nagata [224] provide such diffraction expressions, and apply them to seismic imaging, noise-barrier analysis, and room acoustics, respectively. Formulations similar to Trorey's also are given by Hilterman [102, 103] and Berryhill [16] and applied to problems in geophysics. Limitations of diffraction calculations based on the KA have also been studied, in particular by Jebsen and Medwin [110] and Norton *et al.* [190] who describe significant errors

in backscattered diffraction through comparison with more accuracte numerical simulation techniques.[3]

Another approximate method for simulating diffraction is the Geometrical Theory of Diffraction (GTD) [130] and the related Uniform Theory of Diffraction (UTD) [137]. Developed in the context of geometrical optics from high-frequency, asymptotic expansions of exact expressions for the diffraction of a plane wave by a half-plane and a wedge, the GTD provides a means to find diffracted rays emanating from the edge of a wedge, a concept amenable to integration with geometrical acoustics as well. The main shortcoming of the GTD is its failure near reflection and shadow boundaries, a problem overcome by the UTD through the use of so-called transition functions that, when combined with the original GTD diffraction coefficients, provide for a continuous and bounded diffracted field. Applications of UTD calculations in virtual-acoustic simulations are described below. Pierce [207] describes a related uniform asymptotic expression for edge diffraction based on a high-frequency approximation of his exact solution for diffraction of spherical waves by a rigid wedge [208]. A comparison of Pierce's method with the GTD and the UTD is given in [122].

Numerous other approximate diffraction expressions exist, although they have been given less attention in the literature. For example, Vanderkooy [280] provides a time-domain line-integral wedge-diffraction expression based on the high-frequency asymptotic solution from Bowman and Senior [28], and applies it to diffraction from loudspeaker cabinets. Menounou *et al.* [171] describe the "directive line-source model" for noise-barrier analysis, an approximate solution based on the integration of infinitesimal secondary sources distributed along a diffracting edge. Stephenson and Svensson [248] describe a diffraction model suitable for use with ray-tracing simulations, in which the Heisenberg Uncertainty Principle is used to bend rays around edges (an idea also used in optical simulations [82]).

2.2.3 Diffraction Modeling in Room Acoustics

The inclusion of edge diffraction in room-acoustics simulation and analysis has been addressed by a number of authors, and the calculations typically are based on either

[3]Thorsos [261] also describes the conditions for validity of the Kirchhoff approximation, but in the context of rough-surface scattering rather than diffraction.

the Kirchhoff approximation, the UTD, or the Biot-Tolstoy-Medwin method. For the first of these, Sakurai and Nagata [224] used their expression to study the early, first-order reflections from the stage walls and ceiling in an auditorium, and Sakurai and Ishida [223] extended their results to multiple reflections. More recently, Tsingos and Gascuel [276] used a KA-based method to approximate the diffraction around occluders in virtual environments. Tsingos *et al.* [269, 270] describe the use of programmable graphics hardware to accelerate scattering calculations, which include diffraction, based on efficient evaluation of the HK integral simplified with the Kirchhoff approximation.

As mentioned above, the diffracted-ray interpretation of the UTD makes it an attractive method to combine with geometrical-acoustics modeling techniques. The existence of a "diffraction cone" resulting from the equal angles of incidence and diffraction posited by Keller [130] makes UTD calculations particularly well suited for integration with beam tracing, and Tsingos *et al.* [271] and Funkhouser *et al.* [85] developed such a beam-tracing system capable of including diffracted paths whose contributions were calculated with the UTD. The beam-tracing system of Antonacci *et al.* [7] also employs UTD diffraction, as does the frustum-tracing system of Chandak *et al.* [37].

Diffraction calculations based on the Biot-Tolstoy-Medwin method [18, 169] also have been used extensively in room acoustics modeling. As described above, such a time-domain method is particularly appropriate for room acoustics due to the common use and analysis of impulse responses rather than frequency-domain transfer functions. In addition, the applicability of the line-integral formulation in [258] to finite edges provides an increase in accuracy over high-frequency, infinite-edge approximate methods such as the UTD when modeling diffraction from objects whose dimensions are comparable to the wavelengths associated with the audible spectrum. Ouis [201] studied the effect of diffraction from the edge of a thin barrier, meant to represent the presence of a side balcony, on the acoustics of a rectangular space using scale-model measurements and image-source/BTM simulations. Torres *et al.* [265] presented similar measurements and simulations for a scale model of a stage house, and of particular significance to Chapter 6, they used listening tests to study the audibility of the diffraction contributions in their simulations. Løvstad and Svensson [164] also presented measured and simulated impulse responses for a model of an orchestra pit. BTM-based diffraction also has been integrated into the

Digital Interactive Virtual Acoustics (DIVA) simulation and auralization system of Savioja, Lokki, *et al.* [162, 211, 230]. For auralization of diffraction in this system, an approximation can be used in which BTM diffraction IRs are converted into transfer functions (with an FFT) which are smoothed and fit with warped infinite-impulse response filters for efficient rendering [162]. In a similar fashion, de Rycker [60] and Torres *et al.* [264] approximated diffraction IRs with finite impulse-response low-pass filters and applied them to simulated sound fields in a virtual performance space.

Commercially available acoustic modeling tools such as CATT [52] and Odeon [38] simulate the *effects* of diffraction on the reflection and scattering from finite surfaces by adjusting the spectra of specular reflections and the fraction of energy that is scattered in non-specular directions. However, they do not calculate diffraction explicitly, and thus do not model sound propagation into shadow zones or address the discontinuities at reflection and shadow boundaries. Tsingos and Gascuel [275] describe a method to approximate the diffracted sound field behind occluders in virtual environments without direct diffraction computations by using graphics hardware to evaluate partial obstructions of Fresnel volumes.

Chapter 3

The Biot-Tolstoy-Medwin Diffraction Formulation

3.1 Introduction

In this thesis, we utilize the line-integral formulation of the Biot-Tolstoy-Medwin diffraction expression [18, 169] developed by Svensson *et al.* [258] for all diffraction modeling. The remainder of this chapter covers: the development of this formulation for continuous-time diffraction impulse responses (IRs) (Sections 3.2 - 3.4); the conversion from continuous-time to discrete-time IRs (Section 3.5, also addressed in Chapter 5); a frequency-domain formulation and its relationship to other diffraction expressions (Section 3.6); a summary of validation experiments, comparing BTM simulations to other numerical methods and to physical measurements (Section 3.7); and finally a discussion of the method's limitations (Section 3.8). While both Medwin and Svensson *et al.* have provided extensions of the BTM model for higher-order diffraction (the limitations of which are described in Section Section 3.8), the following discussion is restricted to first-order diffraction. Section 3.6 has been accepted for publication in slightly modified form [257].

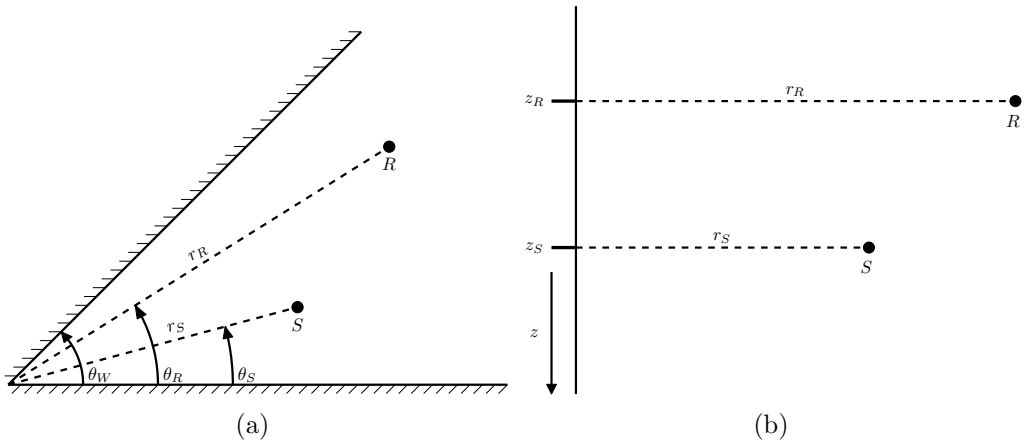

Figure 3.1: 2D projections of the infinite 3D wedge geometry and cylindrical coordinate system. The z-axis is aligned with the edge (perpendicular to the page in (a)), r is measured radially from the edge, and θ is the angle of rotation about the edge measured from one of the faces. The source is located at (r_S, θ_S, z_S) and the receiver at (r_R, θ_R, z_R).

3.2 The Original Biot-Tolstoy Diffraction Expression

In [18], Biot and Tolstoy (BT) provide a solution of the wave equation in cylindrical coordinates (r, θ, z) within an infinite wedge geometry for the displacement potential Φ, from which the acoustic pressure can be found through the relation

$$p = -\rho \frac{\partial^2 \Phi}{\partial t^2}, \tag{3.1}$$

where ρ is the density of the medium within the open portion of the wedge. As shown in Figure 3.1, the coordinate system is oriented such that the z-axis is aligned with the edge of the wedge, r is the radial distance from the edge, and θ measures rotation about the edge with one wedge face at $\theta = 0$ and the other at $\theta = \theta_W$. The BT solution, which is derived using the method of normal coordinates, is a superposition of modes in the wedge-shaped space: rigid boundary conditions are applied at the faces and the modal amplitudes and phases are matched to an "instantaneous unit-volume injection point source" arbitrarily placed within the wedge. The summation of normal modes (a discrete sum over θ due to the boundary conditions and continuous integrals over r and z) collapses into an explicit time-domain expression for the direct sound, specular reflections from the faces, and

diffraction from the edge or wedge apex, *i.e.* the infinite, linear intersection of the two wedge faces. The terms for the direct sound and specular reflections are the expected Dirac delta functions with appropriate delays, and as such are typically considered separately as the geometrical-acoustics components that can be found using alternate techniques such as the image-source method [2]. It is only the term for the diffracted component that is of interest here; combining diffraction with GA modeling is discussed further in Chapter 7.

Using a combination of notation from [18] and [258], the continuous-time BT expression for diffraction from an infinite rigid wedge insonified by a point source at (r_S, θ_S, z_S) and measured at a receiver at (r_R, θ_R, z_R) is

$$\frac{\partial \Phi}{\partial t} = \frac{c}{4\pi\theta_W} \cdot \frac{e^{-\nu\eta}}{r_S r_R \sinh\eta} \cdot \frac{\sin[\nu(\pi \pm \theta_S \pm \theta_R)]}{1 - 2e^{-\nu\eta}\cos[\nu(\pi \pm \theta_S \pm \theta_R)] + e^{-2\nu\eta}}, \tag{3.2}$$

where c is the speed of sound, $\nu = \pi/\theta_W$ is the wedge index, and θ_W is the open wedge angle. The auxiliary function η is

$$\eta = \cosh^{-1}\frac{c^2t^2 - (r_R^2 + r_S^2 + z_R^2)}{2r_S r_R}, \tag{3.3}$$

with the assumption that the $z-$axis is aligned such that $z_S = 0$. The $\pm$ notation is shorthand for a sum over the four angles

$$\begin{aligned} \varphi_1 &= \pi + \theta_S + \theta_R, & \varphi_2 &= \pi + \theta_S - \theta_R, \\ \varphi_3 &= \pi - \theta_S + \theta_R, & \varphi_4 &= \pi - \theta_S - \theta_R, \end{aligned} \tag{3.4}$$

and thus Eq. (3.2) also can be written

$$\frac{\partial \Phi}{\partial t} = \frac{c}{4\pi\theta_W} \cdot \frac{e^{-\nu\eta}}{r_S r_R \sinh\eta} \cdot \sum_{i=1}^{4} \frac{\sin(\nu\varphi_i)}{1 - 2e^{-\nu\eta}\cos(\nu\varphi_i) + e^{-2\nu\eta}}. \tag{3.5}$$

Using Eq. (3.1), the corresponding diffracted acoustic pressure is

$$\begin{aligned} p(t) &= \frac{\rho c^3}{4\pi\theta_W} \cdot \frac{t}{r_S^2 r_R^2 \sinh^2\eta} \cdot e^{-\nu\eta} \cdot \\ &\quad \sum_{i=1}^{4} \left[\coth\eta \cdot \frac{\sin(\nu\varphi_i)}{1 - 2e^{-\nu\eta}\cos(\nu\varphi_i) + e^{-2\nu\eta}} + \right. \\ &\quad \left. \frac{\pi}{\theta_W} \frac{(1 - e^{-2\nu\eta})\sin(\nu\varphi_i)}{\left[1 - 2e^{-\nu\eta}\cos(\nu\varphi_i) + e^{-2\nu\eta}\right]^2} \right] \cdot H\left(t - \frac{L_0}{c}\right), \end{aligned} \tag{3.6}$$

where H is the Heaviside step function and L_0 is the length of the shortest path from the source to the receiver via the edge. In this form, the BT solution is exact for the diffraction from an infinite *rigid* wedge. Pressure-release wedges also can be modeled with a change of sign for the first and fourth terms in the summation [132, 258]. "Combination" wedges with one rigid face and one pressure-release face can be handled with a suitable modification of the signs of the summation terms that satisfies the desired boundary conditions.

3.3 Medwin's Modifications

One non-ideal aspect of the original BT solution is the source type, an "instantaneous unit-volume injection point source ... [which] leads to a spherically propagating pressure doublet (*i.e.*, an infinite compression followed instantaneously by an infinite rarefaction)." [18] This yields a source-pressure function that is proportional to the time derivative of a Dirac delta function, but a more useful source would yield a pressure function proportional to the Dirac function itself. To this end, Medwin chose "to assume a point source S (volume/time) which starts to flow uniformly and instantaneously at $t = 0$, ... [and thus] radiates a delta function of pressure." [169] With such a source, the diffracted pressure is then given by the so-called Biot-Tolstoy-Medwin (BTM) solution,

$$p(t) = \frac{-S\rho c}{8\pi\theta_W} \cdot \frac{1}{r_S r_R \sinh\eta} \cdot \sum_{i=1}^{4} \beta_i \tag{3.7}$$

where the functions β_i are

$$\beta_i = \frac{2e^{-\nu\eta}\sin(\nu\varphi_i)}{1 - 2e^{-\nu\eta}\cos(\nu\varphi_i) + e^{-2\nu\eta}} = \frac{\sin(\nu\varphi_i)}{\cosh(\nu\eta) - \cos(\nu\varphi_i)}. \tag{3.8}$$

The use of the β_i notation was introduced later by Svensson *et al.* in [258], specifically with the latter form in Eq. (3.8), and the significance of these functions is discussed further below.

Medwin also addressed the application of Eq. (3.7) to noise barriers with edges of finite length by truncating the infinite-edge response at the time associated with the longest path from the source to the receiver through the finite edge. In this context, he pointed out that for the infinite edge, there exist two points that contribute to each instant of the diffraction impulse response, one on each side of the so-called apex point, the point on the edge that represents the least time $S \rightarrow \text{Edge} \rightarrow R$ path. For the finite-edge case, it is possible for both, one, or neither of these points to contribute to the diffraction IR at a given instant of time, resulting in the diffracted pressure being, respectively, equal to that for the infinite-edge case, half of that for the infinite-edge case[1], or zero. While the first and last of these are obvious results and can be stated without proof, Svensson *et al.* definitively established that the two "sides" of the edge do in fact contribute equally to the diffracted pressure [258]. Examples of this two-sided contribution can be seen in Figure 3.3 in the context of computing discrete-time diffraction IRs.

3.4 Secondary Source Functions and the Line-Integral Formulation

In [258], Svensson *et al.* further developed the BTM expression into a more physically intuitive solution. In particular, they reformulated the expression as a line integral along the diffracting edge, which has the benefit of allowing for simulations of finite and infinite edges with the appropriate choice of integration limits. This new formulation suggests the interpretation of the edge as a collection of infinitesimal secondary sources of radiation (a concept also used by Medwin *et al.* in their "discrete Huygens" interpretation of second-order diffraction in [170]), and thus

[1] In a later paper, Medwin *et al.* [170] suggest that the contributions from the two sides of the least-time point are not equal, but instead should be scaled by a factor related to the asymmetry of the geometry.

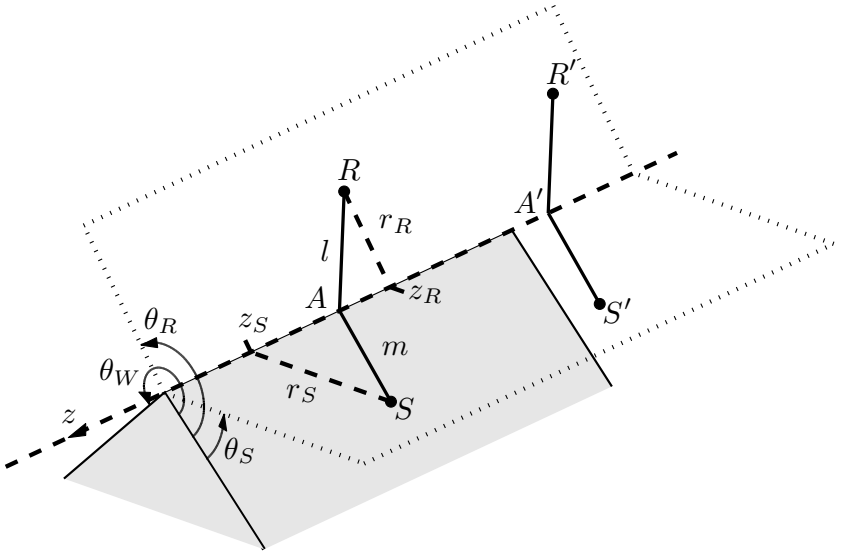

Figure 3.2: Wedge geometry and edge-aligned cylindrical-coordinate system for a finite wedge. For the source/receiver pair (S, R) the apex point A is included in the physical edge; this is always the case for infinite edges. For the source/receiver pair (S', R') the apex point A' is not included in the physical edge, and this condition can only occur for finite wedges.

the integrand as the product of secondary-source directivity functions (β_i) and distance-attenuation terms. Isolating the diffraction impulse response from the source function, the former is given by

$$h_{diffr}(t) = -\frac{\nu}{4\pi} \sum_{i=1}^{4} \int_{z_1}^{z_2} \delta\left(t - \frac{m+l}{c}\right) \frac{\beta_i}{ml}\, dz, \tag{3.9}$$

where the β_i functions are given in Eq. (3.8) and m and l are the distances from the source to a point on the edge and the receiver to a point on the edge, respectively, as seen in Figure 3.2. The integration limits z_1 and z_2 correspond to the $z-$ coordinates for the end points of a finite edge, and can take the values $\pm\infty$ for an infinite wedge. For numerical convenience, the auxiliary function η can be rewritten as [258]

$$\eta = \cosh^{-1}\left\{\frac{ml + (z - z_S)(z - z_R)}{r_S r_R}\right\}. \tag{3.10}$$

To obtain the diffracted pressure, the source signal is defined as $q(t) = \rho A(t)/4\pi$, where ρ is again the density of the propagation medium and $A(t)$ is the volume acceleration of the point source. Such a source signal implies that the free-field

impulse response of the source is $h(t) = \delta(t - d/c)/d$, where d is the distance from the source to the receiver. The diffracted sound pressure can be calculated using Eq. (3.9) through the convolution integral

$$p(t) = \int_0^\infty h_{diffr}(\tau) q(t - \tau) d\tau. \tag{3.11}$$

In summary, the metamorphosis of the BTM solution from Eq. (3.2) to Eq. (3.7) to Eq. (3.9) resulted in a number of computational improvements. First, the implicit source function was changed from a doublet to a Dirac delta function, making evaluation of the diffraction impulse response straightforward. Second, the singularity due to the sinh() function in the denominator was removed, allowing for simpler numerical evaluation. (The singularity due to the denominator of the β_i functions taking the value 0 still remains, however, and is addressed in more detail in Sections 4.3 and Chapter 4.) Finally, the conversion to an integral over the length of the edge allows for the explicit calculation of diffraction from finite edges. This is particularly valuable in the case of virtual-acoustic simulations in architectural environments: the acoustic wavelength can be comparable to or greater than the lengths of the edges in the environment, violating the infinite-edge assumption of high-frequency asymptotic methods such as the Uniform Theory of Diffraction [137].

3.5 From Continuous Time to Discrete Time

In most computational applications, a discrete-time representation of the diffraction impulse response is needed, and the standard technique is to area-sample a continuous-time expression such as Eq. (3.7) [170, 43, 258]. Given a sampling frequency F_S, such an area-sampling corresponds to the integration of the analytic expression over a time range that is $\pm 0.5/F_S$ around each sample instant, *i.e.*,

$$h_{diffr}(n) = \int_{(n-0.5)/F_S}^{(n+0.5)/F_S} h_{diffr}(\tau)\ d\tau, \tag{3.12}$$

where $h_{diffr}(n)$ is the discrete-time IR with sample index n. The transition from the continuous-time *line-integral* expression in Eq. (3.9) to a discrete-time formulation using the area-sampling in Eq. (3.12) is accomplished by setting the integration

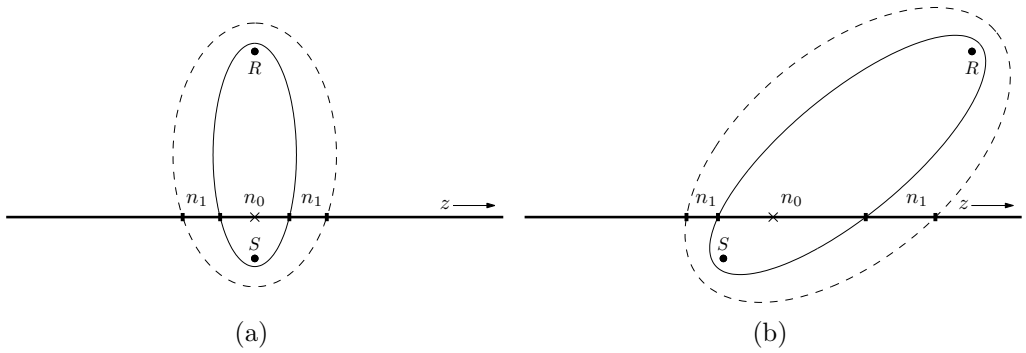

Figure 3.3: Unfolded 2D view of sample-aligned segments for the first two samples of an edge-diffraction IR for two source/receiver geometries. For each, the apex point is marked with an '×'. In both cases, the segment of the edge within the solid ellipse contributes to the first sample (n_0) of the edge-diffraction IR, and the two segments between the solid and dashed ellipses to the second sample (n_1). For (b), an asymmetric case, the two segments marked n_1 are of different lengths, but contribute equally to the second sample of the IR.

limits $z_{n,1}$ and $z_{n,2}$ for the nth sample to points along the edge that correspond to the travel times $(n-0.5)/F_S$ and $(n+0.5)/F_S$. With such boundaries, each segment contributes to exactly one sample of the discrete-time diffraction IR, which can be written

$$h(n) = -\frac{\nu}{4\pi} \sum_{i=1}^{4} \int_{z_{n,1}}^{z_{n,2}} \frac{\beta_i}{ml} dz. \tag{3.13}$$

Such "sample-aligned" segments correspond to portions of an edge that lie between intersections of two confocal ellipsoids with the edge: the foci are the source and receiver locations, and the lengths of the axes are determined by the distances $c(n \pm 0.5)/F_S$. Examples are shown in Figure 3.3. A detailed description of the steps to compute the sample-aligned segment boundaries can be found in Appendix A2 of [255]. Further discussion of sample-aligned edge segments, as well as other edge subdivision methods, can be found in Chapter 5.

3.6 A Frequency-Domain Formulation

While the time-domain BTM formulation in Eq. (3.9) can be useful for identifying individual diffraction components in a simulated IR, certain applications, such as the study of the insertion loss provided by noise barriers, traditionally have employed

analysis in the frequency domain. In addition, the low-pass filtering effect of area-sampling Eq. (3.9) to obtain the discrete-time expression in Eq. (3.13) can be avoided with computations done directly in the frequency domain. While frequency-domain representations of the original Biot-Tolstoy expression and Medwin's BTM expression have been developed previously, none has had the main advantage of the line-integral formulation: direct application to finite edges. In this section, it is shown that the time-domain line-integral BTM expression can be transformed to provide the exact first-order edge-diffraction solution for a finite or infinite wedge in the frequency domain [257]. Furthermore, for an infinite wedge this new formulation is shown to be equivalent to a reference contour-integral solution from [28] and [208] via a transformation of variables.

3.6.1 Previous Frequency-Domain BTM Expressions

In [169], Medwin suggests a "compromise technique" to transform his diffraction expression into the frequency domain due to the lack of an analytical transform. Noting that the diffracted energy is highest at and shortly after the onset of the diffraction IR, he provides an approximation of the time-domain expression for small time values (relative to the onset time) that is analytically transformable. This is complemented with a discrete Fourier transform of the remainder of the diffraction IR to form a complete, but approximate, frequency-domain representation. In a somewhat similar fashion, Kinney *et al.* [132] exploit the dominance of the diffraction onset by developing an analytically transformable approximation to the BTM solution that is asymptotically correct for small time values. In [203], Ouis describes *eight* approximations of Medwin's BTM formulation (one is Medwin's original approximation, the remaining seven are original) that can be transformed into frequency-domain expressions, specifically for diffraction from a hard half-plane.

3.6.2 The Line-Integral Frequency-Domain Formulation

The new line-integral frequency-domain formulation results from a direct Fourier transformation of the time-domain expression given in Eq. (3.9). Since the time variable t occurs only in the δ-function, the transformation is straightforward, and

yields the edge-diffraction transfer function, $H_{diffr}(\omega)$, as a line integral:

$$H_{diffr}(\omega) = -\frac{\nu}{4\pi} \sum_{i=1}^{4} \int_{z_1}^{z_2} e^{-jk(m+l)} \frac{\beta_i}{ml} \, dz. \tag{3.14}$$

A time function of $e^{j\omega t}$ is assumed but omitted.

As with the time-domain formulation, the singularity due to the denominator of the β_i functions taking the value 0 for a receiver on a reflection or shadow boundary must be considered when evaluating Eq. (3.14). If the apex point is not included in the physical wedge, *i.e.* z_a is not in the interval $[z_1, z_2]$, the singularity does not affect the integral and thus ordinary numerical-integration techniques can be used to compute $H_{diffr}(\omega)$. To avoid the singularity when necessary, it is possible to use an analytical approximation of the integrand in the vicinity of the apex point. Such an approximation for the time-domain expression is described in Section 4.3.1 and its validity for use with Eq. (3.14) is addressed in Section 4.3.6. This analytical expression simplifies the numerical integration and offers a formulation that is robust to zone-boundary crossings.

3.6.3 Relationship to the Contour-Integral Solution for the Infinite Wedge

As mentioned above, a related, exact, frequency-domain diffraction expression for the infinite wedge was given independently by Bowman and Senior in [28] and by Pierce in [208]. That formulation is shown below, with some changes of variable names made for easier comparison to the new frequency-domain BTM line-integral formulation. In particular, the original contour-integral integration variable, t in [28] and s in [208], corresponds to η defined in Eq. (3.10). The integration range (typically $-\infty$ to ∞) can be halved because the integrand is even in η, and the reference solution is then

$$H_{diffr}^{ref}(\omega) = -2 \, \frac{\nu}{4\pi} \sum_{i=1}^{4} \int_{0}^{\infty} \frac{e^{-jkR_{ref}}}{R_{ref}} \beta_i \, d\eta, \tag{3.15}$$

where β_i are the same as in Eq. (3.8), and

$$R_{ref} = \sqrt{r_S^2 + r_R^2 + (z_R - z_S)^2 + 2\ r_S\ r_R\ \cosh\eta}. \tag{3.16}$$

Comparing Eqs. (3.14) and (3.15), equivalence of the two formulations can be established if

$$R_{ref} = m + l, \tag{3.17}$$

and

$$\frac{d\eta}{R_{ref}} = \frac{dz}{ml} \Rightarrow \frac{d\eta}{dz} = \frac{R_{ref}}{ml}. \tag{3.18}$$

To address Eq. (3.17), setting $z_S = 0$, without loss of generality, simplifies the derivation somewhat. The expressions for m and l needed to continue are

$$m = \sqrt{r_S^2 + z^2}, \quad l = \sqrt{r_R^2 + (z - z_R)^2}. \tag{3.19}$$

Squaring both sides of Eq. (3.17) leads to the variable

$$f_1 = R_{ref}^2 - (m + l)^2, \tag{3.20}$$

and the goal is then to show that $f_1 = 0$ (since R_{ref}, m, and l all are positive). Substituting Eqs. (3.16) and (3.19) into Eq. (3.20) yields

$$\begin{aligned} f_1 &= r_S^2 + r_R^2 + z_R^2 + 2r_S r_R \cosh\ \eta - \left[\sqrt{r_S^2 + z^2} + \sqrt{r_R^2 + (z - z_R)^2}\right]^2 \\ &= 2r_S r_R \cosh\ \eta - 2z(z - z_R) - 2\sqrt{r_S^2 + z^2}\sqrt{r_R^2 + (z - z_R)^2}. \end{aligned} \tag{3.21}$$

Applying the definition of η (Eq. 3.10) to Eq. (3.21) results in $f_1 = 0$.

To address the second part of the proof, Eq. (3.18) can be rewritten using Eq. (3.17) as

$$\frac{m + l}{ml} = \frac{d\eta}{dz}. \tag{3.22}$$

To establish equality, $d\eta/dz$ can be derived using the definition of η which yields

$$\begin{aligned}
\frac{d\eta}{dz} &= \frac{r_S r_R}{\sqrt{\left[ml + z(z - z_R)\right]^2 - r_S^2 r_R^2}} \\
&= \frac{\frac{zl}{m} + \frac{(z-z_R)m}{l} + 2z - z_R}{\sqrt{\left[ml + z(z - z_R)\right]^2 - r_S^2 r_R^2}} \\
&= \frac{\frac{1}{ml}\left[zl^2 + (z - z_R)m^2 + (2z - z_R)ml\right]}{\sqrt{\left[ml + z(z - z_R)\right]^2 - r_S^2 r_R^2}} \\
&= \frac{\frac{2}{ml}\left[z(m + l)^2 - z_R m(m + l)\right]}{\sqrt{\left[ml + z(z - z_R)\right]^2 - r_S^2 r_R^2}} \\
&= \frac{\frac{m+l}{ml}\left[z(m + l) - z_R m\right]}{\sqrt{\left[ml + z(z - z_R)\right]^2 - r_S^2 r_R^2}}.
\end{aligned} \tag{3.23}$$

Inserting this expression into Eq. (3.22), rearranging, and squaring both sides yields the variable f_2 that will be shown to vanish (the involved terms are all positive so the squaring introduces no sign ambiguity):

$$\begin{aligned}
f_2 &= \left\{\left[ml + z(z - z_R)\right]^2 - r_S^2 r_R^2\right\} - \left[z(m + l) - z_R m\right]^2 \\
&= m^2 l^2 + z^2(z - z_R)^2 + 2mlz(z - z_R) - r_S^2 r_R^2 \\
&\quad - \left\{z^2(m + l)^2 + z_R^2 m^2 - 2zz_R m(m + l)\right\} \\
&= m^2\left[l^2 - (z - z_R)^2\right] + z^2\left[(z - z_R)^2 - l^2\right] - r_S^2 r_R^2 \\
&= \left[l^2 - (z - z_R)^2\right](m^2 - z^2) - r_S^2 r_R^2 \\
&= 0.
\end{aligned} \tag{3.24}$$

Pierce [208] presents a similar argument by applying a different transformation of variables followed by an inverse Fourier transform to his frequency-domain formulation to arrive at the original (time-domain) Biot-Tolstoy expression [18]. Chu *et al.* [41] also provide a proof of equivalence between the original BT solution and Pierce's contour-integral solution by applying the Fourier transform to the former with a change of integration variable from t to η, followed by a short series of trigonometric and algebraic manipulations.

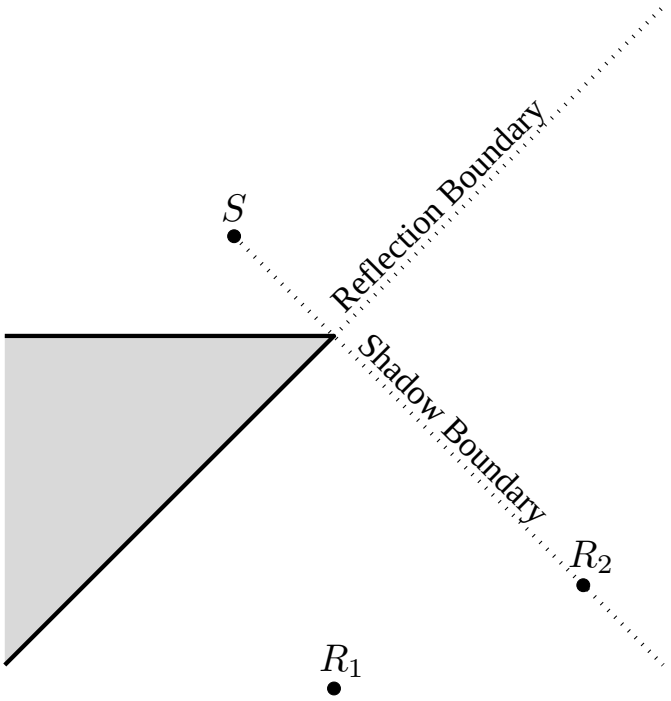

Figure 3.4: 2D view of the geometry used to produce the results in Figures 3.5 - 3.7. For the source: $r_S = 2$ m, $\theta_S = 45°$, $z_S = 0$ m. For receiver R_1: $r_R = 5$ m, $\theta_R = 270°$, $z_R = 0$ m. For receiver R_2: $r_R = 5$ m, $\theta_R = 224.999°$, $z_R = 0$ m. The wedge angle $\theta_W = 315°$. The length of the edge (perpendicular to the page) varies and is given for each set of results.

3.6.4 Sample Calculations

One basic geometry has been chosen for numerical evaluation of the new frequency-domain formulation. Fig. 3.4 depicts the wedge (in 2D), with one source position, S, and two receiver positions, R_1 and R_2. Furthermore, different edge lengths (perpendicular to the page) are used in the various examples, as specified below.

Equations (3.14) and (3.15) were used to compare the new formulation to the reference solution, respectively. [2] Of particular interest was the edge length needed in the former to provide a suitable approximation of the infinite edge in the latter. As can be seen in Figure 3.5, increasing the edge length to 200 m with the new formulation yields results for which the error is approximately 100 dB below the reference solution at low frequencies and decreases with increasing frequency.

[2]Numerical integration was computed using the *quadgk* function in Matlab®, which implements adaptive Gauss-Kronrod quadrature. A relative tolerance of 10^{-6} has been used for all calculations.

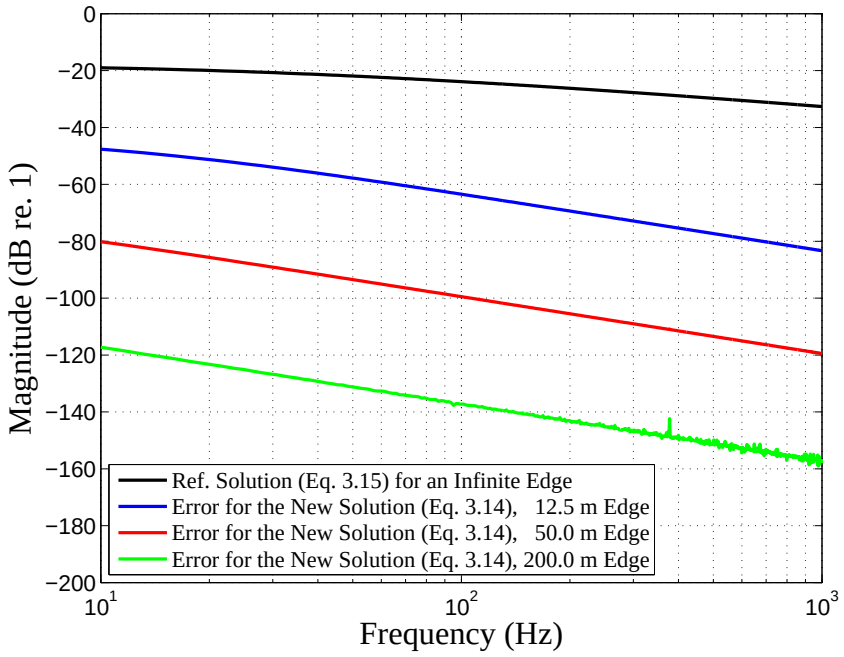

Figure 3.5: $|H_{diffr}(\omega)|$ calculated with the reference solution, Eq. (3.15), for an infinite edge using the geometry in Fig. 3.4 and receiver R_1. Error for the new formulation, Eq. (3.14), is shown for edges with various lengths, indicating the convergence to the reference solution with increasing length.

The new formulation has also been compared to a discrete Fourier transform of the diffraction impulse response in Eq. (3.13). The edge length was set to 1 m ($z_1 = 0$ and $z_2 = 1$). As described previously, the use of area sampling to convert the continuous-time expression to a discrete-time IR corresponds to a first-order low-pass filter, and such a low filter order can result in significant aliasing effects. Therefore, in order to reach a high level of accuracy for the transformed time-domain results, a high sampling frequency must be chosen. In Fig. 3.6, the new method has been used to compute a reference magnitude spectrum, and the spectral error associated with Fourier-transformed time-domain calculations using sampling frequencies of 48, 96, 192, and 384 kHz are shown (48 kHz in Fig. 3.6(a) only). As can be seen in Figure 3.6(a), the error for receiver R_1 decreases as expected when the sampling frequency is increased, indicating its dominant source is the aliasing mentioned above. For each sampling frequency, the error increases approximately 6 dB per octave due to the first-order nature of low-pass filtering due to area sampling. The ripple seen in the frequency-domain solution is caused by the finite length of the edge. In Figure 3.6(b), results are shown for receiver R_2 which is very close to the shadow boundary. The reference magnitude spectrum is nearly flat, corresponding

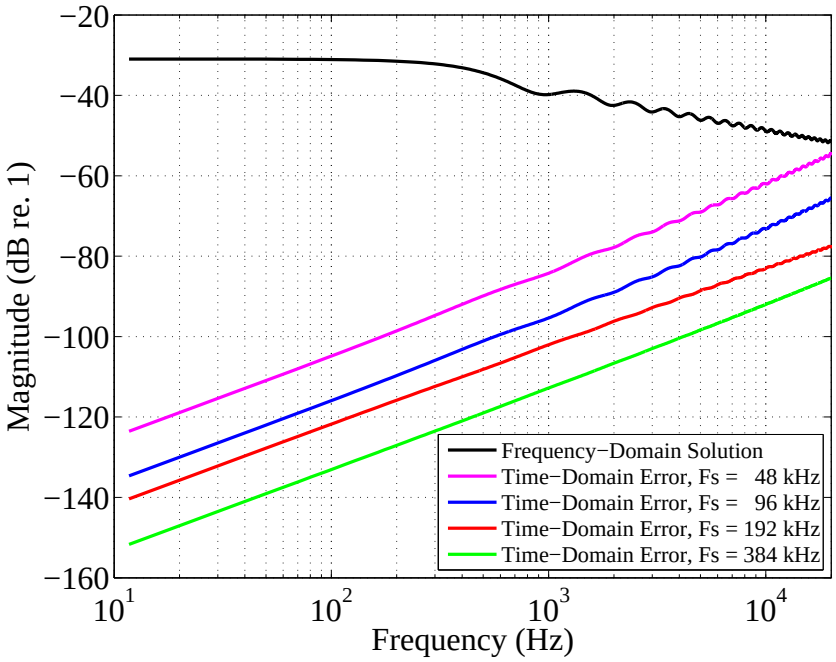

(a) Receiver R_1

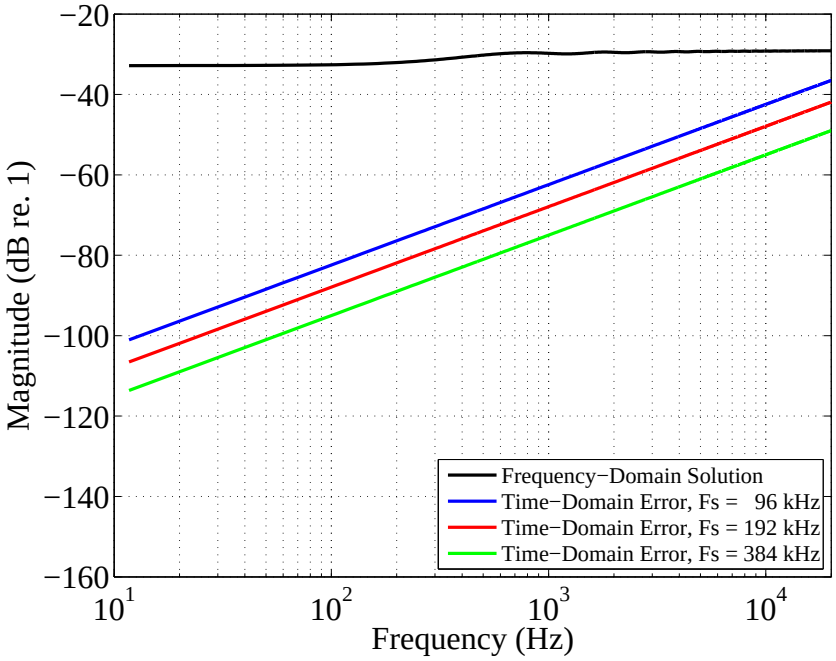

(b) Receiver R_2

Figure 3.6: $|H_{diffr}(\omega)|$ calculated with the new frequency-domain BTM formulation (Eq. (3.14)) for the geometry in Fig. 3.4, using edge endpoints $z_1 = 0$ m, $z_2 = 1$ m. Time-domain solutions computed for sampling frequencies 48 ((a) only), 96, 192, and 384 kHz have been transformed to the frequency domain using the FFT, and the error relative to the frequency-domain solution is shown. (a) Data for receiver R_1. (b) Data for receiver R_2.

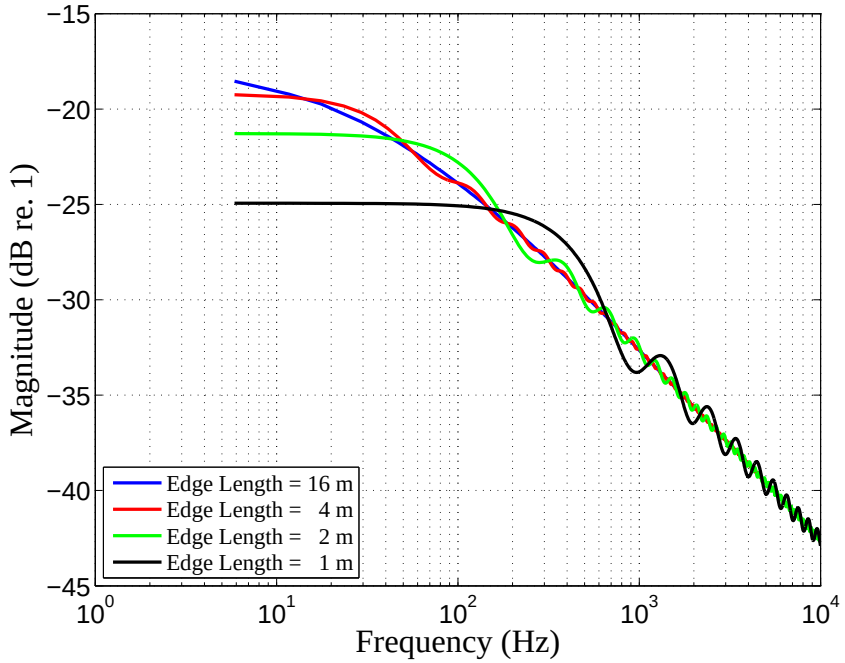

Figure 3.7: $|H_{diffr}(\omega)|$ calculated for the geometry in Fig. 3.4, using receiver R_1 and edge lengths of 1, 2, 4, and 16 m.

to the Dirac-like behavior of the diffraction IR for such receiver positions. The error is significantly higher in this case, also due to the pulse-like characteristics of the impulse response near the zone boundaries.

The effect of varying the edge length was also studied, and the results shown in Figure 3.7 agree with those presented by de Rycker [60] and Torres *et al.* [264]. The low-frequency magnitude decreases as expected with decreasing edge length, and the spectral ripple, which is due to the sudden truncation of the edge (and it's associated impulse response), increases as expected with decreasing edge length.

3.7 Numerical and Experimental Validation

3.7.1 Comparison to Measurements

Medwin's BTM formulation has been the subject of many validation experiments, with measured data for various geometries typically captured by recording the scattered (reflected and diffracted) field due to insonification by a spark source.

Such sources tend to produce little low frequency energy[3], and thus the requirement of rigid wedge faces for the BTM solution is easily met with common materials such as plasterboard, plywood, and aluminum used in these experiments. The free-field spark response can be convolved with the simulated impulse response to allow for direct comparison of measured and simulated data.

In his original paper on the subject [169], Medwin compared BTM predictions to measured insertion-loss data between 1 and 40 kHz from Jonasson [115] and Bremhorst [30] for a wedge with $\theta_W = 270°$ and a screen with $\theta_W = 360°$. The reported error is near 1 dB across the measured spectrum, with slightly higher error at near grazing diffraction angles for the screen attributed to its thickness and the lack of second-order diffraction in the simulations.

In [170], Medwin *et al.* compared measurements (obtained from [30] and [111]) of insertion loss for a thin (0.48 cm) plate to BTM calculations. For a source at $\theta_S = 15°$, they show excellent agreement, with error below 1 dB between 4 and 40 kHz, using first-order diffraction simulations from an infinitely thin plate ($\theta_W = 360°$) when $\theta_R \leq 270°$. For $\theta_R \geq 270°$, they report an r.m.s. error near 4 dB for first-order diffraction simulations, but a reduction to 1 dB when the plate is modeled as two wedges with $\theta_W = 270°$ separated by a shared 0.48 cm face and second-order diffraction is included. They also provide comparisons for an alternate barrier design and a rigid strip, and similar agreement is seen when second-order diffraction is included.

In [110], Jebsen and Medwin studied backscatter from a plate ($\theta_W = 360°$) and a wedge ($\theta_W = 270°$) with a co-located source and receiver. They compared measurements to two types of predictions: one based on the BTM expression, and the other on the Helmholtz-Kirchhoff integral theorem simplified with the Kirchhoff assumption. They found good agreement with the former and significant errors with the latter.

Li and Clay [159] measured and simulated impulse responses in 12.07° and 52° plasterboard wedges. For the former, the choice of the wedge angle, for which $\theta_W \approx 180°/15$, resulted in very weak diffraction from the interior edge[4], and they used the measurements mainly to confirm the BTM predictions for the reflections from the wedge faces. For the latter, the measured and simulated impulse responses

[3]Typical results cited below have a low-frequency limit between 2 kHz and 5 kHz

[4]Wedges for which $\theta_W = \pi/m$ for integer values of m do not diffract [18, 129].

for a single source/receiver pair are presented for comparison. Visual inspection suggests a good match, and errors are attributed to the difficulty in constructing a "non-leaky" wedge apex. In addition, they provide data for a line of receivers that crosses a reflection boundary for a 270° wedge, and show high accuracy for the BTM simulations.

Li *et al.* [158] measured and simulated scattering from an angle iron on plasterboard, arranged to yield a wedge with $\theta_W = 270°$, and two wedges with $\theta_W = 135°$ where the faces of the angle iron met the plasterboard. Comparison of their results in the time-domain show good agreement for first-order and second order diffraction.

Chambers and Berthelot [36] studied the reflection boundaries for a step discontinuity (two horizontal surfaces offset with an 18-mm vertical surface, thus a 270° wedge sharing a face with a non-diffracting 90° wedge) and show comparisons in the time domain and at single frequencies for various receiver positions. While the comparison is largely qualitative, the results indicate that the BTM solution can predict the scattering from this geometry accurately in terms of amplitude, shape, arrival time, and polarity of the diffracted components.

Wadsworth and Chambers [285] used BTM-based simulations for the analysis of the insertion loss (IL) of 1:10-scale noise barriers and compared the results to measured IL values. Their test cases included a single knife-edge barrier ($\theta_W = 360°$), a wide barrier (two wedges with $\theta_W = 270°$ connected by a common face), and a double knife-edge barrier (two wedges with $\theta_W = 360°$ separated by a fixed distance). They found excellent agreement in IL between 2 and 20 kHz.

In the context of evaluating various diffraction-calculation methods, Ouis [202] presents a frequency-domain comparison of BTM-based simulations with measurements of diffraction from the edge of a 1-mm aluminum sheet mounted on a plywood base. No quantitative evaluation of the error is provided, but the measurements seem to support the predictions "quite favourably." In a later work, Ouis [204] measured and simulated diffraction from the edge of a 1.5-mm aluminum plate and presented time-domain and frequency-domain comparisons of the results for two source/receiver combinations. He found excellent agreement between 2 and 25 kHz, with some low-frequency error likely due to "poor performance of the sound source."

Menounou and You [172] studied various barrier configurations (*e.g.* straight edge and jagged edge) in part to validate the directive line-source model of diffraction

(DLSM, see also [171]), and compared spark-based measurements to DLSM and BTM simulations in the time-domain. The observed agreement among all three is quite good but not quantified.

A collection of papers has also been written on the so-called "facet-ensemble method" or "wedge-assemblage" (WA) method, which is based on BTM diffraction. In short, the method involves defining a surface (*e.g.* a one-dimensional sinusoid or a two-dimensional rough surface) as a collection of planar facets, then simulating the scattering from the surface by modeling the diffraction from the facet intersections (edges). Comparison of WA results with measured data and/or other numerical scattering models has shown good agreement, although the comparisons typically have been based on gross characteristics of the scattered field rather than the individual diffracted components. See [125, 126, 127, 128, 131, 132, 194] for further details.

Comparisons of diffraction measurements to simulations based on the line-integral BTM formulation from Svensson *et al.* [258] are limited. Torres *et al.* [265] present measured and simulated data for a scale-model stage house (made with reinforced acrylic). Their main goal is to show the importance of including diffraction in the simulations rather than to validate the BTM formulation, but the agreement is good, and discrepancies between the overall responses are largely ascribed to excess levels of the simulated specular reflections rather than inaccuracies in the diffraction computations. Løvstad and Svensson [164] presented measured data obtained from a 1:5 scale model of an orchestra pit, and compared them to simulations including first-order diffraction and specular reflections up to second order. The results, for a linear distribution of source positions, indicate good agreement between the two. However, the stated purpose of the paper was to suggest a benchmark case for simulations that include diffraction (the source is occluded from the receiver in many cases and the model contains numerous prominent diffracting edges), so the analysis of the comparison is limited to visual inspection of the data, and in particular the (correct) continuity of the simulated sound field when diffraction is included.

For a more explicit validation of the BTM line-integral formulation, Lokki *et al.* [160, 161] developed an experimental setup to isolate the diffraction from a single edge of a chipboard panel. Their measured and simulated results are presented in the time and frequency domains and again show good agreement. Factors such as non-rigidity of the panel, imperfect attenuation of diffraction from secondary edges,

and a non-ideal point source are suggested as the main causes for the differences in the measured and simulated data.

3.7.2 Comparison to Other Numerical Techniques

In addition to experimental validation, BTM expressions also have been the subject of comparison to other numerical diffraction solutions. In [125], Keiffer used pressure-release sinusoids to compare BTM-based diffraction calculations from the wedge-assemblage method to predictions from a method-of-moments formulation described in [261]. The agreement is quite good, and errors generally are attributed to the lack of multiple scattering in the WA method rather than the BTM solution itself. Keiffer *et al.* [128] compared Medwin's BTM formulation to a T-matrix solution for hard and soft discs. Results are generally excellent, and multiple diffraction is again identified as a critical component to obtain truly accurate results.

In [258], Svensson *et al.* compare simulations of axisymmetric scattering from rigid and soft discs using their line-integral BTM formulation to those in [128], and report a maximum error of 0.2 dB for the first-order diffraction amplitude relative to the T-matrix solution. They also report good agreement between their predictions for scattering from a rigid rectangular plate and previously published predictions for the same plate made with the boundary-element method [46]. A comparison of the frequency-domain formulation of the BTM line-integral expression to Pierce's exact frequency-domain expression [208] is shown in Section 3.6 above.

3.8 Limitations

One limitation of BTM diffraction is the lack of so-called slope diffraction terms. Slope diffraction is a phenomenon that arises when the incident field on an edge has a non-zero gradient, from which diffraction can arise even when the amplitude of the field is zero [12]. A common 2D example of this is a wedge insonified by a dipole, with the edge aligned with the null of the source; a diffracted field is present despite the zero-amplitude incident field. Slope diffraction plays a role in higher-order diffraction, where the diffracted field from one edge may result in an incident field on a subsequent edge with zero amplitude but a non-zero gradient. While

this concept is well studied in electromagnetics, and slope-diffraction terms for the UTD have been determined [12, 167], it remains relatively unexplored in acoustics. One exception is [250], in which Summers uses BTM diffraction to study the energy transfer between spaces in systems of coupled acoustic volumes, and notes that the lack of slope diffraction results in errors in the associated power transmission coefficients (but does not attempt to determine the appropriate expressions). Derivation of the slope-diffraction terms for the BTM formulation should be straightforward, and would allow a quantitative assessment of their importance in various simulation scenarios.

An additional shortcoming of BTM diffraction, as is common with many other expressions, is its restriction to ideal surfaces for the wedge faces. While experiments have shown good agreement between BTM-based simulations and measured results for various hard materials (as summarized in Section 3.7.1), an exact solution for diffraction from wedges with faces of arbitrary impedance is not yet known. The BTM method *has* been extended to apply to iso-velocity, density-contrast wedges [39, 40, 58, 79, 80, 193] (*i.e.* wedges for which the speed of sound is the same as that for the surrounding medium but the density is not), and this solution is applicable to ocean acoustics where the water and bottom surface meet the necessary criteria. However, the general case has yet to be solved, and it may be particularly applicable to environments commonly used in virtual-acoustic simulations such as concert halls, classrooms, offices, etc. that typically contain surfaces with varying degrees of frequency-dependent impedance.

Chapter 4

Diffraction Singularities at Reflection and Shadow Boundaries

4.1 Introduction

The sound field in the vicinity of a wedge is often analyzed in terms of its constituent parts: the geometrical-acoustics (GA) components, *i.e.* the direct sound and specular reflections, and the diffraction from the edge. With such a decomposition, singularities in mathematical expressions for the diffracted component are typically explained as necessary to compensate for the discontinuities in the GA field at the two shadow boundaries and at the two first-order reflection boundaries (one of each for each of the two wedge faces). However, these singularities result from periodic functions taking specific values, and thus can occur more than these commonly described four times. In this chapter, we address the singular behavior through the association of specific values of $\nu\varphi_i$ (see Eqs. 3.4 and 3.8) with specific zone boundaries. Higher-order reflection boundaries, which are relevant to the evaluation of sound fields near or within wedges for which the open angle is less than 180°, *i.e.* wedges that support multiple reflections between their faces, are discussed in detail. Analytical approximations to the BTM line-integral formulation, which address the singularities and allow for straightforward numerical implementations, also are described. Section 4.3 was published in modified form in [255].

4.2 Singular Behavior of the Diffraction Integrand

As mentioned in Section 3.4, Eq. (3.8), and thus the integrand in Eqs. (3.9) and (3.14) (time-domain and frequency-domain BTM formulations, respectively), is subject to a singularity when $\cosh(\nu\eta) = \cos(\nu\varphi_i) = 1$ for certain combinations of θ_S and θ_R.[1] $\cosh(\nu\eta) = 1$ for the shortest path from the source to the receiver via the line containing the diffracting edge, and thus the singularity occurs at the onset of the diffraction IR only when the apex point is included in the physical edge. $\cos(\nu\varphi_i) = 1$ when a receiver is on a reflection boundary or shadow boundary (hereafter collectively referred to as zone boundaries) associated with $\nu\varphi_i$, *i.e.* a location where a geometrical-acoustics component experiences a discontinuity. It is the cosine term that is of particular interest in this section. The BTM line-integral formulation is used for the following analysis, although the singular behavior at zone boundaries is characteristic of all diffraction expressions.

4.2.1 Singularities Related to the Direct Sound and First-Order Specular Reflections

The four terms of Eq. 3.9 typically are associated with the two shadow boundaries and two first-order reflection boundaries dictated by the wedge faces and shown in Figure 4.1. For a source with visibility to F_1 ($\theta_S < \pi$), the shadow boundary is located at $\theta_{SB} = \pi + \theta_S$. For a receiver located on this boundary (*i.e.* $\theta_R = \pi + \theta_S$),

$$\nu\varphi_2 = \nu[\pi + \theta_S - (\pi + \theta_S)] = 0. \tag{4.1}$$

The reflection boundary is located at $\theta_{RB} = \pi - \theta_S$, and for a receiver located on this boundary,

$$\nu\varphi_4 = \nu[\pi - \theta_S - (\pi - \theta_S)] = 0. \tag{4.2}$$

For a source with visibility to F_2 ($\theta_S > \pi$), the shadow boundary is located at $\theta_{SB} = \theta_S - \pi$. For a receiver located on this boundary,

$$\nu\varphi_3 = \nu[\pi - \theta_S + (\theta_S - \pi)] = 0. \tag{4.3}$$

[1] Since $\cosh(\nu\eta) \geq 1$ and $\cos(\nu\varphi_i) \leq 1$, the singularity can occur only when $\cosh(\nu\eta) = \cos(\nu\varphi_i) = 1$.

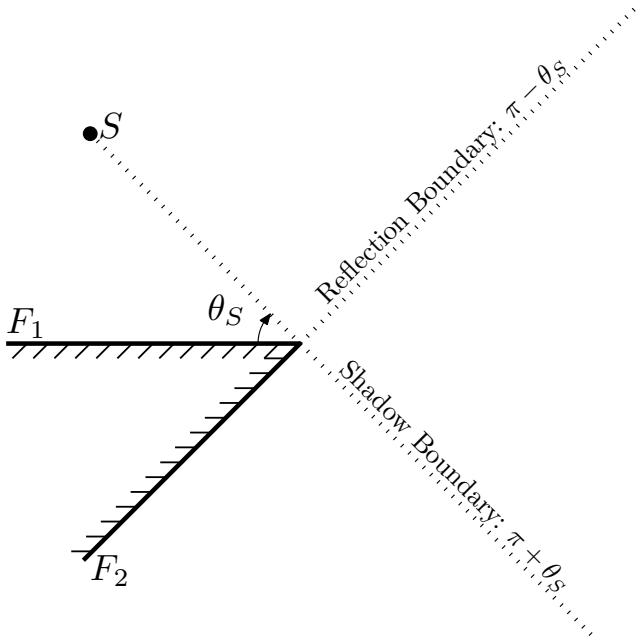

(a) $\theta_S < \pi$

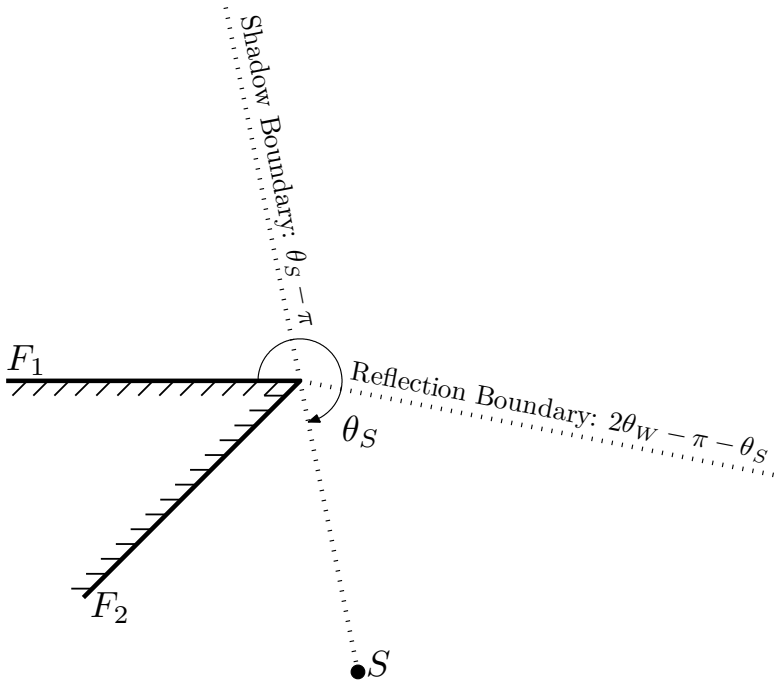

(b) $\theta_S > \pi$

Figure 4.1: Example geometry for the four basic singularity cases. (a) $\theta_S < \pi$: $\nu\varphi_2 = 0$ at the shadow boundary and $\nu\varphi_4 = 0$ at the reflection boundary. (b) $\theta_S > \pi$: $\nu\varphi_3 = 0$ at the shadow boundary and $\nu\varphi_1 = 2\pi$ at the reflection boundary.

The reflection boundary is located at $\theta_{RB} = 2\theta_W - \pi - \theta_S$, and for a receiver located on this boundary,

$$\nu\varphi_1 = \nu[\pi + \theta_S + (2\theta_W - \pi - \theta_S)] = \frac{\pi}{\theta_W} \cdot 2\theta_W = 2\pi. \tag{4.4}$$

For each of these, $\cos(\nu\varphi_i) = 1$ causes an onset singularity when the apex point is included in the physical edge.

An alternative method to identify the values of $\nu\varphi_i$ associated with singularities at reflection boundaries involves finding the angular coordinate of the image source that gives rise to the reflection, then evaluating the appropriate *shadow-boundary* condition for that image source. For example, the image source for a reflection from F_1 is located at $\theta'_S = -\theta_S$ (recall F_1 is in the $\theta = 0$ plane). Replacing θ_S with θ'_S in Eq. (4.1), the shadow-boundary condition for F_1, yields

$$\nu\varphi'_2 = \nu[\pi + \theta'_S - \theta_R] = \nu[\pi - \theta_S - \theta_R] = \nu\varphi_4 = 0, \tag{4.5}$$

a result equivalent to Eq. (4.2). Similarly, mirroring S about θ_W yields $\theta'_S = 2\theta_W - \theta_S$ for the image source associated with the first-order reflection from F_2 (recall F_2 is in the $\theta = \theta_W$ plane). Replacing θ_S with θ'_S in Eq. (4.3) yields

$$\begin{aligned} \nu\varphi'_3 \;\; = \;\; & \nu[\pi - \theta'_S + \theta_R] = 0 \\ & \nu[\pi - 2\theta_W + \theta_S + \theta_R] = 0 \\ & \pi + \theta_S + \theta_R = 2\theta_W \\ & \varphi_1 = 2\theta_W \\ & \nu\varphi_1 = 2\pi, \end{aligned} \tag{4.6}$$

which is equivalent to Eq. (4.4).

4.2.2 Singularities Related to Higher-Order Specular Reflections

To understand the first-order diffraction from a wedge completely, all possible singularities caused by $\cos(\nu\varphi) = 1$, *i.e.* all possible conditions for which $\nu\varphi_i = 2n\pi$ for integer values of n, must be considered. Using the image-source approach

Table 4.1: Geometrical-acoustics components associated with the four $\nu\varphi_i$ angles at $2n\pi$ for $n = 0, 1, 2, 3$.

	0	2π	4π	6π
$\nu\varphi_1$	N/A	$S \to F_2 \to R$	$S \to F_2 \to F_1 \to F_2 \to R$	$S \to F_2 \to F_1 \to F_2 \to F_1 \to F_2 \to R$
$\nu\varphi_2$	F_1 (Shadow)	$S \to F_2 \to F_1 \to R$	$S \to F_2 \to F_1 \to F_2 \to F_1 \to R$	$S \to F_2 \to F_1 \to F_2 \to F_1 \to F_2 \to F_1 \to R$
$\nu\varphi_3$	F_2 (Shadow)	$S \to F_1 \to F_2 \to R$	$S \to F_1 \to F_2 \to F_1 \to F_2 \to R$	$S \to F_1 \to F_2 \to F_1 \to F_2 \to F_1 \to F_2 \to R$
$\nu\varphi_4$	$S \to F_1 \to R$	$S \to F_1 \to F_2 \to F_1 \to R$	$S \to F_1 \to F_2 \to F_1 \to F_2 \to F_1 \to R$	$S \to F_1 \to F_2 \to F_1 \to F_2 \to F_1 \to F_2 \to F_1 \to R$

described above, higher-order reflection boundaries can be associated with the appropriate singularity-causing values of $\nu\varphi_i$, specifically for wedges with $\theta_W < 180°$ that can support second and higher-order reflections between their faces. For example, consider the reflection path $S \to F_2 \to F_1 \to R$. The corresponding image source is located at $\theta''_S = \theta_S - 2\theta_W$. Substituting this value into Eq. (4.1), the shadow-boundary condition for F_1, yields

$$\begin{aligned} \nu\varphi''_2 &= \nu[\pi + \theta''_S - \theta_R] = 0 \\ &\quad \nu[\pi + \theta_S - 2\theta_W - \theta_R] = 0 \\ &\quad \pi + \theta_S - \theta_R = 2\theta_W \\ &\quad \varphi_2 = 2\theta_W \\ &\quad \nu\varphi_2 = 2\nu\theta_W = 2\frac{\pi}{\theta_W}\theta_W = 2\pi. \end{aligned} \tag{4.7}$$

Similarly, the boundary for the reflection $S \to F_1 \to F_2 \to R$ corresponds to $\nu\varphi_3 = 2\pi$, and that for $S \to F_1 \to F_2 \to F_1 \to R$ corresponds to $\nu\varphi_4 = 2\pi$. Further values of $2n\pi$ and the associated reflection boundaries are given in Table 4.1.

The range of possible singularity-causing values of $\nu\varphi_i$ is a function of the wedge angle. With the faces at $\theta = 0$ and θ_W, the minimum value of θ_S and of θ_R is 0, and the maximum value for both is θ_W. This implies that the minimum and maximum

values of φ_i are

$$\varphi_{min} = \varphi_4\Big|_{(\theta_S=\theta_W,\theta_R=\theta_W)} = \pi - 2\theta_W,$$

$$\varphi_{max} = \varphi_1\Big|_{(\theta_S=\theta_W,\theta_R=\theta_W)} = \pi + 2\theta_W, \tag{4.8}$$

and the corresponding minimum and maximum values of $\nu\varphi_i$ are

$$\nu\varphi_{min} = \nu(\pi - 2\theta_W) = \nu\pi - 2\pi = (\nu - 2)\pi,$$

$$\nu\varphi_{max} = \nu(\pi + 2\theta_W) = \nu\pi + 2\pi = (\nu + 2)\pi. \tag{4.9}$$

The minimum value of ν is 1/2 (when $\theta_W = 2\pi$), therefore $\nu\varphi_{min} \geq -3\pi/2$ and a singularity due to $\nu\varphi_i \leq -2\pi$ will never occur. Thus, in general, values of $\nu\varphi_i$ for which a singularity *can* occur take the form

$$\nu\varphi_i = 2n\pi, n = 0, 1, ..., \left\lfloor \frac{\nu + 2}{2} \right\rfloor. \tag{4.10}$$

For a specific wedge, the lower bound for n is $\left\lceil \frac{\nu-2}{2} \right\rceil$. Note that $\nu\varphi_i = 0$ only occurs for $i = 2, 3, 4$ because $\nu > 0$ and $\varphi_1 = \pi + \theta_S + \theta_R > 0$.

4.2.3 Example Calculations

Consider a wedge with open angle $\theta_W = 75°$ and a source located at $r_S = 8$ m, $\theta_S = 50°$, $z_S = 0$ m. The behavior of the diffraction onset as a function of a receiver's angular position, θ_R, can be seen in Figure 4.2, for which a receiver with coordinates $r_R = 8$ m and $z_R = 0$ m has been swept through all possible angular positions. The wedge index for this case is $\nu = \pi/\theta_W = 2.4$, and thus Eqs. 4.9 and 4.10 predict that singularities can occur only for $\nu\varphi_i = 2\pi, 4\pi$. Two singularities are evident in Figure 4.2: one at $\theta_R = 20°$ for which $\nu\varphi_3 = 2\pi$, and the other at $\theta_R = 70°$ for which $\nu\varphi_1 = 4\pi$. Per Table 4.1, these are associated with the boundaries for the second-order reflection $S \rightarrow F_1 \rightarrow F_2 \rightarrow R$ and for the third-order reflection $S \rightarrow F_2 \rightarrow F_1 \rightarrow F_2 \rightarrow R$, respectively.

The example geometry is depicted in 2D in Figure 4.3 along with the behavior near the 20° reflection boundary. For the receiver R_1 with $\theta_R = 23°$ on the "illuminated" side of the boundary, the associated specular reflection is valid and

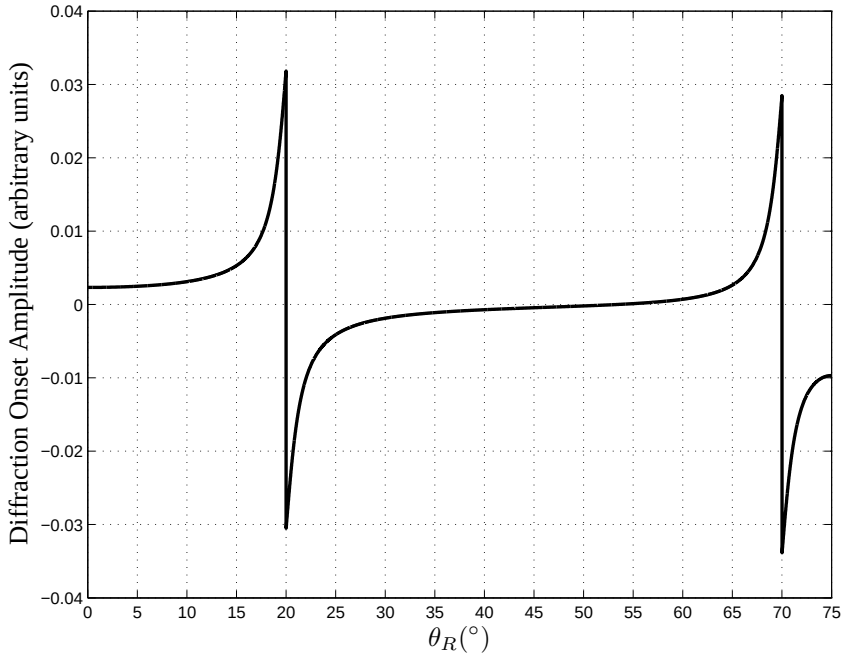

Figure 4.2: Onset diffraction amplitude as a function of the receiver angle for a 75° wedge and a fixed source at $S = 50°$ (geometry shown in Fig. 4.3). Note the effect of the singularities at 20° ($\nu\varphi_3 = 2\pi$) and 70° ($\nu\varphi_1 = 4\pi$).

its path is shown. For receiver R_2 with $\theta_R = 17°$ on the "shadowed" side of the boundary, the reflection is not valid. This can be seen by the line segment connecting the image source $I_{1,2}$ with R_2 that does not intersect face F_2 (intersection is a necessary condition for the validity of the reflection). The impulse responses at R_1 and R_2 are depicted in Figure 4.4. The loss of the reflection for R_2 is evident, as is the change in polarity of the diffraction component at the reflection boundary, also seen in Figure 4.2.

Similar behavior occurs at and near the reflection boundary at 70°. For a receiver with $\theta_R > 70°$, the reflection $S \rightarrow F_2 \rightarrow F_1 \rightarrow F_2 \rightarrow R$ exists and the diffraction polarity is negative. For $\theta_R < 70°$ the reflection does not exist and the diffraction polarity is positive.

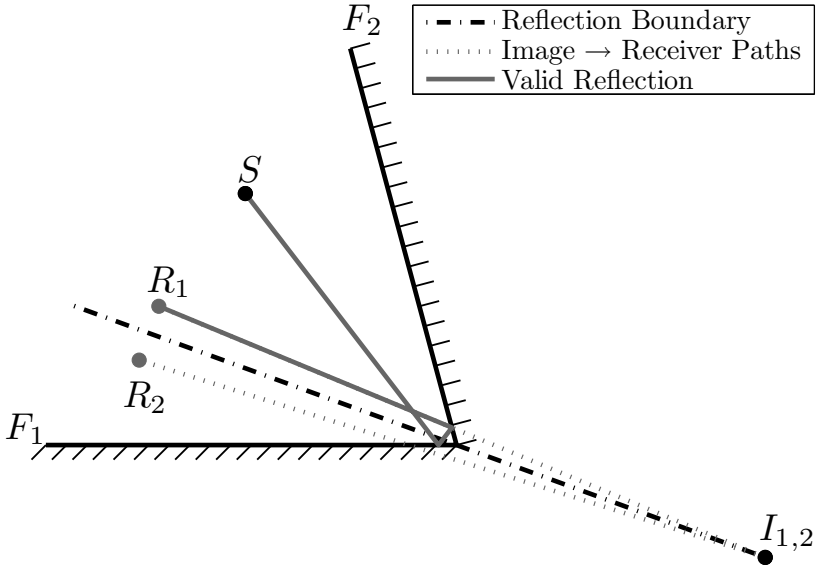

Figure 4.3: Example geometry: $\theta_W = 75°$, $\theta_S = 50°$, $\theta_{R_1} = 23°$, $\theta_{R_2} = 17°$ (with all angles measured clockwise from face F_1). The boundary shown at $\theta = 20°$ is for the second-order reflection $S \to F_1 \to F_2 \to R$. A valid reflection exists for receiver R_1 above the boundary, but not for R_2 below the boundary. See also Fig. 4.4.

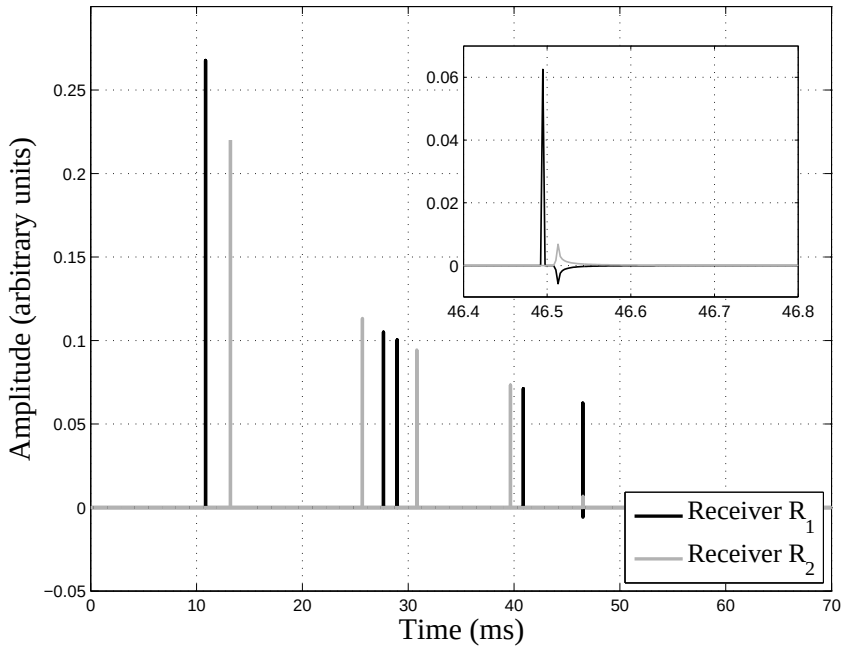

Figure 4.4: Impulse responses for the wedge, source S, and receivers R_1 and R_2 shown in Fig. 4.3. The main figure shows the full impulse responses. The inset, a zoomed-in view, shows the behavior of the $S \to F_1 \to F_2 \to R$ reflection and the diffracted component. For receiver R_1 the reflection exists and the diffraction polarity is negative. For receiver R_2 there is no reflection and the diffraction polarity has flipped to positive (also seen in Fig. 4.2).

4.3 Analytical Approximations to Address Zone-Boundary Singularities

As mentioned in Section 4.2, the denominator of the β_i functions only takes the value 0 when $\cosh(\nu\eta) = \cos(\nu\varphi_i) = 1$, and while the previous analysis of the singular behavior focused on the cos() term and its relationship to the proximity of a receiver to a zone boundary, the approximations described below are related to the cosh() term. Because $\cosh(\nu\eta) = 1$ for the shortest path from the source to the receiver via the line containing the diffracting edge, the singular behavior of the integrand occurs for $z-$values around the apex point, and this suggests an approximation approach that is valid and accurate around the apex point. If the apex point is within the physical edge, it is contained within the segment of the edge that contributes to the first sample of the diffraction IR, and the following approximations have been developed specifically for this first sample.[2] If the apex point falls outside of the edge, the approximations are not necessary and the entire edge can be processed with standard numerical-integration techniques.

4.3.1 Approximating the Diffraction Integrand

Given an edge, source, and receiver, the $z-$coordinate of the apex point is

$$z_a = \frac{z_R r_S + z_S r_R}{r_S + r_R}, \tag{4.11}$$

and an approximation of the integrand β_i/ml near the apex point can be made using a z-coordinate measured relative to z_a,

$$z_{rel} = z - z_a. \tag{4.12}$$

Approximations for $\cosh(\nu\eta)$ and ml can be derived for small values of z_{rel}, and with these the integrand β_i/ml can be approximated as

$$\frac{\beta_i}{ml} \approx B_0 \cdot \frac{1}{z_{rel}^2 + B_1} \cdot \frac{1}{z_{rel}^2 + B_2\ z_{rel} + B_3}, \tag{4.13}$$

[2]The application of the approximations to the first sample is a critical point in the development of edge subdivision strategies to reduce computation time that are addressed in Chapter 5.

where

$$
\begin{aligned}
B_0 &= \frac{4\ R_0^2\ \rho^3 \sin(\nu\varphi_i)}{\nu^2 (1+\rho)^4 \left[(1+\rho)^2 \sin^2\psi - 2\rho\right]}, \\
B_1 &= \frac{4R_0^2\ \rho^2 \sin^2\left(\frac{\nu\varphi_i}{2}\right)}{\nu^2 (1+\rho)^4}, \\
B_2 &= \frac{2\ R_0\ (1-\rho)\,\rho\ \cos\psi}{(1+\rho)\left[(1+\rho)^2 \sin^2\psi - 2\rho\right]}, \\
B_3 &= \frac{2\ R_0^2\ \rho^2}{(1+\rho)^2\left[(1+\rho)^2 \sin^2\psi - 2\rho\right]},
\end{aligned}
\tag{4.14}
$$

with the dimensionless quantity ρ defined as

$$
\rho = \frac{r_R}{r_S}, \tag{4.15}
$$

and the angle ψ defined such that

$$
\sin\psi = \frac{r_S + r_R}{R_0}, \quad \cos\psi = \frac{z_R - z_S}{R_0}, \tag{4.16}
$$

where R_0 is the distance from the source to the receiver via the apex point on the edge. The finite integral in Eq. (3.13), the discrete-time line-integral BTM expression, can be solved analytically when the integrand is given by Eq. (4.13). The solution is treated separately for symmetrical ($\rho = 1$ ($r_S = r_R$) or $\psi = \pi/2$ ($z_S = z_R$)) and asymmetrical cases separately in Sections 4.3.3 and 4.3.4, respectively, below.

4.3.2 Limits of Integration

Because the analytical approximation is needed only for the onset of the diffraction IR, the limits of integration for the approximation will typically be the z-values that delineate the portion of the edge that contributes to the first sample. Using z-coordinates relative to the apex point, one of these values will be negative (z_0^-) and the other positive (z_0^+), and thus for the first sample (n_0) Eq. (3.13) can be

written

$$\begin{aligned} h(n_0) &= -\frac{\nu}{4\pi}\sum_{i=1}^{4}\int_{z_0^-}^{z_0^+}\frac{\beta_i}{ml}dz_{rel} \\ &= -\frac{\nu}{4\pi}\left(\sum_{i=1}^{4}\int_{z_0^-}^{0}\frac{\beta_i}{ml}dz_{rel}+\sum_{i=1}^{4}\int_{0}^{z_0^+}\frac{\beta_i}{ml}dz_{rel}\right). \end{aligned} \tag{4.17}$$

It was shown in [258] that two segments on opposite sides of the apex point that contribute to the same sample (*e.g.* see Figures 3.3 and 5.4) do so equally, therefore

$$\sum_{i=1}^{4}\int_{z_0^-}^{0}\frac{\beta_i}{ml}dz_{rel}=\sum_{i=1}^{4}\int_{0}^{z_0^+}\frac{\beta_i}{ml}dz_{rel}, \tag{4.18}$$

which holds even for the asymmetrical case when $|z_0^-| \neq |z_0^+|$. Eq. (4.17) can now be restated

$$h(n_0) = -\frac{\nu}{2\pi}\sum_{i=1}^{4}\int_{0}^{z_0^+}\frac{\beta_i}{ml}dz_{rel}. \tag{4.19}$$

In what follows, the approximation is presented for the ith term of the summation in Eq. (4.19), written as a one-sided integral with a lower limit of 0 and an upper limit that is positive. Cases for which this form is not appropriate, or for which z_0^+ is not an appropriate choice for the upper limit of integration, are discussed in further detail in [255].

4.3.3 Approximation for the Symmetric Case

For a symmetric geometry, either $r_S = r_R$, *i.e.* $\rho = 1$, or $z_S = z_R$, *i.e.* $\psi = \pi/2$, and in both cases $B_2 = 0$ in Eq. (4.13). The integral that gives the first sample of the discrete-time IR, $h(n_0)$, is the sum of the four IR terms denoted $h_i(n_0)$, and the ith term is

$$h_i(n_0) \approx -\frac{\nu}{2\pi}\cdot\frac{B_0}{B_3-B_1}\cdot\int_0^{z_{range}}\left(\frac{1}{z_{rel}^2+B_1}-\frac{1}{z_{rel}^2+B_3}\right)dz_{rel}, \tag{4.20}$$

where z_{range} is typically z_0^+, the z-coordinate of the point on the edge corresponding to $\tau = (n_0 + 0.5)/f_S$, as described in Section 3.5. The result of this integration is

$$h_i(n_0) \approx -\frac{\nu}{2\pi} \cdot \frac{B_0}{B_3 - B_1} \left[\frac{\arctan\left(\frac{z_{range}}{\sqrt{B_1}}\right)}{\sqrt{B_1}} - \frac{\arctan\left(\frac{z_{range}}{\sqrt{B_3}}\right)}{\sqrt{B_3}} \right]. \tag{4.21}$$

A special case of the symmetrical situation occurs when $\rho = 1$ *and* $\psi = \pi/4$, for which the integrand β_i/ml further simplifies to

$$\frac{\beta_i}{ml} \approx \frac{B_4}{z_{rel}^2 + B_1}, \tag{4.22}$$

where

$$B_4 = \frac{B_0}{B_3} = \frac{\sin(\nu\varphi_i)}{2\nu^2}. \tag{4.23}$$

The result of the integration in this case is

$$h_i(n_0) \approx -\frac{\nu}{2\pi} \cdot \frac{B_4}{\sqrt{B_1}} \cdot \arctan\left(\frac{z_{range}}{\sqrt{B_1}}\right). \tag{4.24}$$

4.3.4 Approximation for the Asymmetric Case

For the general, asymmetrical case, the integral form for the ith term of the first sample of the diffraction IR is

$$h_i(n_0) \approx \frac{\nu}{2\pi} \cdot \frac{B_0 B_2}{B_1 B_2^2 + (B_1 - B_3)^2} \cdot$$

$$\int_0^{z_{range}} \left[\frac{z_{rel} + (B_1 - B_3)/B_2}{z_{rel}^2 + B_1} - \frac{z_{rel} + (B_1 - B_3 + B_2^2)/B_2}{z_{rel}^2 + B_2 z_{rel} + B_3} \right] dz_{rel}. \tag{4.25}$$

The result of this integration is

$$h_i(n_0) \approx \frac{\nu}{2\pi} \cdot \frac{B_0 B_2}{B_1 B_2^2 + (B_1 - B_3)^2} \cdot \left[\frac{1}{2} \ln \left| \frac{B_3\left(z_{range}^2 + B_1\right)}{B_1\left(z_{range}^2 + B_2 z_{range} + B_3\right)} \right| \right.$$

$$\left. + \frac{B_1 - B_3}{\sqrt{B_1}\, B_2} \arctan\left(\frac{z_{range}}{\sqrt{B_1}}\right) + \frac{2(B_3 - B_1) - B_2^2}{2B_2} F \right], \tag{4.26}$$

where F can take one of four forms depending on the quantity

$$q = 4B_3 - B_2^2. \tag{4.27}$$

For $q < 0$ and finite, form I should be used, where

$$F_I = \frac{1}{\sqrt{-q}} \ln \left[\left| \left(\frac{2z_{range} + B_2 - \sqrt{-q}}{2z_{range} + B_2 + \sqrt{-q}} \right) \cdot \left(\frac{B_2 + \sqrt{-q}}{B_2 - \sqrt{-q}} \right) \right| \right], \tag{4.28}$$

and for $q > 0$ and finite, form II should be used, where

$$F_{II} = \frac{2}{\sqrt{q}} \left(\arctan \frac{2z_{range} + B_2}{\sqrt{q}} - \arctan \frac{B_2}{\sqrt{q}} \right). \tag{4.29}$$

When $q = 0$, the third form is

$$F_{III} = \frac{4\ z_{range}}{B_2\ \ (2z_{range} + B_2)}. \tag{4.30}$$

The fourth form, to be used when the denominator of q goes to zero, is

$$F_{IV} = 0. \tag{4.31}$$

When q is written

$$q = \frac{4R_0^2\rho^2 \left[2\left(1+\rho^2\right) - \cos^2\psi \left(1 + 6\rho + \rho^2\right) \right]}{\left(1+\rho\right)^2 \left[\left(1+\rho\right)^2 \sin^2\psi - 2\rho \right]}, \tag{4.32}$$

it is clear that the denominator will be zero when

$$\sin^2\psi = \frac{2\rho}{\left(1+\rho\right)^2}, \tag{4.33}$$

or, equivalently, when

$$\rho = \cot^2\psi \cdot \left(1 \pm \sqrt{1 - \tan^4\psi} \right). \tag{4.34}$$

F_{IV} can be used directly in Eq. (4.26); however an alternative formulation of Eq. (4.25) is numerically more suitable in this case,

$$h_i(n_0) \approx \frac{\nu}{\pi} \cdot \frac{B_5}{B_1 + B_6^2} \cdot \int_0^{z_{range}} \left(\frac{z_{rel} - B_6}{z_{rel}^2 + B_1} - \frac{1}{z_{rel} + B_6} \right) dz_{rel}. \tag{4.35}$$

The result of this integration is

$$h_i(n_0) \approx \frac{\nu}{2\pi} \cdot \frac{B_5}{B_1 + B_6^2} \cdot \left[\frac{1}{2} \ln \left| \frac{B_6^2 (z_{range}^2 + B_1)}{B_1 (z_{range} + B_6)^2} \right| - \frac{B_6}{\sqrt{B_1}} \arctan \left(\frac{z_{range}}{\sqrt{B_1}} \right) \right], \quad (4.36)$$

where

$$B_5 = \frac{B_0}{B_2} = -\frac{2\ R_0\ \rho^2 \sin(\nu\varphi_i)}{\nu^2 (1+\rho)^3 (1-\rho)\ \cos\psi}, \quad (4.37)$$

and

$$B_6 = \frac{B_3}{B_2} = -\frac{R_0\ \rho}{(1-\rho^2)\ \cos\psi}. \quad (4.38)$$

There is no risk that the denominator of B_5 or B_6 will take the value zero, since that can happen only for the symmetrical cases $\rho = 1$ and $\psi = \pi/2$ which have been addressed separately.

4.3.5 Limit Value for the Approximations

To address the singular behavior for receivers at or near zone boundaries described in Section 4.2, the approximations must be evaluated in the limit as $\cos(\nu\varphi_i)$ approaches 1, *i.e.* as the angle $\nu\varphi_i$ approaches $2n\pi$ for $n = 0, 1, 2....$ The approach must be considered from both sides of the boundary, *i.e.* as $\nu\varphi_i \to 2n\pi^+$ and $\nu\varphi_i \to 2n\pi^-$. For Eqs. (4.21) and (4.24), the finite limit value is

$$\lim_{\nu\varphi_i \to 2n\pi^\pm} h_i(n_0) = \mp \frac{1}{2\ R_0}. \quad (4.39)$$

This is an interesting limit value since it shows that as the receiver approaches a zone boundary, the diffraction IR will tend toward a pulse (since the IR value in the first time sample will dominate the values in the following samples due to the singularity) with an amplitude that is half that of the GA component associated with that boundary. On the "illuminated" side of the boundary, *i.e.* where the direct sound or specular reflection reaches the receiver, the geometrical component and the diffraction IR will have opposite polarities, with amplitudes of $1/R_0$ and $-1/(2R_0)$, respectively, and thus at the boundary will fuse into a single pulse with amplitude $1/(2R_0)$. Just beyond the zone boundary, the diffraction IR maintains the amplitude of $1/(2R_0)$ while the GA component disappears, and thus the total sound field is continuous across the boundary. The limit value in Eq. (4.39) is

consistent with the one reported by Kinney *et al.* in [132], although Clay and Kinney suggest in [43] that the limit is in fact zero.

This limit value suggests three possible interpretations for the values of the diffraction IR and the geometrical component when the receiver is located exactly on a zone boundary. To maintain continuity of the sound field, the GA component and the diffraction IR onset can be assigned amplitudes $1/R_0$ and $-1/(2R_0)$, $1/(2R_0)$ and 0, or 0 and $1/(2R_0)$ respectively for such cases. It may be that this choice of interpretation lead to the apparently conflicting results in [132] and [43]. Li and Clay [159] provide experimental evidence that the first interpretation is the correct one, although it is not clear how precisely one can place a receiver on a zone boundary in an experimental setup.

4.3.6 Application of the Approximation to the Frequency-Domain Formulation

With slight modification to the integration limit, the approximations described above for the time-domain line-integral formulation also are applicable to the frequency-domain formulation. For a symmetric case, the integration range z_1 to z_2 is split into two sub-ranges: one in the vicinity of the apex point, up to a point that can be denoted z_{split}, and one for the remainder of the edge. For such a case the presentation can be simplified by assuming $z_a = 0$ with a wedge that extends symmetrically to an end-point of z_2 so that the integration range can be halved. With these assumptions, Eq. (3.14) becomes

$$\begin{aligned} H_{diffr}(\omega) &= I_1 + I_2 \\ &= -2\frac{\nu}{4\pi}\sum_{i=1}^{4}\int_0^{z_{split}} e^{-jk(m+l)}\frac{\beta_i}{ml}\,dz \\ &\quad -2\frac{\nu}{4\pi}\sum_{i=1}^{4}\int_{z_{split}}^{z_2} e^{-jk(m+l)}\frac{\beta_i}{ml}\,dz. \end{aligned} \tag{4.40}$$

The second integral has no singularities and can be handled with ordinary numerical-integration techniques. The first integral is solved using the analytical approxima-

tion described above, with a small modification. I_1 can be written

$$I_1 = -2\frac{\nu}{4\pi}e^{-jk(m_0+l_0)}\sum_{i=1}^{4}\int_0^{z_{split}} e^{-jk(m-m_0+l-l_0)}\frac{\beta_i}{ml}\,dz, \tag{4.41}$$

where m_0 and l_0 are distances from the apex point to the source and to the receiver, respectively. If z_{split} is chosen such that

$$e^{-jk(m-m_0+l-l_0)} \approx 1, \tag{4.42}$$

then

$$I_1 \approx -2\frac{\nu}{4\pi}e^{-jk(m_0+l_0)}\sum_{i=1}^{4}\int_0^{z_{split}} \frac{\beta_i}{ml}\,dz, \tag{4.43}$$

and the analytical approximation can be used directly for the integral. In order to fulfill Eq. (4.42), it is required that

$$k(m - m_0 + l - l_0) \ll 1, \tag{4.44}$$

which leads to

$$z_{split} \ll \sqrt{\frac{2m_0l_0(m_0+l_0)}{k(r_S+r_R)^2}}. \tag{4.45}$$

In addition, the analytical approximations for β_i/ml require that

$$z_{split} \ll m_0, \qquad z_{split} \ll l_0. \tag{4.46}$$

For the asymmetric case in which the apex point is included in the wedge, three integration sub-ranges are necessary: one covering a small portion of the edge around the apex point, and one extending from this "apical" region to each of z_1 and z_2.

4.4 Summary

In this chapter the singular behavior of diffraction expressions near geometrical-acoustics zone boundaries has been discussed, with examples and analysis provided in the context of the BTM line-integral formulation. For wedges with an open angle greater than 180°, four boundaries and thus four singularities are possible: a

shadow boundary and a specular-reflection boundary associated with each face. Wedges with an open angle less than 180° can support higher-order reflections between their faces, and the boundaries for these reflections cause discontinuities in the GA sound field just as the more commonly studied shadow boundaries and first-order reflection boundaries do. The singularity in the diffraction from the edge of the wedge is necessary to maintain a continuous sound field where the geometrical-acoustics components are discontinuous, and the periodicity of the singular behavior, encoded in the $\cos(\nu\varphi_i)$ term in the BTM expression, ensures this continuity across all reflection boundaries.

Also described here is an analytical approximation for the first sample of a discrete-time diffraction impulse response that can be used to address the singularities in numerical implementations. The approximation is developed for the integrand of the line-integral expression along a small section of the edge that includes the apex point. A finite limit value for the approximation is given, and using this limit it has been shown that the approximation maintains a continuous sound field across zone boundaries when combined with geometrical-acoustics components.

Chapter 5

Reducing Diffraction Computation Time with Edge Subdivision

5.1 Introduction

Diffraction calculations can be quite time consuming, a problem that may be exacerbated by complex virtual environments with many edges and/or by interactive simulations that require fast update rates. Existing modeling systems such as those described in [85, 271] address this constraint by using various simplifications and approximations with an approach based on the Uniform Theory of Diffraction (UTD) [137]. While the line-integral BTM formulation would offer higher accuracy for finite edges and sources/receivers in close proximity to edges, its computational complexity thus far has restricted its use to static scenarios and off-line calculations.

In this chapter, we describe a technique that allows for fast calculations of edge-diffraction impulse responses based on the BTM line-integral formulation. The integration along the diffracting edge suggests a calculation approach in which the edge can be subdivided into segments for processing. Our technique uses a hybrid of two types of segments: sample-aligned segments, each of which contributes to exactly one sample of the discrete-time diffraction IR; and large, evenly sized segments that contribute to multiple IR samples. The former provide a high level of accuracy, but their boundaries are relatively slow to compute and must be updated when the source or receiver is moved. Therefore, we use them only for a small

part of the edge that contributes a significant portion of the total diffracted energy to the early part of the IR. The latter (even) segments introduce some error, but their boundaries are independent of the source and receiver positions and can be computed quickly in a preprocessing step for use with the diffraction-IR tails. The subdivision process, and the trade-off between accuracy and computation time, can be controlled with a number of parameters, allowing the user to find an appropriate balance between speed and error for a specific modeling scenario.

In the remainder of this chapter, Section 5.2 describes the subdivision schemes, and Section 5.3 addresses the various parameters available for adjusting the speed and accuracy of the diffraction calculations. Section 5.4 presents example calculations along with timing and accuracy statistics. Portions of this chapter were published in modified form in [32] and [34].

5.2 Edge Subdivision Strategies

We initially consider two basic edge-subdivision strategies to calculate discrete-time edge-diffraction IRs: subdivision into sample-aligned segments, and subdivision into evenly sized segments. The former was introduced in [258] and described in Section 3.5, and the latter also was discussed briefly in [258]. A third method, which is a hybrid of these two, is proposed and evaluated here as well.

5.2.1 Subdivision into Sample-Aligned Segments

As discussed in Section 3.5, sample-aligned segments correspond to portions of an edge that lie between intersections of that edge with two confocal ellipsoids determined by the source and receiver locations, and the distances $c(n \pm 0.5)/F_S$, where F_S is the sampling frequency and n is the sample index. With such boundaries, each segment contributes to exactly one sample of the discrete-time diffraction IR. 2D examples are shown in Figure 3.3, and an additional example is provided in Figure 5.1.

Sample-aligned segments are advantageous for many reasons. First, despite the low-pass filtering implied by the area sampling in Eq. (3.13) (the discrete-time diffraction IR with sample-aligned segments), the spectrum of the discrete-time IR

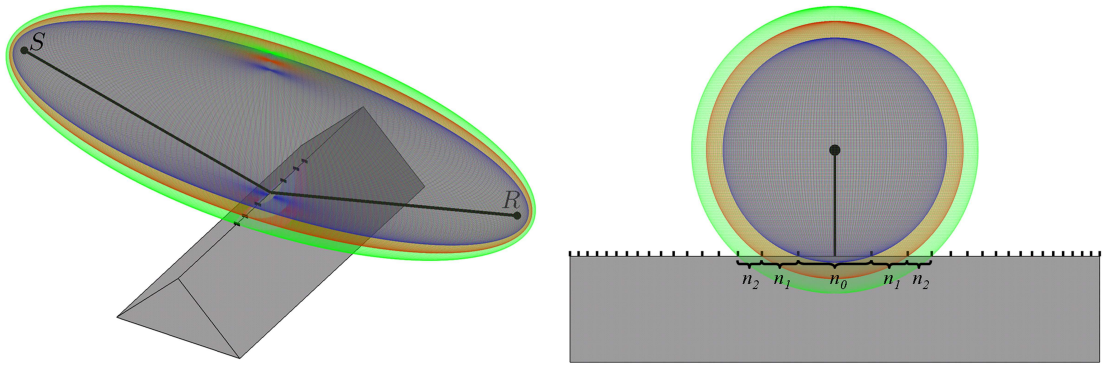

(a) (b)

Figure 5.1: Sample-aligned edge subdivision. Segment boundaries are determined by the intersections of the edge with ellipsoids whose foci are the source and receiver and whose dimensions are given by the travel distance associated with a particular sample in the discrete-time diffraction IR.

can be made to match that of the exact continuous-time IR up to a chosen frequency by using a sufficiently high sampling rate. Clay and Kinney [43] recommend a minimum sampling rate of four times the highest frequency of interest for analysis, which suggests using $F_S \geq 80$ kHz for applications in acoustics concerned with the audible spectrum of sound. Second, these segments can be used easily with the analytical approximations for sample n_0 described in Section 4.3 to avoid the onset singularity because the boundaries corresponding to that sample are given explicitly. Finally, the per-segment processing is straightforward: each segment's contribution is calculated using either numerical integration or the analytical approximation, and the result is added to the corresponding sample of the IR.

Sample-aligned segments unfortunately are not practical for interactive simulations because of the associated computational demands. The segment-boundary calculations are time consuming, the boundaries must be recalculated when the source or receiver is moved, and high sampling frequencies often result in prohibitively high segment counts. Furthermore, the segments are sample-aligned for first-order diffraction IRs only, and thus the benefits do not extend to higher orders of diffraction.

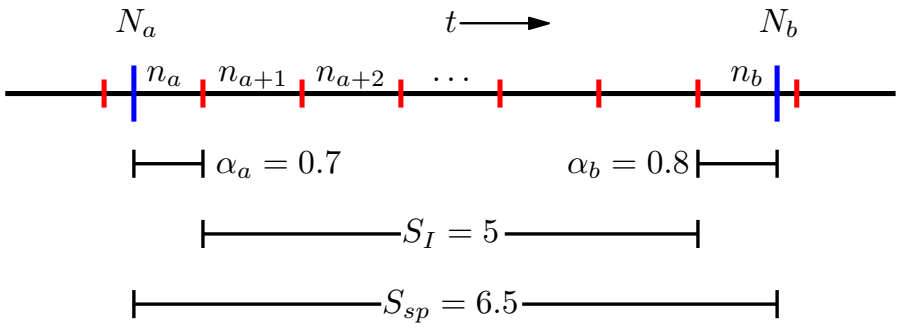

Figure 5.2: Example values used for multi-sample distribution. Sample boundaries are shown in red. Segment boundaries, expressed as real-valued sample numbers, are shown in blue.

5.2.2 Subdivision into Evenly Sized Segments

Evenly sized segments for an edge of length L are generated by choosing a maximum length Δz, and subdividing the edge into k segments of length l where $k = \lceil L/\Delta z \rceil$ and $l = L/k$. The segment boundaries are easily calculated and are independent of the source and receiver locations; thus they can be calculated once in a simple pre-processing step. However, excessively large values of l or Δz can introduce significant errors in the resulting IR, while small values may result in a prohibitively large number of segments to process. Per-segment processing is somewhat more complicated than with sample-aligned subdivision because each segment may contribute to multiple IR samples. For each segment, the group of corresponding samples must be determined, and the total segment contribution must be calculated and then spread appropriately across these samples. Finally, the boundaries corresponding to sample n_0 are not given explicitly, making it more difficult to avoid the onset singularity.

When using evenly sized segments that contribute to multiple IR samples, the amplitude value A obtained by integrating over the length of a segment must be distributed accordingly. Let the path lengths from the source to the receiver through the endpoints of a segment be p_a and p_b with $p_b > p_a$, which correspond to real-valued sample numbers $N_a = p_a \cdot F_S/c$ and $N_b = p_b \cdot F_S/c$, and integer sample numbers $n_a = \text{round}(N_a)$ and $n_b = \text{round}(N_b)$, respectively. The sample span for the segment is then $S_{sp} = N_b - N_a$, which comprises $S_I = n_b - n_a - 1$ complete inner samples and two fractional outer samples. For the latter, the fractions "covered" by the segment are $\alpha_a = n_a - N_a + 0.5$ and $\alpha_b = N_b - n_b + 0.5$. An example is shown in Figure 5.2. A simple, flat distribution of A over the sample span results

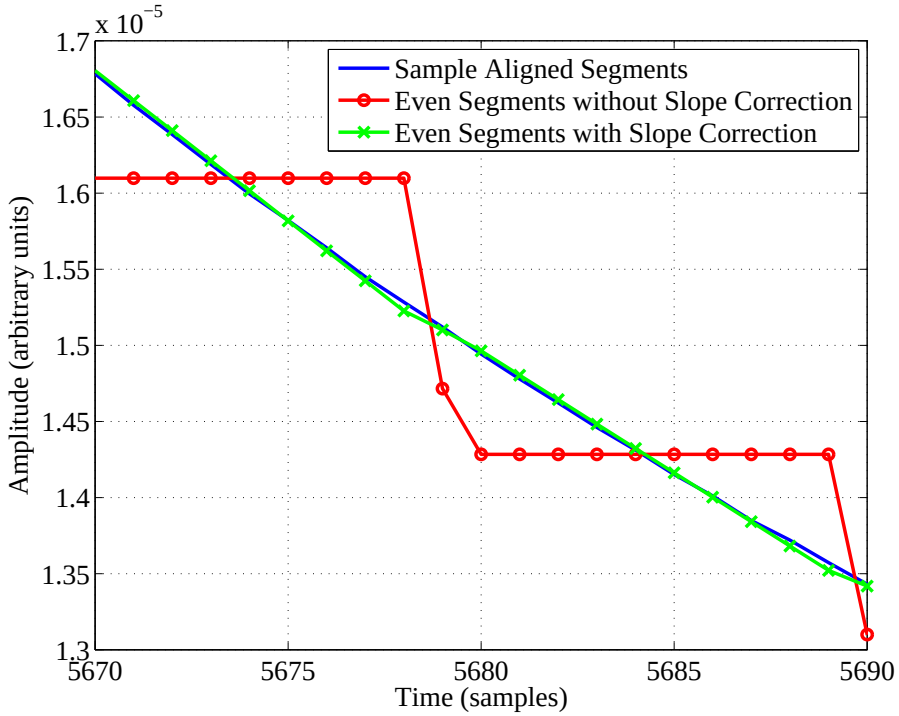

Figure 5.3: Multi-sample distribution for evenly sized segments, with and without the slope correction that assumes the impulse response has a locally linear decay.

in $\alpha_a \cdot A/S_{sp}$ in sample n_a, $\alpha_b \cdot A/S_{sp}$ in sample n_b, and A/S_{sp} in each of the S_I inner samples.

The fact that consecutive inner samples are given the same value leads to a staircase effect in the impulse response as can be seen in Figure 5.3. To remedy this, it is possible to weight the sample contributions for a segment with the local slope of the IR. Consider two adjacent multi-sample segments, with respective total amplitudes A_1 and A_2 and sample spans S_{sp1} and S_{sp2}. With the flat distribution method described above, the middle sample associated with the first segment will be given the value A_1/S_{sp1}, and that associated with the second segment A_2/S_{sp2}. Under the assumption that the IR is locally linear, the slope s between the two middle samples can be calculated, and the distribution of A_2 can be adjusted such that the slope over S_{sp2} is equal to s. An example of the slope correction can be seen in Figure 5.3.

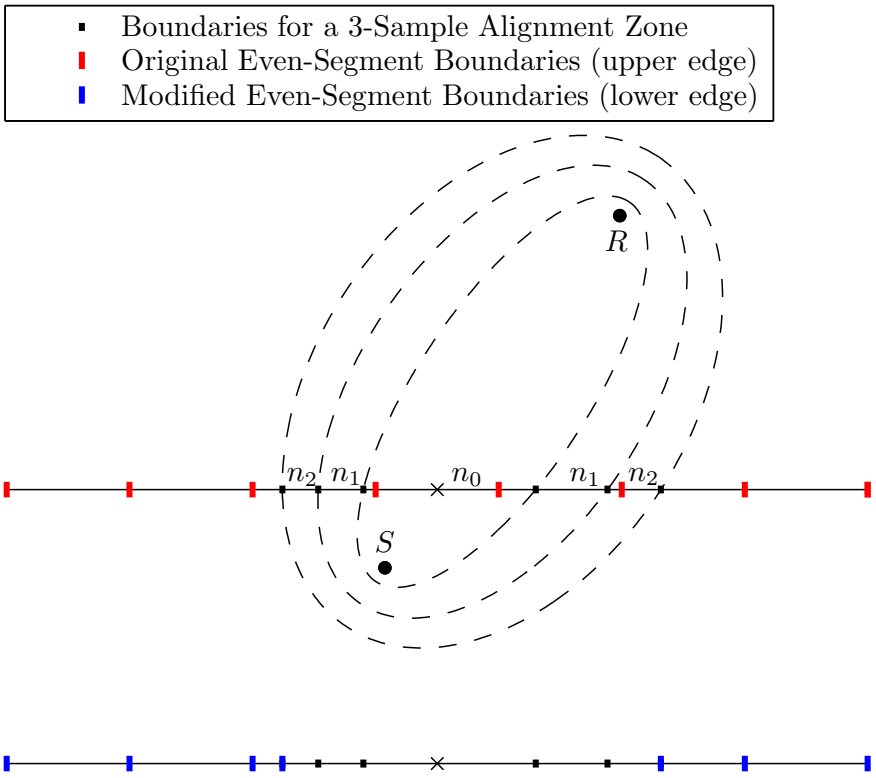

Figure 5.4: Unfolded 2D view of a source, receiver, and segmented edge. The upper edge is marked with the boundaries for a 3-sample alignment zone (samples n_0, n_1, and n_2) in black and the original even-segment boundaries in red. The lower edge (S and R not shown) is marked with the modified segment boundaries for the hybrid subdivision scheme in blue: even segments overlapping the alignment zone have been truncated at the edges of the zone, and those completely within the alignment zone have been discarded. The apex point is marked with an 'x'.

5.2.3 Hybrid Subdivision Strategy

A hybrid subdivision strategy can be used to exploit some of the benefits of both sample-aligned and evenly sized segments. With this method, a small number of sample-aligned segments is used to calculate the first N samples of the diffraction impulse response, and evenly sized segments are used to process the remainder of the edge. Any portion of an evenly sized segment that overlaps the alignment zone (*i.e.* would contribute to any of the first N samples) is discarded. An example of hybrid subdivision with $N = 3$ is shown in Figure 5.4. If the source or receiver is moved, the boundaries for the first N segments must be recalculated and the alignment-zone overlap tests must be repeated, but this is far less time consuming than recalculating sample-aligned boundaries for the entire edge.

5.3 Calculation Parameters

Given the hybrid subdivision method described above, our goal is to minimize the diffraction processing time while limiting the error in the calculations. Three parameters provide control over the accuracy and timing: the number of samples in the alignment zone; the size of the evenly sized segments; and the integration technique used to calculate the contribution of each segment, which can be chosen independently for the alignment zone and the even segments.

5.3.1 Size of the Alignment Zone

Because diffraction impulse responses tend to have an impulsive onset followed by a rapidly decaying tail, the high-frequency response is governed by the early samples. The low-frequency response is determined by the total integral over the entire edge, but this value also is strongly dependent on the early part of the IR which has a high amplitude relative to that of the tail. Therefore, accurate computation of the early part of a diffraction IR is critical for an accurate reproduction of its broadband spectral content and thus its perceptual characteristics. Our implementation of the hybrid edge-subdivision scheme allows for an alignment zone of arbitrary size, although as described in Section 5.4 the use of as few as 4 sample-aligned segments can be sufficient for results with low spectral error.

5.3.2 Segment Size

The size of the even segments is given in terms of the maximum number of IR samples, n_S, to be spanned by any one segment, and converted to a length using

$$\Delta z = \frac{n_S \cdot c}{F_S}, \tag{5.1}$$

where c is the speed of sound and F_S is the sampling frequency. In practice, the actual sample span of most segments is well below the specified upper bound of n_S. A single value of Δz is used for all edges in a given modeling environment. As Δz increases, computation time decreases due to fewer calls of the integration function, and accuracy decreases because each segment's diffraction contribution

must be distributed over a larger span of samples, and the assumption of a locally linear slope over such a span becomes less valid.

5.3.3 Numerical Integration Technique

Our implementation provides a choice of three numerical integration techniques: 5-point compound Simpson's rule integration with one step of Romberg extrapolation, standard 3-point Simpson's rule integration, and 1-point midpoint integration [59]. Because the integrand, β_i/ml, includes one hyperbolic and two standard trigonometric functions (see Eq. (3.8)), a reduction of the number of points at which it must be evaluated can lower the total processing time significantly for multi-edge environments, albeit with a corresponding reduction in accuracy. Any of the three techniques can be chosen for the alignment zone and for the evenly sized segments independently. However, the relative importance of the early part of the diffraction IR suggests that combinations in which the integration technique for the alignment zone is equal to or more accurate than that for the evenly sized segments will yield the best results.

5.4 Results

For the following results, all processing was done on a desktop computer with a 3.2-GHz Pentium 4 processor and 2 gigabytes of RAM. The sampling rate for all simulations was 96 kHz.

5.4.1 Calculations for a Single Edge

We initially evaluated the subdivision approaches with a simple, single-edge geometry. The calculations were made using sample-aligned subdivision as well as the hybrid subdivision strategy with a one-sample alignment zone, with and without the slope-correction for multi-sample distributions. Figure 5.5(a) contains IRs calculated for a 6 m edge with $\theta_W = 270°$. The coordinates of the source were $r_S = 10$ m, $\theta_S = 53°, z_S = 0$ m, and those of the receiver were $r_R = 10$ m, $\theta_R = 157.5°, z_R = 0$ m, with the apex point 4 m from one end of the edge. Results

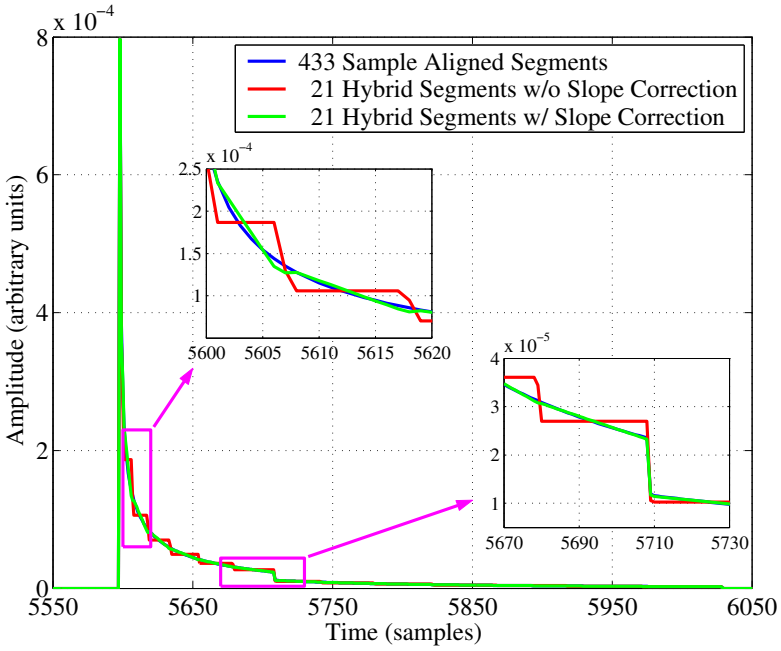

(a)

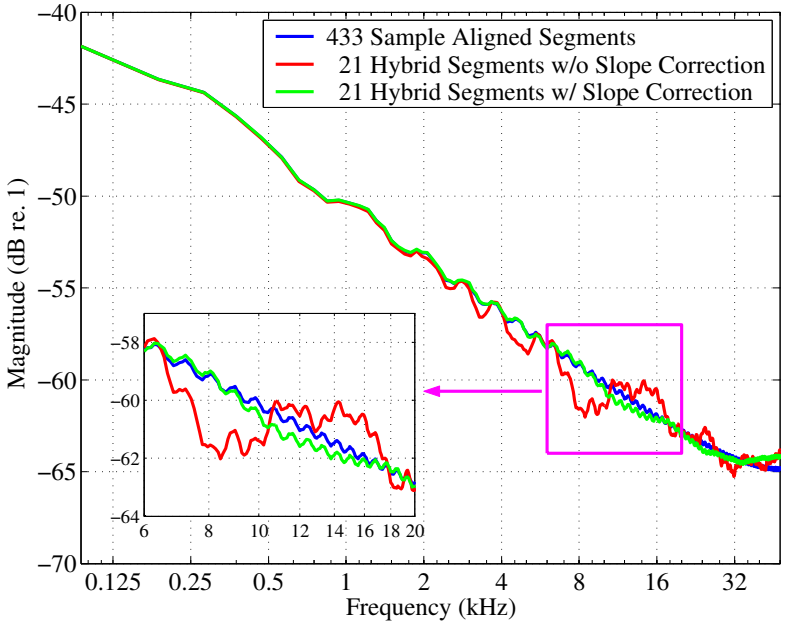

(b)

Figure 5.5: Results for the single-edge example. (a) Impulse responses: Note the improved performance of the slope correction in the later part of the IR (right inset vs. left). (b) Magnitude spectra.

using strictly evenly sized segments are not shown because the apex point is included in the edge, and even segments do not allow for proper numerical handling of the

associated onset singularity. For all cases, the apex sample was calculated with the approximations described in Section 4.3 and numerical integration was done for each non-apex segment with one iteration of 5-point extended Simpson's rule quadrature. The maximum length of the evenly sized segments used with the hybrid strategy was set such that the total number of segments needed to cover the edge (21) was reduced by a factor of approximately 20 from the sample-aligned total (433). The insets in Figure 5.5(a) show close-up views of the diffraction IRs, and it can be seen that the performance of the slope correction improves as the IR becomes more linear with increasing elapsed time. Using the hybrid method, the processing times (averaged over 1000 trials) were reduced from 3.329 ms (sample-aligned) to 0.194 ms (hybrid, no slope correction) and 0.199 ms (hybrid, with slope correction). The fact that these reductions in time, by factors of 17.1 and 16.8, respectively, do not match the factor of 20 reduction in segment number is not surprising, because the per-segment processing time is higher for the hybrid subdivision strategy than for the sample-aligned subdivision strategy.

Figure 5.5(b) contains the magnitude spectra of the IRs in Figure 5.5(a). Below 20 kHz, the maximum difference between the sample-aligned spectrum and the hybrid spectrum without slope correction is 2.4 dB. This difference is reduced to 0.6 dB when the slope correction is used. Deviations above 20 kHz are unlikely to be audible. The excellent agreement among all three spectra at low frequencies is a result of computing the integral accurately for each segment.

The IRs shown in Figure 5.5(a) are typical of general source and receiver locations, so the level of accuracy achieved for this example can be expected for a wide range of configurations. However, there are conditions under which the IR will be more impulsive or can have a zero crossing, for example when the source and receiver are very close to the edge or when the receiver is near a shadow-zone boundary. With such cases, it may be necessary to use multiple sample-aligned segments for the early part of the IR, or smaller evenly sized segments to simulate the IRs accurately.

5.4.2 Calculations for an Array of Rectangular Panels

To evaluate further the effect of the subdivision parameters on the computation of diffraction impulse responses, we simulated the diffraction from an array of rigid,

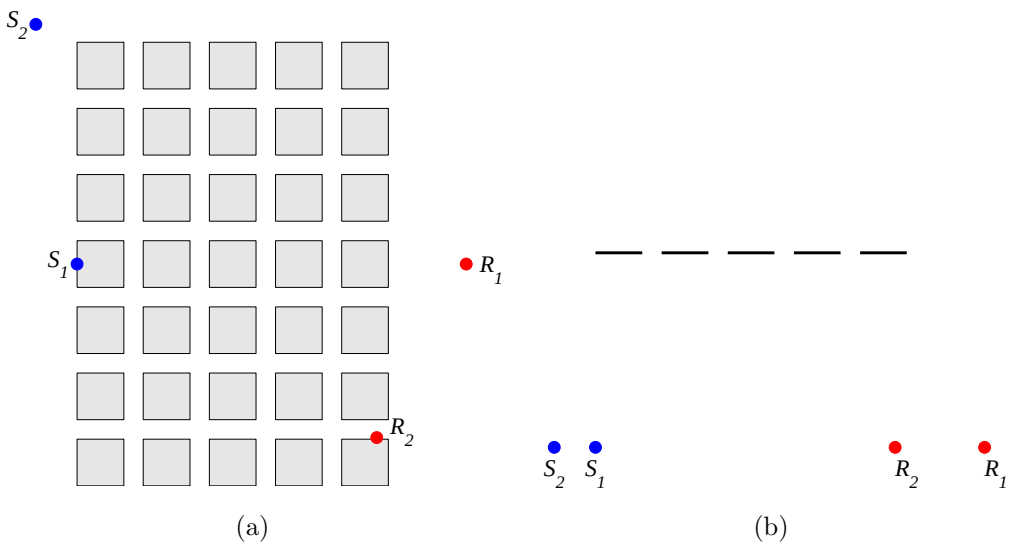

Figure 5.6: Panel-array geometry used to evaluate the hybrid edge-subdivision metthod, shown in plan (a) and section (b) with the source and receiver locations. See the text for further details.

rectangular panels described in [263], similar to one that might be deployed over the stage in a concert hall or other performance space. The array comprises 35 infinitely thin, 1.2 m by 1.2 m panels in a 5-by-7 grid with an inter-panel spacing of 0.5 m. 140 diffracting edges (4 for each panel) were evaluated for each calculation with the array positioned 5 m above two source/receiver pairs. The array and the source and receiver positions are shown in Figure 5.6. All calculations included first-order diffraction only; neither of the source/receiver pairs engendered a specular reflection from the array, and the direct sound and higher diffraction orders were omitted. Due to the absence of GA components, our testing scenarios are conservative in the sense that they over-emphasize the need for accurate diffraction modeling, but are representative of more general test cases in which the sound field is dominated by diffraction.

All computation times are averages from 100 trials, and represent the time to compute all 140 diffraction IRs for the total panel-array response. For each of the two source/receiver pairs, the impulse response generated with sample-aligned segments and 5-point integration for all samples was used as the baseline for all speed and accuracy evaluations. Such calculations previously have been shown to agree quite well with measured data [161, 164], so no comparisons to measured data are included here.

For a conservative approximation of the audibility of the errors in the diffraction IRs, we calculated the diffraction magnitude spectra, smoothed them with 1/10-octave filters, and compared them with the smoothed spectrum of the corresponding baseline case. Differences of less than 1 dB between 20 Hz and 20 kHz were assumed to be inaudible and thus acceptable for perceptual accuracy. Even though all diffracting edges were 1.2 m long, the individual impulse responses within the total response from the panel array ranged in size from 16 to 393 samples for the first source/receiver pair, and from 14 to 441 samples for the second source/receiver pair.

Using the hybrid method, we tested 180 combinations of the calculation parameters with each of the two source/receiver pairs. These combinations included: variations in the size of the alignment zone from 1 to 10 samples; three sizes of evenly-sized segments, specified as maximum sample spans of 40, 100, and 300 samples; and the three integration techniques used independently on the alignment zone and the evenly-sized segments. Only combinations for which the alignment-zone integration technique was equal to, or more accurate than, that for the evenly sized segments were used. For example, when 3-point integration was used for the alignment zone, only 3-point and 1-point integration were tested for the evenly sized segments.

Overall results from the 360 hybrid-subdivision tests are shown in Figure 5.7, where the maximum error in the 1/10th-octave smoothed spectra (below 20 kHz) for the panel-array response is plotted against the total processing time. The trend of reduced error with increased processing time is clear, and the effects of the various parameters are generally as expected. For example: all results with a maximum error greater than 4 dB were generated using the largest even-segment size and a single-sample alignment zone; all results with a maximum error less than .09 dB were generated using the smallest segment size and an alignment zone of at least 6 samples; all but one of the results with a processing time less than 4 ms used 1-point integration with 100-sample or 300-sample even segments. Table 5.1 contains the parameters that resulted in the five fastest processing times with a maximum error of less than 1 dB in the smoothed spectrum for each of the two source/receiver pairs. While there is not a single combination of parameters that yields the "best" result for both source/receiver pairs, the use of a small alignment zone ($N \approx 4$ samples) to compute the onset of the diffraction IRs allows for the use of simplified numerical integration and moderately large, evenly sized segments and thus rapid calculations

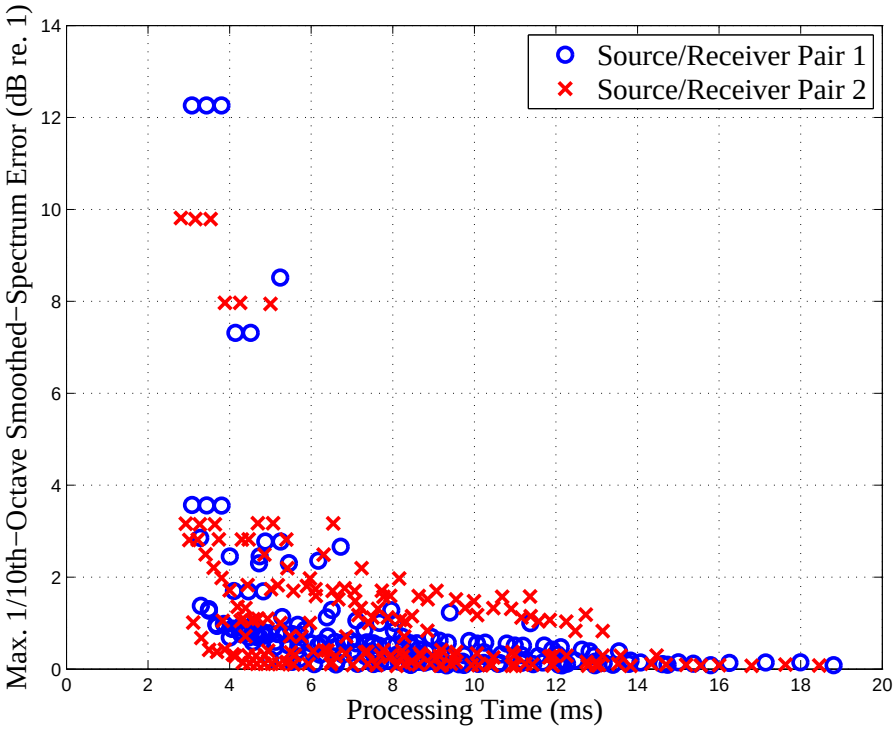

Figure 5.7: Maximum error in the 1/10th-octave smoothed spectra below 20 kHz for various alignment-zone sizes (1 to 10 samples), segment sizes (40, 100, or 300 samples), and integration techniques (1-point, 3-point, or 5-point) using the hybrid method.

with low error. Using the first entry for each source/receiver pair in Table 5.1, the processing time for S_1 and R_1 was reduced by a factor of 46.6 (from 171 ms to 3.67 ms) and that for S_2 and R_2 by a factor of 41.7 (from 138 ms to 3.31).

Results from an example calculation can be seen in Figures 5.8 and 5.9(a). The IRs and corresponding magnitude spectra shown were generated for S_1 and R_1 using the baseline parameter configuration (all sample-aligned subdivision with 5-point integration), and with hybrid subdivision using the following parameters (see Table 5.1 Line 1): an alignment zone of 4 samples, a maximum sample span for the even segments of 100 samples, and 1-point integration for the entire edge. Figure 5.8 shows the total impulse response calculated for the panel array, and the inset contains a zoomed-in view of a portion of the IR where the hybrid method's piecewise linear approximation of the IR can be seen. Figure 5.9(a) contains the smoothed magnitude spectra of the two IRs. The error (difference between the two spectra) is plotted in Figure 5.9(b), as is the error for an example calculation using S_2 and R_2 with the parameters given in Line 7 of Table 5.1. The maximum error

S/R Pair	Zone Size (Samples)	Zone Integ.	Segment Size (Samples)	Segment Integ.	Proc. Time (ms)	Max. Error (dB)
1	4	1-point	100	1-point	3.67	.97
1	4	1-point	300	1-point	3.69	.94
1	5	1-point	100	1-point	3.86	.98
1	5	1-point	300	1-point	3.88	.96
1	2	3-point	100	1-point	4.01	.69
1	all	5-point	N/A	N/A	171.25	0
2	3	1-point	100	1-point	3.31	.68
2	4	1-point	100	1-point	3.50	.41
2	5	1-point	100	1-point	3.69	.38
2	6	1-point	100	1-point	3.88	.43
2	7	1-point	100	1-point	4.08	.32
2	all	5-point	N/A	N/A	137.51	0

Table 5.1: Parameters resulting in the 5 fastest processing times for each S/R pair with maximum error in the smoothed spectrum less than 1 dB. Data for the baseline calculations also are included for comparison as the last entry for each S/R pair.

below 20 kHz occurs at approximately 325 Hz for S_1 and R_1 and at 13.05 kHz for S_2 and R_2.

5.5 Summary

In this chapter we have described three edge-subdivision strategies for generating discrete-time diffraction impulse responses: one based on sample-aligned edge segments, one on evenly sized edge segments, and a hybrid of the two. The first is the most accurate but suffers from high computation time. The second provides a significant reduction in computation time, but is problematic numerically when segments span the apex point on an edge due to the singular behavior of the diffraction integrand at that point. The third attempts to provide a compromise between the first two, allowing for fast computations with low error and straightforward numerical evaluation. Using the hybrid method, each edge in a 3D model initially is subdivided into evenly sized segments. Given the source and receiver positions, the section of each edge that contributes to the first few samples of the diffraction IR is subdivided into sample-aligned segments. Even segments overlapping this alignment zone are truncated at the edges of the zone, and those completely within

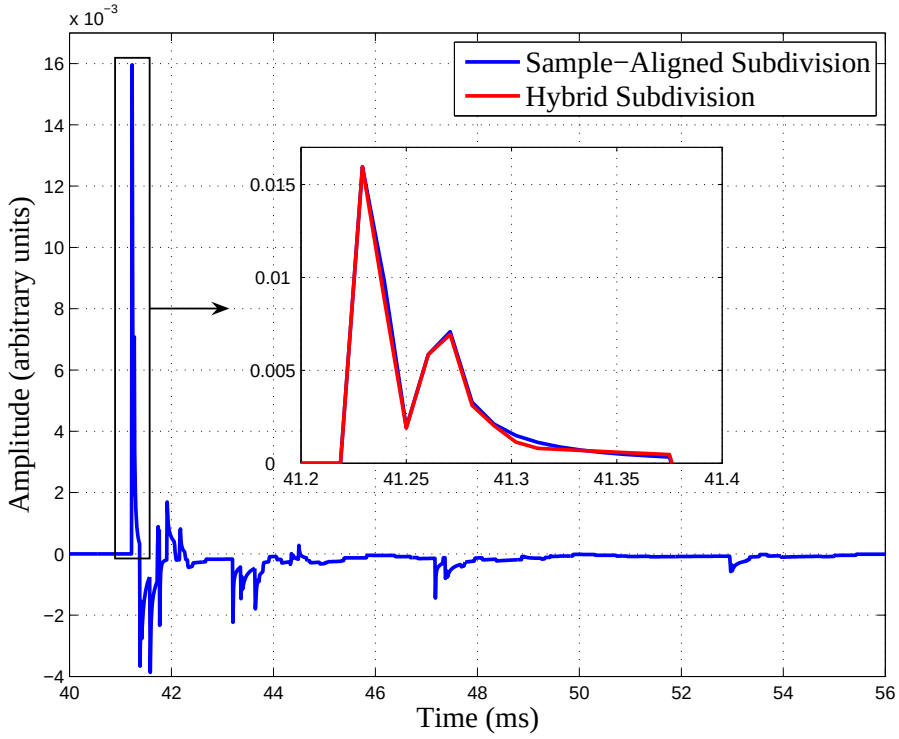

Figure 5.8: Impulse responses for source position S_1 and receiver position R_1. The blue IR (shown in the main figure and the inset) is the baseline calculation using sample-aligned segments and 5-point integration, and the red IR (inset only) is an approximation using hybrid subdivision with the parameters specified in Line 1 of Table 5.1.

the alignment zone are discarded. The diffraction integral is then evaluated for all remaining segments along the edge. Because the sample-aligned subdivision provides numerically accurate results with a high computational cost, we restrict its use to the early portion of the IR that contains a significant percentage of the total diffracted energy and thus must be calculated accurately for a perceptually convincing simulation. It also allows for the onset sample, which is subject to a singularity for receivers near reflection and shadow boundaries, to be handled with the analytical approximations described in Section 4.3. However, a user is free to choose the size of the alignment zone, as well as the size of the evenly sized segments and the integration technique(s) used to evaluate the two types of segments, to optimize the speed-accuracy trade-off for each modeling scenario.

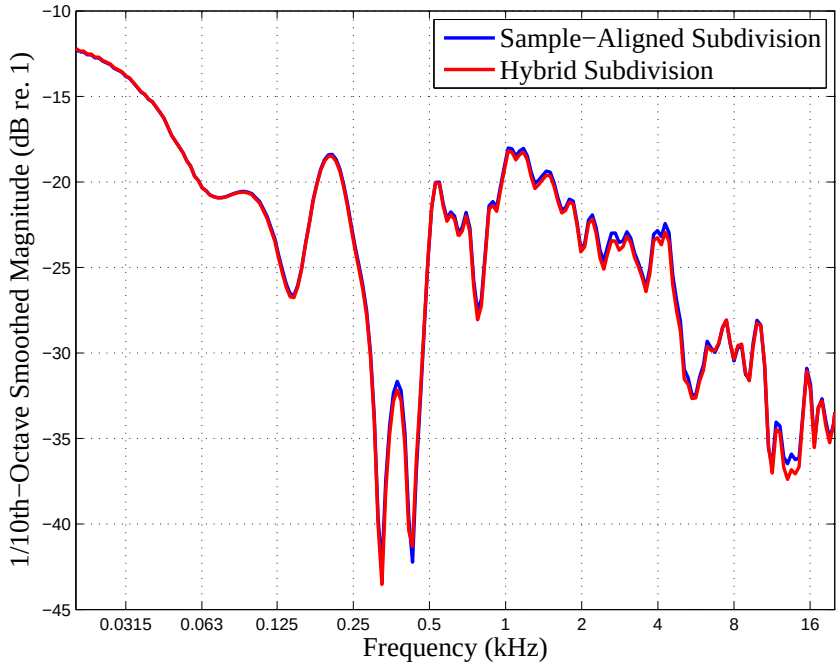

(a)

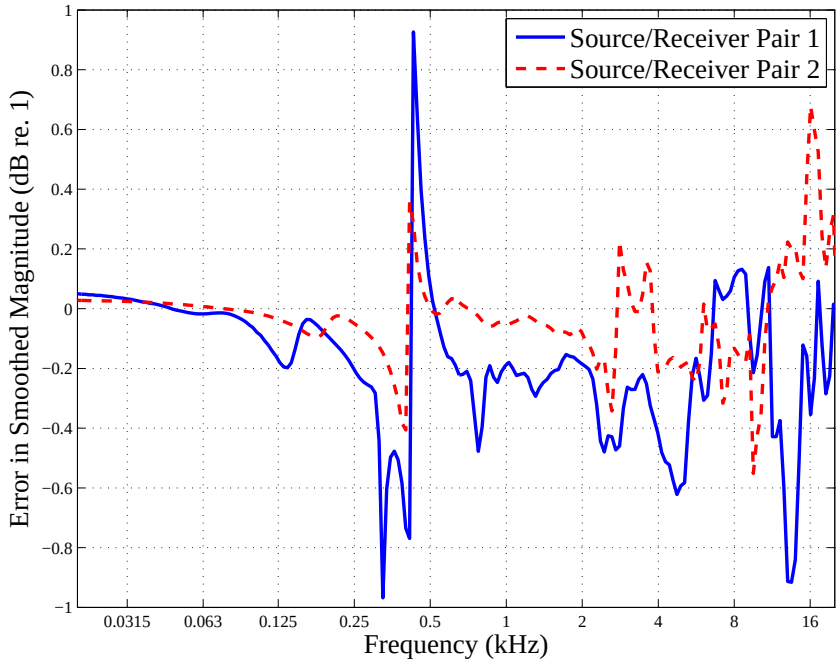

(b)

Figure 5.9: (a)1/10th-octave smoothed magnitude spectra for the impulse responses in Figure 5.8. (b) Error in the smoothed-spectra for S_1 and R_1 and the parameters in Line 1 of Table 5.1 (solid blue line) and for S_2 and R_2 and the parameters in Line 7 of Table 5.1 (dashed red line).

Chapter 6

Diffraction Culling in Virtual-Acoustic Simulations

6.1 Introduction

The addition of diffraction to GA simulations provides an increase in physical and perceptual realism by compensating for the effect of surface size on the strength and directivity of a reflection, allowing for propagation around obstacles and into shadow zones, and by maintaining continuity of the sound field across zone boundaries. These gains, however, come with a high computational cost. As shown in Figure 6.1, including diffracted paths in a simulation drastically increases the total number of propagation paths from a source to a receiver that must be considered, and each diffraction impulse response (IR) can be slow to compute. These issues are particularly important for simulations with a moving source or receiver because the impulse responses must be updated at interactive rates.[1]

However, for a given modeling scenario, the contribution of each diffracted path to the overall impulse response can vary significantly. For example, in some of the concert-hall simulations described in Section 6.2.1, the peak amplitudes of the diffraction components vary over nearly 10 decades (200 dB). This suggests that

[1]The exact update rate required for artifact-free interactive acoustic simulations is a matter of debate. Various authors claim to generate interactive or real-time simulations with update rates varying from 4 to 30 Hz (*e.g.* see [37, 85, 229, 271]) while recommendations of 60 Hz [225, 288] and 100 Hz [84] have also been given.

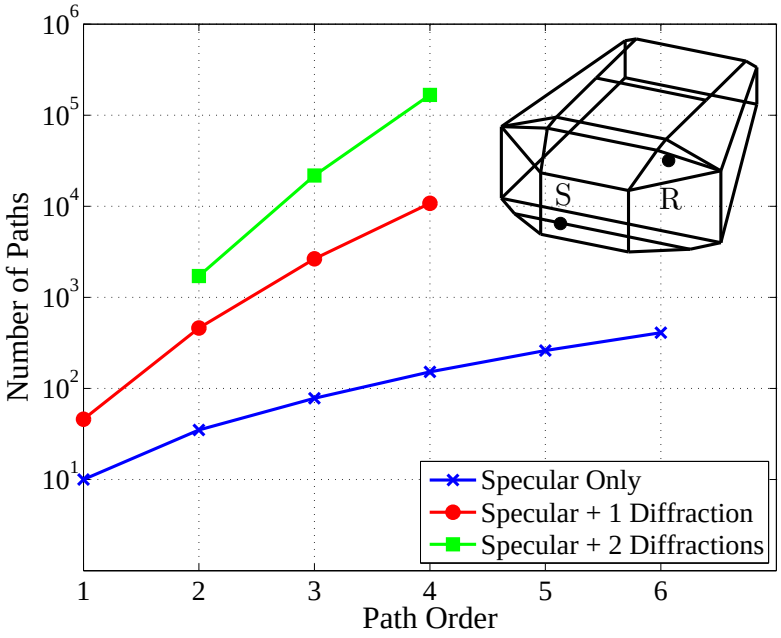

Figure 6.1: Growth in the number of propagation paths with the addition of diffraction for the model, source, and receiver in the inset.

certain diffracted paths for which the contribution is small can be ignored, or culled, potentially resulting in a reduction in processing time with little detrimental effect on the accuracy of the simulation.

Culling insignificant or low-priority diffraction components in virtual-acoustic simulations has been studied previously. In particular, interactive acoustic-modeling systems that include diffraction typically involve some sort of culling procedure for diffracted paths to allow for sufficiently high update rates. For example, Tsingos *et al.* [271] describe an optional culling scheme within a beam-tracing system in which diffracted paths are only considered in the shadow region of a diffracting wedge; all other diffracted paths are culled. Chandak *et al.* [37] employ the same approach in their frustum-tracing system. Antonacci *et al.* [7] have also developed a beam-tracing system for 2D and 2.5D environments with the option of including only a subset of the possible diffracted paths. To enable interactive updates for a moving source or receiver, they ignore diffraction from wedges with an open (exterior) angle $\theta_W \leq \pi$, noting that in such cases the direct sound should be present and thus will dominate the local sound field. For wedges with $\theta_W > \pi$, diffraction is ignored unless the receiver is in the shadow zone. Culling has also been applied to virtual-acoustic simulations in a more general form by Funkhouser *et al.* [84] and Min and

Funkhouser [180], who use a priority queue and various priority functions to control a beam-tracing system. Beams are prioritized based on their expected likelihood of leading to psychoacoustically important propagation paths (comprising reflections and/or diffractions and/or transmissions) and processed in "best first" order up to a termination criterion, thus culling the insignificant sound-field components left unprocessed in the priority queue.

Culling has also been considered in other simulation applications. For rendering images of 3D models, Aveneau *et al.* [11] suggest a method that limits diffraction calculations to wedges that intersect the n^{th} Fresnel ellipsoid defined by the source and receiver. Yagel and Meeker [292] describe a priority-driven ray tracer (similar to the beam-tracing system mentioned above) that rank orders rays to be traced based on their expected contribution to the image, potentially culling paths with insignificant intensity contributions. In the context of modal sound synthesis, van den Doel *et al.* [277] and Raghuvanshi and Lin [212] describe the culling of inaudible modes to accelerate audio rendering for interactive simulations. Tsingos *et al.* [272] cull inaudible sound sources using binaural loudness masking to allow for real-time audio simulations in complex environments with large numbers of sources.

In this chapter we first analyze the effects of diffraction culling though a precomputed, amplitude-based ranking scheme using simulated IRs from two simple concert-hall models. For each IR corresponding to a specific source and receiver, diffracted components are ranked by their maximum amplitude, and the spectral error caused by culling various percentages of the low-amplitude IRs is calculated and evaluated. In addition, we have carried out subjective tests with auralizations based on the culled and unculled IRs from one of the halls, and we show that a significant percentage of diffracted paths can be ignored with limited perceptual consequences (with some dependence on the input signal convolved with the IRs). This approach facilitates an exact importance ranking of the diffracted components and is thus an effective tool to help understand the effects of culling, but it is unrealistic for general use in simulation systems because all diffraction IRs must be calculated prior to the ranking and subsequent pruning.

We then present a simple procedure for culling insignificant diffraction components during a virtual-acoustic simulation that approximates the performance of the precomputed ranking approach. For each diffracted path, this method considers the receiver's angular distance to the nearest reflection or shadow boundary as well as

the shortest path from the source to the receiver through the line that contains the diffracting edge. This combination of parameters can be an effective predictor of the diffraction amplitude, and can be evaluated before the actual diffraction IR is calculated. Results from numerical analysis and subjective tests confirm that this method approximates the rank-based amplitude culling well, and in certain circumstances allows for simulations that cannot be distinguished reliably from those made with unculled impulse responses.

The remainder of this chapter is organized as follows. Section 6.2 contains an overview of our simulation methodology. Sections 6.3 and 6.4 describe rank-based culling and our zone-boundary culling method, respectively, and contain numerical analyses of results from two simple concert-hall models, and subjective analyses of results from one model. Further discussion of our method is provided in Section 6.5 and Section 6.6 contains some concluding remarks. This chapter was published in modified form in [31].

6.2 Methodology

The culling approach described in Section 6.4 relies on the singular behavior of Eq. 3.8 (the β_i functions in the BTM integrand) to identify high-amplitude diffraction IRs. Recall that the denominator of this expression approaches zero for the onset sample of the diffraction IR as a receiver approaches a zone boundary if the apex point is included in the edge. The resulting high-amplitude onset can be used as a measure of importance for a diffraction IR, and can be predicted by the angular distance to the nearest zone boundary and the apex-point status. Since the singular behavior is physically based and occurs in other diffraction expressions, our culling method is not restricted to the BTM line-integral formulation that is used in our implementation.

6.2.1 Simulation Scenarios

To study the effects of diffraction culling, we used the Edge Diffraction Toolbox for Matlab® [254] with custom modifications to compute the impulse responses in two

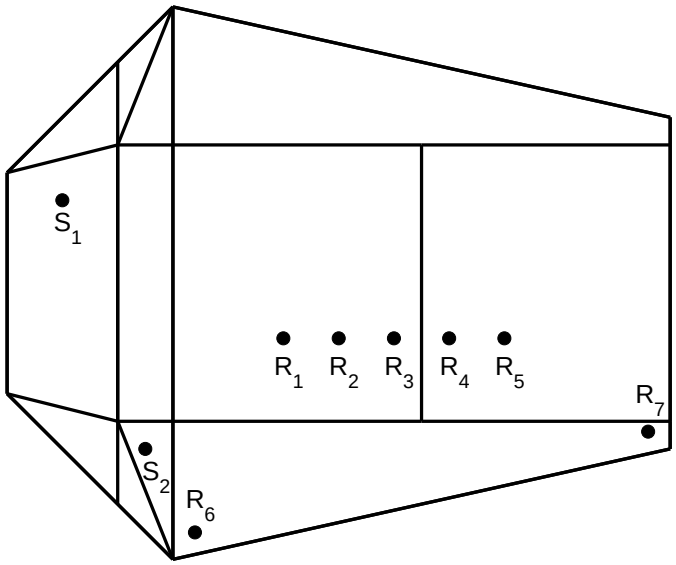

(a)

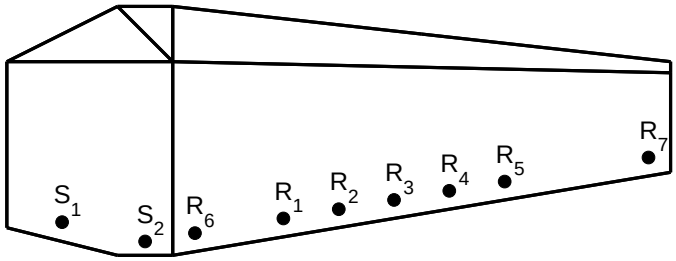

(b)

Figure 6.2: Hall 1: A simple concert-hall model from [168] used in our tests. See also the inset in Figure 6.1.

simple concert-hall models from [168], [2] with two source positions and seven receiver positions in each. As shown in Figure 6.2, the geometry of the first hall (hereafter Hall 1) is convex, and the two sources on the stage have clear lines of sight to all receivers. As shown in Figure 6.3, the second hall (Hall 2) is of similar shape and size with the addition of an orchestra pit[3] and a balustrade/rail between the pit and the audience seating area. The two sources, both in the pit, are occluded from all receivers in this scenario.

[2]The exact geometries of the halls used in our studies differ slightly from those in [168] because various vertex locations needed to be modified to close gaps and enforce planarity of surfaces.

[3]The pit depth has been changed from the original 5.5 m to 3.0 m by raising the pit floor. This was done to bring the dimension into agreement with Beranek [15] and Barron [13] who give the range for a typical pit depth as 2.5 to 3.5 m.

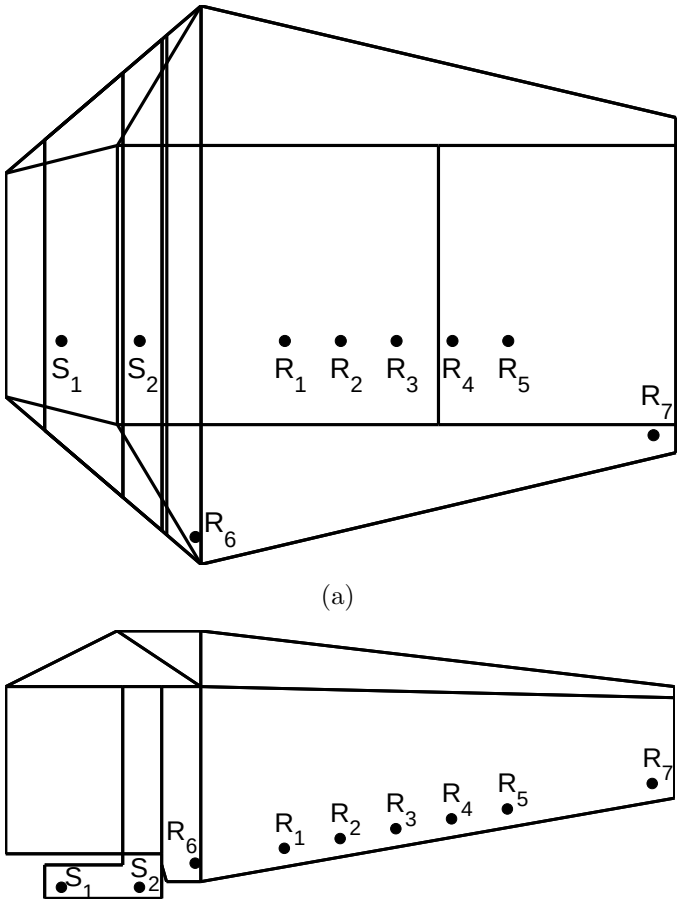

Figure 6.3: Hall 2: A concert hall-model from [168] with an orchestra pit used in our tests. Note that both sources are occluded from all receivers.

The simulated IRs included components up to fourth order with at most one diffraction per path. Thus, using the symbols S for source, R for receiver, F for reflection, and D for diffraction, a GA component could be of the form $S \rightarrow F^* \rightarrow R$ where F^* represents any number of reflections from zero to four, and a diffraction component could be the result of a path of the form $S \rightarrow F^* \rightarrow D \rightarrow F^* \rightarrow R$ with the sum of the number of reflections and the single diffraction no greater than four. All IRs were computed at 96 kHz. In order to isolate the effect of culling on the early part of the simulated sound fields, a reverberant tail was not added to the computed IRs. This also prevented any audible culling artifacts from being masked by reverberation. The lack of a reverberant tail is mitigated somewhat by the use of a path-order cutoff, which results in IRs that taper off more gradually than those with a time cutoff.

The halls were modeled with all rigid surfaces due to the rigid-wedge restriction of the BTM diffraction formulation. While this is not a physically realistic condition, various studies (*e.g.* see [161]) have shown good agreement between BTM diffraction and hard architectural materials that typically occur in concert halls.

6.3 Culling by Amplitude Rank

Diffraction IRs typically have an impulsive onset followed by a rapidly decaying tail. The high-frequency response is governed primarily by the onset, while the low-frequency response is affected by both the onset and the length and total energy of the entire IR. Thus, the onset plays a critical role in the broadband diffracted spectrum and its perceptual characteristics. We therefore used the maximum amplitude of each diffraction IR, typically the onset amplitude, to rank the diffraction components in each computed room IR from most to least important (highest to lowest maximum amplitude). A rank of '1' indicates the highest amplitude, and thus low rank numbers correspond to the most significant diffraction IRs.

We also considered ranking diffraction components based on their total energy. Figure 6.4 shows the relationship between rank by maximum amplitude (abscissa) and the rank by total energy (ordinate) for the 10628 diffraction components within the IR corresponding to source S_1 and receiver R_3 in Hall 1. While the rank ordering is not identical for the two, our numerical and subjective tests focus on a small percentage of the highest amplitude IRs, *i.e.* those with low ranks, where the correlation is quite good (Fig. 6.4 inset), suggesting that either ranking is suitable for our purpose.

The diffraction components in room impulse responses can cover a wide range of amplitudes, and many of them are significantly smaller than the GA components. For example, one IR addressed further in Section 6.4 and Figure 6.10 contains diffraction components with peaks that vary over a 200 dB range. Because such a wide range is consistent throughout our source/receiver combinations, we used the amplitude rankings to recompute the room IRs described in Section 6.2.1 with only the largest 32 percent, 8 percent, 2 percent, and 0.5 percent of the diffraction components retained (68 percent, 92 percent, 98 percent, and 99.5 percent culled, respectively). In addition, the 9-percent retained case (91 percent culled) was also

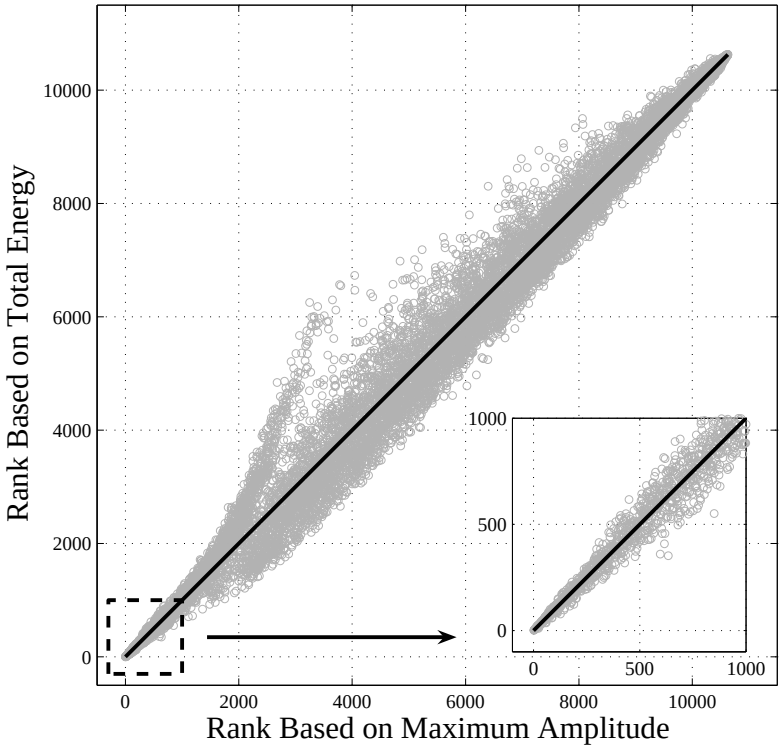

Figure 6.4: Relationship between rank by maximum amplitude and rank by total energy for the 10628 diffraction components in the simulated impulse response from S_1 to R_3. The inset is a zoomed-in view of the 1000 diffraction IRs with lowest ranks (highest amplitude/energy). Our analysis is focused on these low ranks where the correlation is quite good, suggesting that either criterion is suitable for ranking the significance of the diffraction components. The correlation for the other source/receiver pairs is similar.

computed for Hall 2. If the peak amplitude of a diffraction component was not above the percentage threshold (*i.e.* its rank was not sufficiently low), the *entire* diffraction IR (onset and tail) was omitted from the recomputed room IR. For each S/R pair, the spectra of these culling cases were compared with the spectrum of the full IR, *i.e.* the one for which all diffraction components were retained. In addition, listening tests with auralizations based on the culled and full IRs from Hall 1 were conducted to determine the audibility of the errors introduced by the culling. Throughout the remainder of this paper, we refer to these culling cases by the percentage of *retained* diffraction components. For example, the case for which 2 percent were retained and 98 percent were culled is called "the 2-percent culling case."

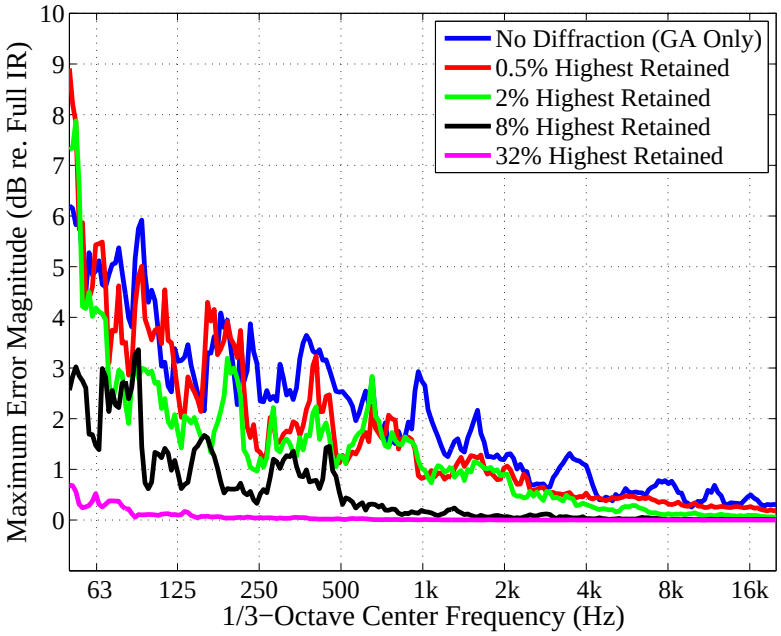

Figure 6.5: Maximum error, taken over all 14 source/receiver pairs, in the smoothed magnitude spectrum for various rank-based culling cases in the Hall 1 model (Figure 6.2). Values in the legend indicate percentages of diffraction components retained based on amplitude ranking from highest to lowest.

6.3.1 Hall 1: Visible Sources on Stage

Initial test results were generated for Hall 1 with two sources on the stage and seven receivers in the audience-seating area as shown in Figure 6.2. The open geometry and clear lines of sight from both sources to all receivers allowed for significant energy from GA and diffracted components in all IRs. Over all 14 source/receiver combinations, the full IRs (with maximum 4th-order components) contained an average of 123 GA components (min.: 59, max.: 247) and 10455 diffracted components (min.: 8723, max.: 11252).

6.3.1.1 Numerical Analysis

Figure 6.5 shows the maximum error, taken over all 14 S/R combinations, for the 1/3-octave smoothed spectra of the four culling-by-rank cases. The error for the GA-only case (*i.e.*, IRs with no diffraction) is also shown for comparison. It can be seen that the error is quite low at high frequencies for all culling cases, generally 1 dB or less above 1 kHz. This is not surprising for two reasons: much of the high-

frequency energy is contained within the GA components and is thus unaffected by the culling; and the highest amplitude diffraction onsets, which contain much of the high-frequency diffracted energy as described previously, are retained. The error below 1 kHz is neither smooth nor monotonic, but shows a general trend of increasing as frequency decreases, with some significant peaks and valleys caused by interference effects between the diffracted and GA components. The growth in error with decreasing frequency is due to the low-pass nature of the individual diffraction components. At very low frequencies, the diffracted contribution can be stronger than the GA contribution since the GA components have, on average, a flat frequency response. This low-pass behavior summed over the thousands of small, culled IRs is significant. Taking into consideration the frequency weighting of the human auditory system, the data in Figure 6.5 suggest that the threshold of audibility for the culling error will occur at or below the 8-percent case, thus allowing at least 92 percent of the diffraction components to be culled without detrimental perceptual consequences.

An interesting and unexpected characteristic of the error spectra plotted in Figure 6.5 is the low-frequency error near 50 Hz for the 0.5 percent and 2.0 percent culling cases, which is *larger* than the corresponding error for the GA-only case. This is due to the IR computed for source S_1 and receiver R_6. In this case, many of the largest diffraction IRs have a negative polarity, and arrive at the receiver simultaneously with GA components. The resulting destructive interference reduces the total energy in the IR from that of the GA-only case, and thus increases the low-frequency error. It is not until the largest 8 percent of the diffraction IRs are included that this effect is mitigated.

6.3.1.2 Subjective Analysis

To evaluate the perceptual consequences of the rank-based culling, we conducted listening tests using auralizations created with the simulated IRs. Three anechoic samples were used to create the auralizations: a five-second pink-noise burst, and approximately six-second excerpts from Handel's Water Music and Bruckner's Symphony No. 4 [64]. Magnitude spectra for the anechoic samples are shown in Figure 6.6. 17 subjects participated for the pink-noise and Handel auralizations, and each session comprised 48 individual tests covering the two source materials, two source

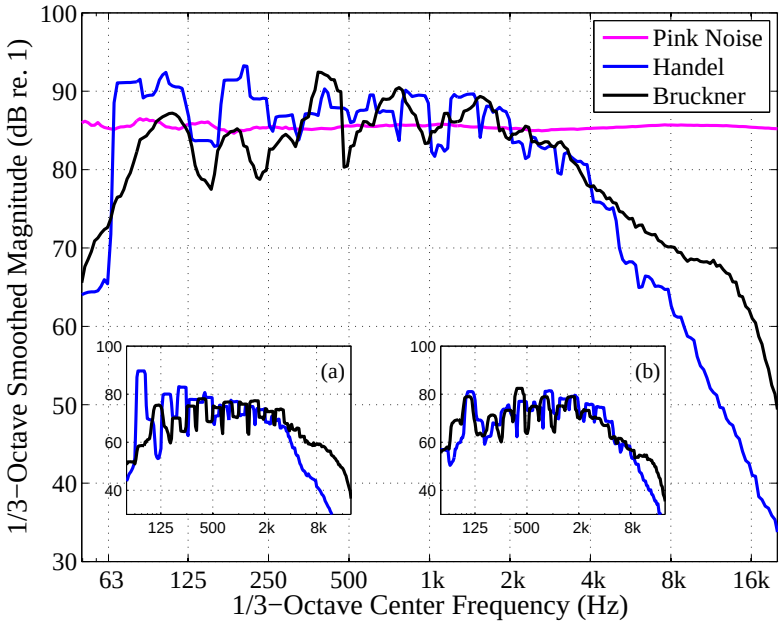

Figure 6.6: One-third octave smoothed magnitude spectra for the source materials used in the auralizations: pink noise, and excerpts from Handel's Water Music and Bruckner's Symphony No. 4. The main figure shows the overall spectra for the full-length signals: 5 seconds for the pink noise, 6 seconds for the Handel, and 6.5 seconds for the Bruckner. To indicate the non-stationary nature of the musical samples, Inset (a) shows the spectra for the first second of the excerpts, and Inset (b) the spectra for the final second.

positions, three receiver positions, and four levels of culling. The four culling levels included: no diffraction (GA components only), culling all but the largest 0.5 percent of the diffraction IRs; culling all but the largest 2.0 percent; and culling all but the largest 8.0 percent. The 32-percent case was omitted from the listening tests due to the extremely low spectral error. To limit the length of each test session and avoid listener fatigue, only six of the fourteen possible source/receiver combinations shown in Figure 6.2 were used. The six were chosen to represent a variety of error spectra. 9 subjects, all from among the original 17, participated in the Bruckner-based tests that included the same four culling levels applied to 4 of the 6 original source/receiver pairs.

For each test, subjects were presented with three sound samples in the typical ABX paradigm. In each case, either Sample A or B was an auralized signal using an impulse response with the full compliment of diffraction components, while the other sample was created with a culled IR. The test was designed to determine the threshold of audibility for the rank-based culling, *i.e.* the smallest percentage of diffraction components (from among the tested values) necessary to

make the auralizations with culled IRs indistinguishable from those made with the full-diffraction IRs.

The auralizations were presented diotically over Sennheiser model HD 600 headphones (powered by a PreSonus HP4 headphone amplifier that obtained the audio signal from a desktop-computer soundcard) in a sound-isolated listening room. Because the simulated IRs were non-directional, no attempt was made to add spatial information to the auralizations, *e.g.* through the use of head-related transfer functions. Each test session began with two training tests, one each with convolved music and pink noise. During the training the subject was encouraged to adjust the sound level to a comfortable range (within appropriate limits) that was then left constant for the remainder of the session. For each ABX comparison, the subject was allowed to play the samples in any order, and each as many times as desired. The subjects were between 20 and 36 years of age. Fourteen of the subjects were self described as "experienced in critical listening," and one reported hearing loss as, "a slight mid-frequency dip in the left ear."

Results from the listening tests are presented in Figure 6.7. The first group of bars represents the subjects' performance when comparing the GA-only auralizations to the full-diffraction auralizations. Each of the three remaining groups of bars indicates the performance of the subjects for one of the culling cases. The data cover all tested source and receiver pairs, and are shown for each source type individually because the subjects' performance varies among them.

For the pink-noise auralizations, the successful differentiation rate of approximately 83 percent for the GA-only condition is slightly higher than, but generally in agreement with, results presented by Torres *et al.* who studied the audibility of diffraction in a virtual model of a stage house [265]. As expected, the subjects' pink-noise performance degrades with increasing retention of diffraction IRs and is near chance for the 8-percent case, indicating that they were unable to discriminate reliably between the culled and unculled examples for this source material and culling condition.

The results for the Handel auralizations are less intuitive. The reduced discrimination performance for the GA-only condition (approximately 66 percent) is somewhat expected, given the narrower bandwidth and the non-stationary and generally more complex nature of the source spectrum. However, the *increasing*

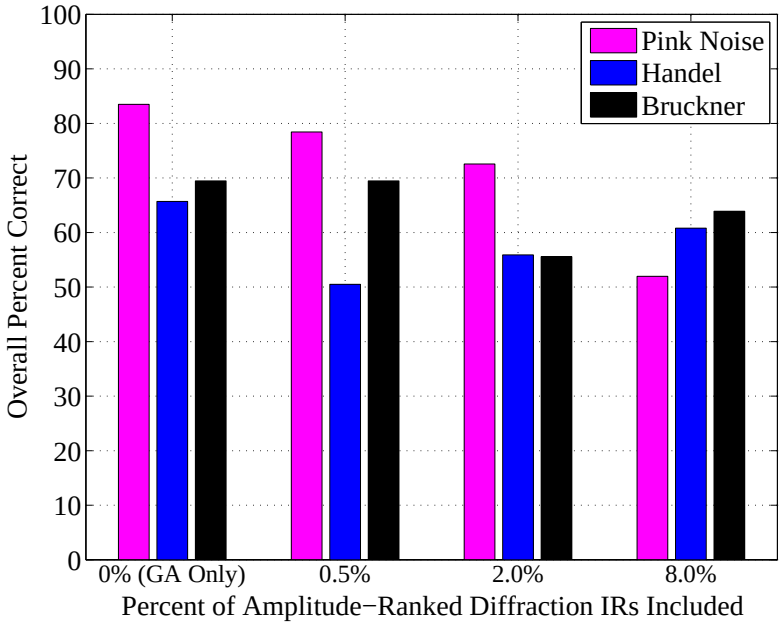

Figure 6.7: Results from our listening tests for rank-based culling in the Hall 1 model. For the pink-noise and Handel auralizations, responses have been averaged over 17 subjects and 6 source/receiver pairs. For the Bruckner auralizations, responses have been averaged over 9 subjects and 4 source/receiver pairs. See Section 6.3.1.2 for details.

discrimination performance with increasing diffraction content is the opposite of the expected trend. To a certain extent this can be explained by evaluating the spectral error for the individual source/receiver pairs. For four of the six pairs, the error shows a fairly consistent and expected decreasing trend as the diffraction content is increased. When the listening-test results for only these four pairs are examined as a group, the subjects' performance was approximately 74 percent correct for the GA-only case, and 59 percent for all three culling conditions. For the other two S/R pairs, there is considerable overlap in the spectral-error curves among the culling conditions, making discrimination more difficult and thus skewing the overall subjective results. The effect of these two S/R pairs is also evident, but less so, in the pink-noise results, which show a slightly more robust discrimination trend when the two are omitted from the analysis.

The Bruckner-based tests were conducted in a separate, later session to evaluate the effect of diffraction culling on a second, realistic (musical) source material.[4] Only the four S/R pairs mentioned above with the expected error trends were included.

[4]As a control, tests based on pink noise and Handel auralizations were repeated at this stage as well. The results were comparable to those from the original tests.

As can be seen in Figure 6.7, the discrimination performance was identical for the GA-only and 0.5-percent culling cases at 69 percent, decreased to 56 percent for the 2-percent case, then increased to 64 percent for the 8 percent culling case. The small number of subjects makes it somewhat difficult to compare these data directly to the pink-noise and Handel results, and to draw definitive conclusions about the relative audibility of the different culling conditions (*e.g.* the 2% and 8% results differ by only 3 correct responses out of 36) for the Bruckner auralizations. However, it is clear that for certain source materials the complete lack of diffraction components leads to perceptible differences from the full-IR simulations, and only a small fraction is needed to make discrimination between culled and unculled IRs unreliable.

Test results for each individual source/receiver pair, source type, and culling case are provided in Table 6.1. Using a significance level of 0.05, 12 correct responses out of 17 ($p = 0.0472$, binomial distribution) or 8 correct out of 9 ($p = 0.0176$) are necessary to establish that the auralization using the culled IR can be distinguished reliably from the auralization made with the full-diffraction IR. This was achieved for 11 of the 16 GA-only examples, 7 of the 16 half-percent culling examples, 5 of the 16 two-percent culling examples, and only 1 of the 16 eight-percent culling examples, again indicating that retaining only 8 percent of the diffraction components is sufficient to make the auralizations indistinguishable from those made using IRs with all diffraction components included.

6.3.2 Hall 2: Occluded Sources in the Pit

Impulse responses were also generated for the model in Figure 6.3 with two sources in the pit, seven receivers in the audience-seating area, and maximum 4th-order components. The line of sight was occluded from both sources to all receivers. The numbers of GA and diffracted components in the Hall 2 IRs displayed a bimodal characteristic: for source S_1, the full IRs contained an average of 15 GA components (min.: 4, max.: 28) and 5219 diffracted components (min.: 4839, max.: 5555); for source S_2, the full IRs contained an average of 56 GA components (min.: 7, max.: 69) and 9195 diffracted components (min.: 8762, max.: 9773).

For direct comparison to the results in Section 6.3.1.1, Figure 6.8 shows the maximum error, taken over all 14 S/R pairs in Hall 2, for the 1/3-octave smoothed

Table 6.1: Correct/incorrect responses for the subjective tests of rank-based culling. Bold pairs indicate those for which the 0.05 significance level is met or surpassed, suggesting reliable discrimination between the auralizations with culled and unculled impulse responses. For the Handel and pink-noise auralizations, each entry represents the responses of 17 test subjects. However, for the two entries marked with an asterisk (Handel, S_2, R_7: GA only and 0.5%), the sum of correct and incorrect responses is 16 rather than 17. This is due to an error in the subjective-testing software that led to these two cases being omitted from a session. The error was corrected when it was discovered after reviewing the data from the first subject. For the Bruckner auralizations, each entry represents the responses of 9 test subjects.

	Pink Noise				Handel				Bruckner			
	GA Only	0.5%	2.0%	8.0%	GA Only	0.5%	2.0%	8.0%	GA Only	0.5%	2.0%	8.0%
S_1, R_4	**12/5**	**12/5**	**15/2**	7/10	9/8	6/11	4/13	10/7	N/A	N/A	N/A	N/A
S_1, R_5	**12/5**	**13/4**	**14/3**	7/10	8/9	5/12	**13/4**	**12/5**	N/A	N/A	N/A	N/A
S_1, R_7	**15/2**	**14/3**	**13/4**	10/7	**12/5**	9/8	9/8	8/9	3/6	4/5	3/6	6/3
S_2, R_2	**17/0**	**12/5**	10/7	11/6	**12/5**	11/6	9/8	11/6	**9/0**	6/3	5/4	6/3
S_2, R_3	**15/2**	**15/2**	11/6	8/9	**15/2**	11/6	9/8	10/7	**8/1**	**8/1**	7/2	6/3
S_2, R_7	**14/3**	**14/3**	11/6	10/7	11/5*	9/7*	**13/4**	11/6	5/4	7/2	5/4	5/4

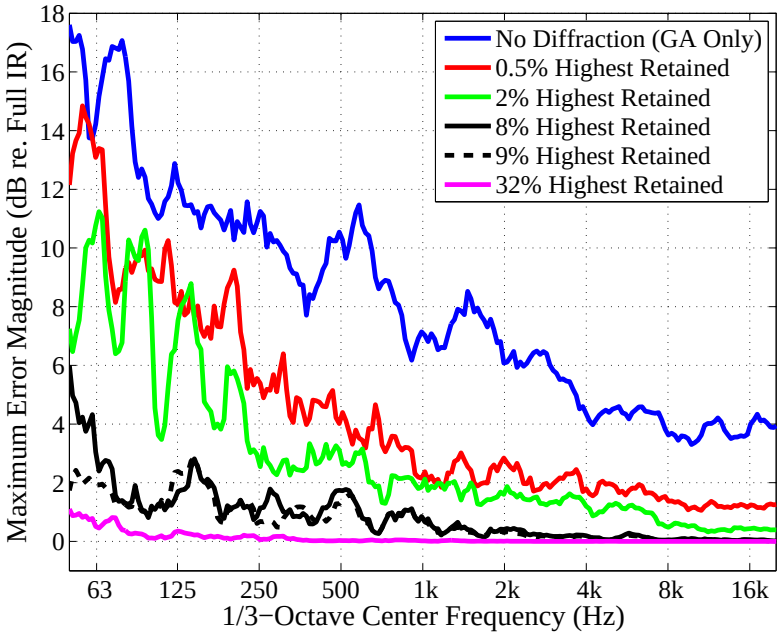

Figure 6.8: Maximum error, taken over all 14 source/receiver pairs, in the smoothed magnitude spectrum for various rank-based culling cases from the Hall 2 model (Figure 6.3). Values in the legend indicate percentages of diffraction components retained based on amplitude ranking from highest to lowest. Compare to Figure 6.5, but note the change in the y-axis limits.

spectra of the same four culling-by-rank cases. The error for the GA-only case is significantly higher than that in Figure 6.5 due to the reduced GA content of the IRs and thus the greater importance of the diffracted components. In particular, the S_1/R_6 or S_2/R_6 pair produced the highest GA-only error in nearly every band across the spectrum, as the associated IRs contain only 4 and 7 GA components, respectively. The 0.5-percent culling case results in a large improvement over the GA-only case, with error reductions between approximately 2 and 8 dB across the audible spectrum (*cf.* the 1 - 2 dB correction in Figure 6.5), but the error remains quite high. The 2-percent case also results in high error, particularly in the bands below 250 Hz. The error for the 8-percent case is comparable to that for the open model, deviating significantly only below the 63-Hz band. This low-frequency error is associated with the IR for source S_1 and receiver R_7, and is due to interference effects between the diffraction and GA components that are specific to this S/R pair. This error is reduced to an acceptable level when an additional 1 percent of the diffraction components (9 percent total) are included, as shown with the dashed black line. Despite the occluded sources and reduced GA components, a low spectral error similar to that found to be imperceptible in the open model can be achieved

by including fewer than 10 percent of the diffraction components. Subjective tests were not conducted using the IRs from Hall 2, but are discussed briefly in Section 6.5.

6.4 Culling by Proximity to a Zone Boundary

As seen Eqs. 3.8, 3.10, and 3.13, the various BTM expressions, there are numerous parameters that influence the strength of a diffraction IR and could be used to identify significant components to retain. Some are particularly attractive because they depend only on the geometry of the simulation environment and require little additional computational overhead, but they also can be difficult to exploit effectively. For example, the dependence of the diffracted amplitude on the wedge angle θ_W is a function with easily identified zeros (when $\theta_W = \pi/m$ for integer values of m [18, 129]) but complicated behavior in between. Edge length is loosely correlated with the duration of the diffraction IR, but this relationship is heavily dependent on the source and receiver positions. Rather than use such purely geometric parameters, our method indirectly uses the denominator of Eq. 3.8 which can be very small or zero as described in Chapter 4, and the resulting singularity causes the diffraction IR to have a high-amplitude, impulsive onset. In addition, these high-amplitude IRs occur for receivers at or near zone boundaries, and thus play a particularly significant role in maintaining a continuous sound field for a moving source or receiver.

Recall that the singularity in Eq. 3.8 occurs only when $\cosh(\nu\eta) = \cos(\nu\varphi_i) = 1$, a condition that is met for the diffracted path through the apex point for a receiver on a zone boundary associated with a value of $\nu\varphi_i$. The effect of the singularity on the diffraction can be seen in Figure 6.9 for a wedge with $\theta_W = 270°$ and a source at $\theta_S = 45°$. The diffracted field peaks and changes polarity as the receiver approaches and crosses the reflection boundary at $\theta_R = 135°$ and the shadow boundary at $\theta_R = 225°$. When the source and receiver are moved to a z-value beyond the end of the edge and thus the apex point is not included, there is still a polarity change in the diffracted field at the zone boundaries but the peak amplitude is significantly reduced from the apex-included case.

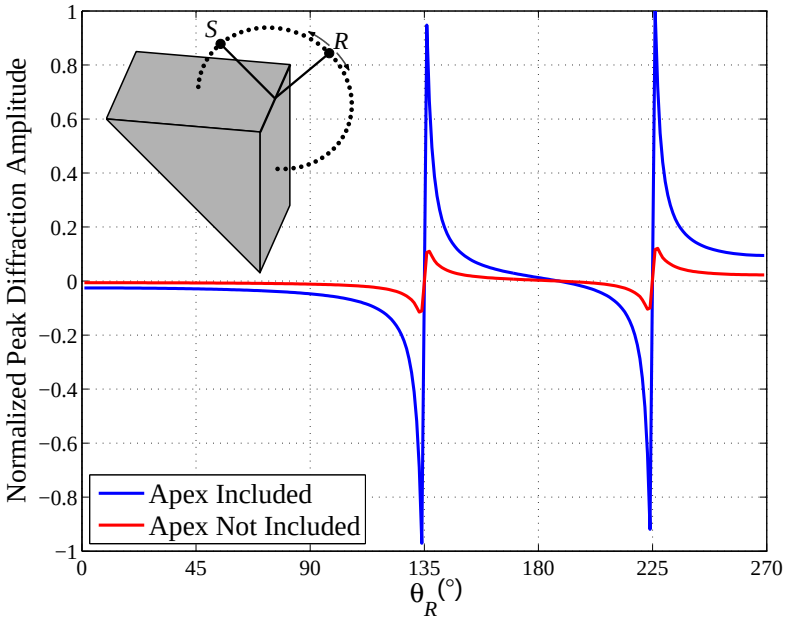

Figure 6.9: Normalized peak diffraction amplitude as a function of the receiver angle for a 270° wedge and a fixed source at $\theta_S = 45°$. Blue curve: data for the geometry shown in the inset. Red curve: S and R have been moved such that the apex point is 0.1 m beyond one end of the 20 m edge. Note the maximum values as the receiver approaches the reflection boundary at 135° and the shadow boundary at 225°.

Given this behavior of the diffracted field relative to the zone boundaries, we identify significant diffracted paths to be retained for processing in this way: the receiver must be within a user-specified angular distance of the *nearest* zone boundary, and the apex point must be included in the physical edge. For the former, this corresponds to

$$\min_i |\nu\varphi_i - 2n\pi| \leq \epsilon, n = 0, 1, 2, ... \tag{6.1}$$

where ϵ is the angular culling threshold, and the receiver is then within ϵ/ν of the nearest zone boundary. For example, consider the geometry from Figure 6.9 with $\nu = 2/3$ and a receiver near the shadow boundary ($\theta_S + \pi$) at 225°. For such a case, $\varphi_2 = \pi + \theta_S - \theta_R$ measures the receiver's angular distance from this (nearest) boundary, and $\varphi_2 = 0$ for a receiver on the boundary. Because the singularity is determined by values of $\nu\varphi_i$ rather than φ_i alone, we would retain the diffracted component if the receiver satisfied $|\nu\varphi_2| \leq \epsilon$, or $|\varphi_2| \leq \epsilon/\nu = 3\epsilon/2$. [5]

[5]The minimum value of ν is 1/2 (when $\theta_W = 2\pi$) so the angular distance to the nearest boundary cannot be greater than 2ϵ.

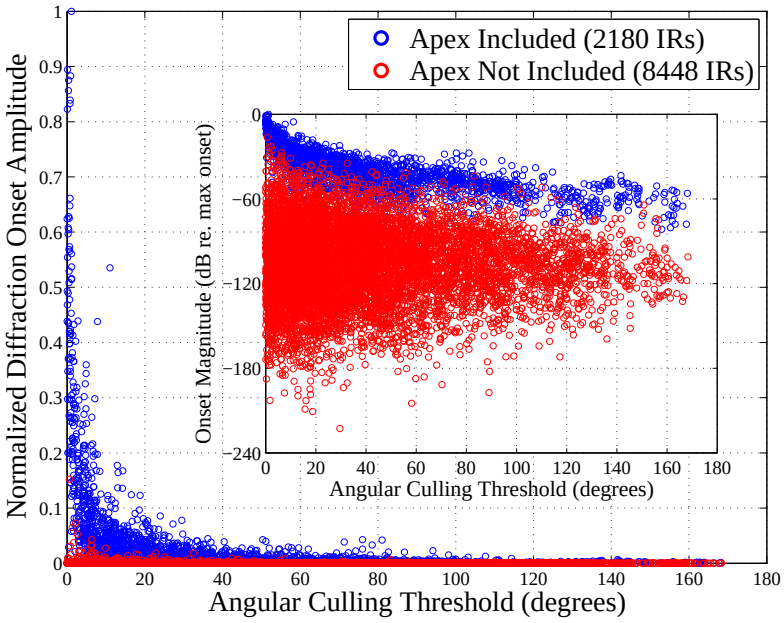

Figure 6.10: Variation in diffraction-IR onset amplitude with angular culling threshold for S_1 and R_3 in the Hall 1 model as described in Section 6.3. Data for 10628 diffraction IRs are shown. The inset shows normalized log-magnitude onset values.

In Figure 6.10, the diffraction onset amplitude is shown as a function of angular culling threshold for the full S_1/R_3 IR. It can be seen that the majority of high-amplitude components do indeed occur when the angular distance is small and the apex point is included in the edge (blue circles), and that this culling method can effectively eliminate a large percentage of the smaller, insignificant diffraction IRs (red circles).

Using the zone-boundary culling method, we calculated impulse responses for the two source positions and seven receiver positions in both models as described in Section 6.2.1. The culling thresholds were chosen to match as closely as possible the average percentage of included diffraction components to the percentage of amplitude-ranked diffraction components used in Section 6.3.1.1: 0.5, 2.0, 8.0, and 32.0 percent for both models, with the addition of 9.0 percent for Hall 2.

Averaged over all fourteen source/receiver combinations in Hall 1, a culling angle of 1° resulted in the inclusion of 0.43 percent of the diffraction IRs, 5° resulted in the inclusion of 1.99 percent of the diffraction IRs, 24° resulted in the inclusion of 8.08 percent of the diffraction IRs, and 180° resulted in the inclusion of 19.5 percent of the diffraction IRs. Similar but not identical angles were found to match the

Table 6.2: Comparison of rank-based culling and zone-boundary culling for Halls 1 and 2. Column 3 contains the number of diffraction IRs retained for each of the rank-based culling cases. Column 5 contains the number of diffraction IRs retained for the corresponding zone-boundary culling cases. Column 6 contains the number of matches, or common IRs, between the two. Data are averaged over all 14 S/R pairs for each model.

Hall	Rank Percent	# Diff. IRs Retained	Culling Angle	# Diff. IRs Retained	Matches
1	8.0	837	24°	836	658
	2.0	210	5°	207	152
	0.5	53	1°	45	31
2	9.0	649	26°	631	493
	2.0	145	3.5°	142	103
	0.5	37	0.8°	35	23

culling percentages for the IRs from Hall 2. A culling angle of 0.8° resulted in the inclusion of 0.50 percent of the diffraction IRs, 3.5° resulted in the inclusion of 2.07 percent of the diffraction IRs, 22° resulted in the inclusion of 7.99 percent of the diffraction IRs, 26° resulted in the inclusion of 9.00 percent of the diffraction IRs, and 180° resulted in the inclusion of 17.72 percent of the diffraction IRs. It was not possible to approximate the 32-percent cases more closely because, on average, only 19.5 and 17.72 percent of the diffraction IRs had the apex point included for Hall 1 and Hall 2, respectively.

Table 6.2 provides a comparison of rank-based culling and zone-boundary culling for the three well-approximated cases in the two models. The last column contains the number of matches, or common IRs, between the two methods. It can be seen that the zone-boundary culling captures approximately 75 percent of the desired highest-amplitude IRs for the 5° and 24° cases for Hall 1 and the 3.5° and 26° cases for Hall 2, but the performance falls below 70 percent for the 0.5° and 0.8° cases.

6.4.1 Hall 1: Visible Sources on Stage

For the analysis of the zone-boundary culling method with unoccluded sources, IRs were generated for Hall 1 (Figure 6.2) with the same two source positions and seven receiver positions as used with the rank-based culling in Section 6.3.1. The error introduced by the culling was evaluated both numerically and subjectively.

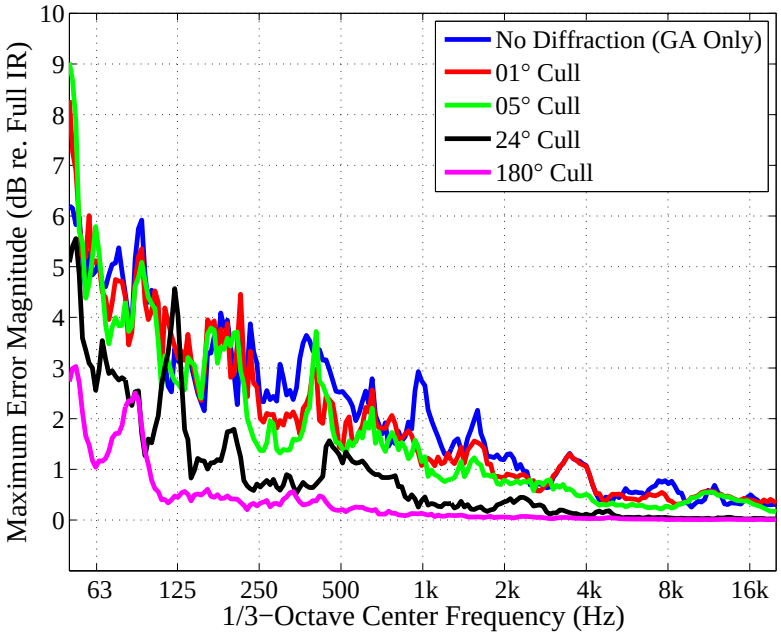

Figure 6.11: Maximum error, taken over all 14 source/receiver pairs, in the smoothed magnitude spectrum for various zone-boundary culling cases in the Hall 1 model. Values in the legend indicate the angular culling threshold.

6.4.1.1 Numerical Analysis

The maximum third-octave error spectrum incurred for each of the zone-boundary culling cases over all 14 source/receiver pairs in Hall 1 is shown in Figure 6.11. Errors for simulations containing no diffraction IRs are shown for comparison, and are identical to those shown for the GA-only case in Figure 6.5.

The error is again quite low at high frequencies for all culling cases, although somewhat higher than that for the rank-based culling cases due to the imperfect retention of the largest diffraction components. Below 1 kHz the error is erratic, but tends to grow with decreasing frequency as expected from the culling of thousands of IRs. Below approximately 250 Hz, the error for the 1° and 5° culling cases is quite similar to that for the GA-only case. The 24° case has noticeably lower error and is similar to that for the 8% amplitude culling case except for the peaks near 125 and 50 Hz, suggesting that the threshold of audibility will occur for the IRs culled with a 24° threshold.

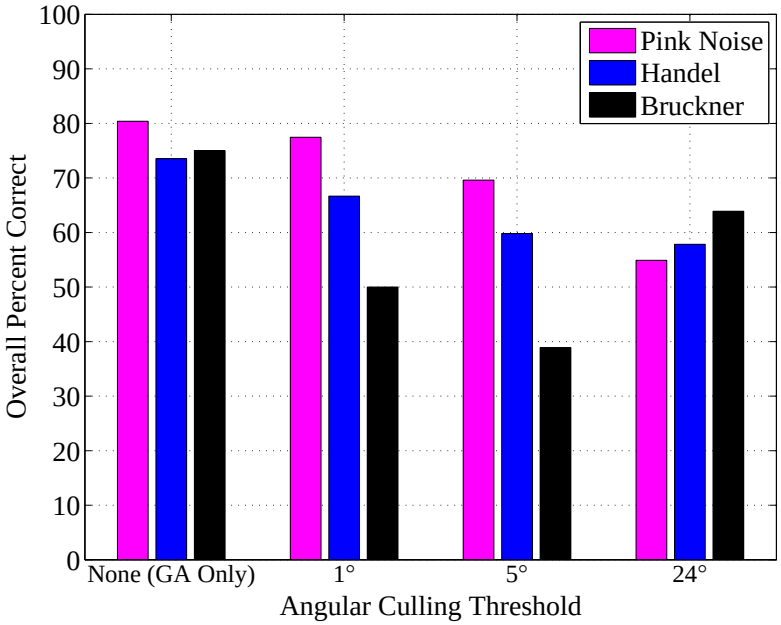

Figure 6.12: Results from our listening tests for zone-boundary culling in the Hall 1 model. For the pink-noise and Handel auralizations, responses have been averaged over 17 subjects and 6 source/receiver pairs. For the Bruckner auralizations, responses have been averaged over 9 subjects and 4 source/receiver pairs. See the text in Section 6.4.1.2 for details.

6.4.1.2 Subjective Analysis

Listening tests were also conducted for the zone-boundary culling cases in Hall 1 with the same methodology as described in Section 6.3.1.2. Subjects were presented with comparisons of full-diffraction IRs and culled IRs with $1°, 5°$, and $24°$ culling thresholds. For the pink-noise and Handel auralizations, the six source/receiver combinations were used, and 16 of the 17 subjects also participated in the tests of rank-based culling. Of those subjects that participated in both tests, a randomly chosen half were tested with rank-based culling first, and the other half with zone-boundary culling first to avoid a learning bias in their responses. 9 subjects participated in the Bruckner-based tests which included four source/receiver pairs.

Overall results from the listening tests are presented in Figure 6.12. The first group of bars again represents the subjects' performance when comparing the GA-only auralizations to the full-diffraction auralizations. Since neither the GA-only nor the full-diffraction IRs changed between the rank-based culling tests and the zone-boundary culling tests, the performance should be (and is) quite similar between the two (see Figure 6.7).

Each of the three remaining groups of three bars indicates the performance of the subjects for one of the culling cases. The data are averaged over the corresponding source/receiver pairs and subjects, and are shown for each source type individually. The subjects' performance with the pink-noise source over all of the zone-boundary culling cases is quite similar to that for the rank-based culling cases, while their performance with the Handel source is slightly improved for the zone-boundary cases. This improved discrimination performance (equivalent to decreased culling effectiveness) is the result of the imperfect retention of the largest diffraction components as shown in Table 6.2. The results from the Bruckner auralizations, particularly the 39% discrimination for the 5° culling case, are suspect due to the low number of subjects, but again indicate a variation in culling effectiveness with the source material. However, the similarity in the pink-noise and Handel results for the amplitude and zone-boundary methods suggests that the zone-boundary culling is approximating the rank-based culling fairly well, and the poor discrimination with the 24° culling threshold indicates that the corresponding auralizations cannot be distinguished reliably from the full-diffraction auralizations.

Test results for each individual source/receiver pair, source type, and culling case are provided in Table 6.3. The significance level of 0.05 (12 of 17 responses or 8 of 9) was achieved for 12 of the 16 GA-only examples, 10 of the 16 1°-culling examples, 5 of the 16 5°-culling examples, and only 3 of the 16 24°-culling examples.

6.4.2 Hall 2: Occluded Sources in the Pit

Numerical analysis of the zone-boundary culling method with occluded sources was carried out on IRs simulated in the Hall 2 model (Figure 6.3). The maximum third-octave error spectrum incurred for each of the zone-boundary culling cases over all 14 source/receiver pairs in Hall 2 is shown in Figure 6.13. Error for the simulations containing no diffraction IRs is shown for comparison.

The error for the 0.8° culling case is quite similar to that for the GA-only (no diffraction) case, with an improvement of only approximately 1 - 2 dB over much of the audible spectrum. This is in contrast to the significant improvement provided by the corresponding 0.5-percent culling case described in Section 6.3.2. The difference is likely due to the mediocre 66-percent matching performance (23 of 35 as shown in Table 6.2) combined with such a small angular threshold: the few retained,

Table 6.3: Correct/incorrect responses for the subjective tests of zone-boundary culling. Bold pairs indicate those for which the 0.05 significance level is met or surpassed, suggesting reliable discrimination between the auralizations with culled and unculled impulse responses. For the Handel and pink-noise auralizations, each entry represents the responses of 17 test subjects. For the Bruckner auralizations, each entry represents the responses of 9 test subjects.

	Pink Noise				Handel				Bruckner			
	GA Only	1°	5°	24°	GA Only	1°	5°	24°	GA Only	1°	5°	24°
S_1, R_4	**12/5**	**14/3**	**12/5**	10/7	**12/5**	8/9	10/7	**12/5**	N/A	N/A	N/A	N/A
S_1, R_5	**14/3**	**12/5**	**14/3**	8/9	9/8	10/7	**12/5**	11/6	N/A	N/A	N/A	N/A
S_1, R_7	**13/4**	**13/4**	**14/3**	**13/4**	**12/5**	**12/5**	11/6	8/9	**9/0**	4/5	6/3	5/4
S_2, R_2	**15/2**	**12/5**	9/8	11/6	**15/2**	**12/5**	10/7	10/7	7/2	4/5	4/5	6/3
S_2, R_3	**15/2**	**16/1**	**13/4**	5/12	**13/4**	**14/3**	10/7	9/8	6/3	4/5	1/8	4/5
S_2, R_7	**13/4**	**12/5**	9/8	9/8	**14/3**	**12/5**	8/9	9/8	5/4	6/3	3/6	**8/1**

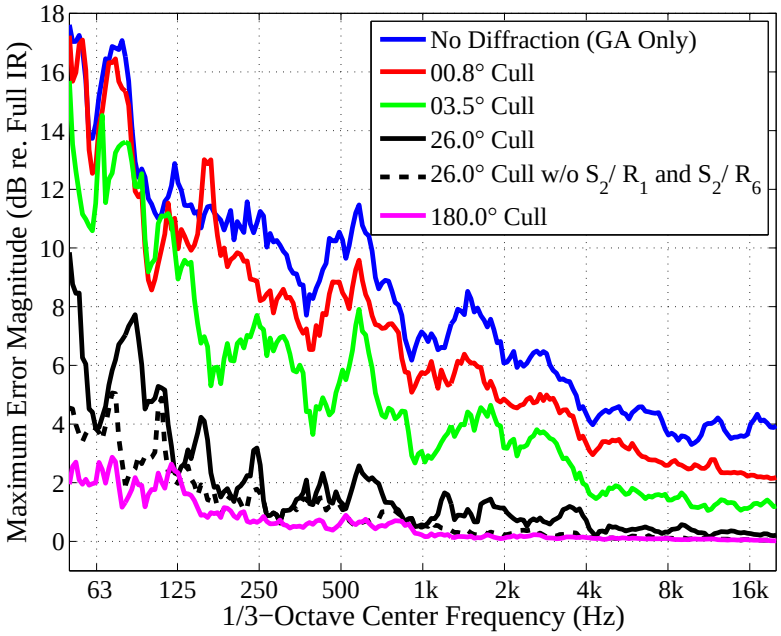

Figure 6.13: Maximum error, taken over all 14 source/receiver pairs, in the smoothed magnitude spectrum for various zone-boundary culling cases in the Hall 2 model. Values in the legend indicate the angular culling threshold. Compare to Figure 6.11, but note the change in the y-axis limits.

high-amplitude diffraction components do not contain a sufficient fraction of the diffracted energy to provide a meaningful correction. The error for 3.5° culling case is also significantly higher than that for the corresponding 2-percent case. This is largely the result of the two IRs simulated for receiver R_6, which have the two lowest numbers of GA components and the two worst matching performances of all 14 S/R combinations.

For the 26° culling, the error is comparable to the 9-percent case above the 125-Hz band, but higher at low frequencies. This is due mainly to the low-frequency error in the S_2 to R_1 and S_2 to R_6 IRs, as shown in Figure 6.13 with the dashed black curve that indicates the error when these two IRs are omitted from the analysis. For these two S/R pairs the source and receiver are close together *and* close to a number of diffracting edges, specifically the upper and lower edges of the stage lip, the edge of the balustrade, and, only for R_6, the vertical edge at the house-left, front end of the audience seating area seen in Figure 6.3. The combination of short source-to-edge and receiver-to-edge distances, m and l respectively in the denominator of the integrand in Equation 3.13, causes an increase in the diffraction amplitude independent of the apex-point and zone-boundary behavior, and thus for

these specific S/R pairs high amplitude diffraction IRs are missed by the angular culling technique.

Overall, the performance of the zone-boundary culling technique was reduced when used with simulations from Hall 2 in which the sources were occluded from the receivers. The increased error was due to two main factors. First, the diffracted components contain a more significant portion of the energy transmitted from the sources to the receivers than in the visible-source IRs from Hall 1. This factor is particularly influential with the smallest culling angles. Second, the Hall 2 simulations contained certain S/R pairs for which the source and receiver were both close to a number of diffracting edges, and such a configuration can lead to diffraction components whose high amplitude is dictated by the short propagation distance rather than by the receiver's proximity to a zone boundary. However, only a small angular increase of 2° (from 24° to 26°) was needed to provide an error similar to that of the unoccluded-source simulations in Hall 1 when this edge-proximity issue was avoided.

6.5 Discussion

As has been shown in [85], identifying the possible sequences of reflecting surfaces and diffracting edges in a virtual environment can be more time consuming than evaluating the contributions of the valid paths (*i.e.* computing the diffraction IRs). [6] Thus, for our culling method to have maximal impact on the overall processing time of a virtual-acoustic simulation, it should be integrated into the path-finding stage as well. This can be achieved most easily in the context of beam tracing. As mentioned in Section 6.1, beam-tracing systems exist that allow for diffraction culling by limiting diffracted beams to the shadow regions of diffracting wedges [85, 271]. Using our culling approach as an alternative, diffracted beams could be limited to small angular regions around the reflection and shadow boundaries (which can be computed easily using the beam and wedge geometry). For each combination of surfaces and an edge that leads to a possible diffracted path, computation can be stopped once the apex-point status has been determined. Because our culling

[6] However, our more accurate BTM-diffraction IR computation is likely more time consuming than methods such as the UTD (although no timing comparison has been made thus far), so culling at the computation stage may be more valuable than in previous work.

method was implemented in the Edge Diffraction Toolbox for Matlab® [254][7] and only in the diffraction calculation stage, we currently cannot provide timing statistics that indicate the full advantage of our approach or that confirm its viability for interactive simulations. However, averaged over all S/R pairs, the 24° culling resulted in an 95 percent decrease in the diffraction processing time for the IRs in Hall 1 and the 26° culling resulted in an 88 percent decrease for Hall 2. Earlier tests of our method reported in [33] with a 30° culling threshold also indicate that the time to compute the contributions of the diffraction IRs can be significantly reduced.

In addition to the potential reduction in processing time, our zone-boundary-based culling approach guarantees a smooth transition across the reflection and shadow boundaries where GA components are discontinuous. This may be particularly helpful in dynamic simulations to prevent audible artifacts when a receiver crosses a zone boundary and a GA component suddenly is added to or removed from the impulse response. The simulated sound field would contain discontinuities at the ends of the "culling zone", but these would be significantly reduced in size relative to the discontinuities at the zone boundaries when diffraction is neglected entirely.

We have also studied the additional culling that can be achieved when small diffraction IRs are further culled by introducing an onset-magnitude threshold to the zone-boundary method. This method works by comparing the onset sample of each diffraction IR to a threshold, and only paths for which the threshold is exceeded are retained. For each diffracted path, the threshold is based on the largest prior diffraction onset sample. Preliminary results for this method were presented previously [33, 256], where culling based on the onset sample, or the first two samples, of a diffraction IR using various thresholds (*e.g.* 20, 30, or 40 dB below the prior maximum) was shown to be effective in reducing computation time with limited spectral error in the early simulated sound field. This method identifies the significant diffraction paths more effectively than the angular method alone, but sound-field continuity is no longer guaranteed throughout the full angular range of retained IRs. It also requires that some computation is done for every diffraction

[7]The Toolbox uses the classical image-source technique to find specular reflections. Diffraction contributions are identified by assigning discrete points, which represent edge segments, along edges and then applying the image-source technique for preceding and subsequent specular reflections.

IR under consideration for culling, so the benefits may be offset by the increase in processing time.

In regard to subjective evaluation of the occluded-source IRs from Hall 2, we opted against further listening tests at this stage for one main reason. The spectral error for the 26° culling case in Hall 2, with the S_2/R_1 and S_2/R_6 IRs omitted, is quite similar to that for the 24° culling case from Hall 1, and thus in the context of our auralizations with omnidirectional IRs, the audible artifacts of culling (or lack thereof) should also be similar. It is clear, however, that ignoring early diffracted paths could have a significant effect on the spatial perception of the simulated sound field in the absence of the direct sound. Further subjective testing is thus necessary as described below, with auralizations rendered either binaurally using HRTFs, or perhaps in an immersive environment using wavefield synthesis or Ambisonics for accurate spatial reproduction.

In regard to the variability of our results with the anechoic source material, similar tests carried out by Torres *et al.* [265] also indicated that perception of diffraction in auralizations with simulated impulse responses was very much source dependent. They report comparable results between pink noise and synthesized organ music, but reduced perception of diffraction with male and female speech as the source material. Similar organ music would be interesting to use in tests with our culling approach. For models with many small surfaces, the error due to neglecting diffraction will spread to higher frequencies and the effects of culling likely will be more evident for a broader range of source material. Some form of culling will be necessary for simulations in such models to manage the computational load since the use of small surfaces will lead to a higher edge count.

6.6 Summary

In this chapter we have addressed the computational complexity of virtual-acoustic simulations that include diffraction. The addition of diffraction to geometrical-acoustics components in a simulation causes a dramatic, combinatorial increase in the number of paths from a source to a receiver that must be considered, but we have shown that only a small subset of these must be processed to maintain high levels of numerical and, in certain cases, perceptual accuracy. Analysis of simulated

impulse responses from two simple concert-hall models indicates that more than 90 percent of the diffracted components can be culled with limited spectral error if the retained components are those with the highest amplitudes. Subjective tests with IRs from a model with unoccluded sources confirm that culling with amplitude-based ranking can be used without audible artifacts, although the effectiveness is dependent on the listening material.

In addition, we have described a method for culling insignificant, singly diffracted paths in a virtual-acoustics simulation. By retaining only diffracted paths for which the receiver is within a given angular distance of the nearest reflection or shadow boundary, and for which the apex point is included in the physical edge, we are able to approximate the performance of the rank-based culling effectively and without pre-processing. Subjective tests verify that auralizations of a simple concert-hall model made with a culling threshold of 24° cannot be distinguished reliably from those made with impulse responses containing all first-order diffracted components (limited to paths up to fourth order), but again the effectiveness is dependent on the listening material.

Chapter 7

Integration of Edge Diffraction and Geometrical-Acoustics Modeling

7.1 Introduction

Aside from a few recent exceptions, room-acoustics modeling systems historically have been limited to simulations based on geometrical-acoustics techniques. In contrast to many frequency-domain analysis approaches, *e.g.* those utilized in studies of highway noise barriers, these simulations are typically carried out in the time domain for various reasons. Time-domain data, *i.e.* impulse responses, allow for intuitive evaluation of the contributions of individual components to the sound field through visual inspection. In addition, they provide results that can be analyzed numerically with standardized parameters such as Reverberation Time, Definition, and others specified in ISO 3382 [108], and perceptually through convolution-based auralization [134]. Despite their widespread use, GA techniques are known to be incomplete and inaccurate, particularly at low frequencies, in part because they fail to include diffraction.

GA techniques rely on ray theory, *i.e.* the approximation that sound propagates between two points along straight, infinitely thin, ray-like paths. Thus, an unoccluded linear path between a source and receiver (with the appropriate attenuation

due to spreading and absorption by the medium) is sufficient to model the direct sound, and specular reflections can be simulated by piecewise linear paths that obey Snell's Law when they encounter flat, reflecting surfaces. Such ray-like behavior is only correct at asymptotically high frequencies[1] or when the dimensions of the reflecting surface are infinitely larger than the wavelength of the incident sound. Therefore GA methods are particularly inaccurate when used with small reflecting surfaces or low-frequency (long-wavelength) sound.

A straightforward approach to remedy this failure involves augmenting GA results with edge-diffraction calculations, e.g. as is done in [211, 254, 265, 271]. However, separate calculations of these two components can limit the accuracy of the simulations because the components are not independent. The relationship between the GA and diffraction components can be seen most easily for a simulation in which the receiver is located on or near a zone boundary. The sum of the associated GA term and the diffraction must yield a continuous sound field across the boundary, and the proper combination of the two components requires that both be simulated with a high degree of numerical accuracy to avoid errors.

In this chapter, we present an integrated approach for time-domain acoustic modeling in which intermediate values normally utilized only in diffraction calculations are exploited in finding GA components as well. Specifically, we show how to detect the existence of first-order specular reflections and an unobstructed direct-sound path using the source and receiver locations specified in edge-aligned cylindrical coordinates. This method can be used for arbitrary source and receiver configurations, but is particularly well suited for use with receivers at or near zone boundaries because it ensures a consistent, physically correct combination of components. This chapter was published in modified form in [35].

7.2 Integrated Modeling Approach

As mentioned above, it is possible to use intermediate values from the diffraction calculations to find the GA components as well. In particular, the φ_i angles defined in Eq. (3.4) contain sufficient information to detect the existence of an unobstructed

[1] Fresnel volumes [138] and zones [14] provide more accurate, frequency-dependent estimates of the finite volume of space and area of a surface, respectively, that influence the propagation and reflection of sound.

direct-sound path as well as first-order specular reflections. Additionally, the radial and angular coordinates of the source and receiver, r_S, r_R, θ_S, and θ_R, can be used to locate the reflection point on a surface that is found to cause a specular reflection.

Our method assumes that the environment/model is stored as a triangle mesh, with explicit lists of faces, edges, and vertices. A single pass over the list of edges is used to generate and store the diffraction parameters, and to calculate the diffraction components of the sound field. For edges that occur at the intersection of two faces (*i.e.* at corners and wedges, as opposed to "free" edges at the ends of isolated surfaces such as the panels in the array discussed in Section 5.4.2 and shown in Fig. 5.6), the parameters must be measured relative to both faces, since either or both could occlude the direct sound or create a specular reflection. The actual diffraction calculations for the edge can be made with the parameters relative to either face. For edges that are known not to diffract, e.g. those for which $\theta_W = \pi/m$ for integer values of m [18, 129], the parameters must still be generated for use in detecting the GA components, but the diffraction calculations can be skipped.

In a subsequent processing pass over the list of faces, the diffraction parameters for the three edges of each face are evaluated to determine whether or not the face obstructs the direct sound or creates a specular reflection. Specifically, two counters are maintained for each face: one with the number of its edges for which $\varphi_2 < 0$, and one with the number of its edges for which $\varphi_4 > 0$. As described below, a face obstructs the direct sound if the value in its first counter is 3, and the face creates a specular reflection if the value in its second counter is 3. For a face that creates a specular reflection, further evaluation of the parameters can be used to find the reflection point. Once a face has been found to obstruct the direct sound, no other faces need to be tested for such an obstruction. Once a specular reflection has been found to be created by a face, no other faces in the same plane need to be considered for reflections.

7.2.1 Direct-Sound Occlusions

To determine whether there is an unobstructed direct-sound path from the source to the receiver, each face in the model must be considered as a possible occluder. Relative to *one* of its three edges, a face will occlude the direct-sound path if

$\theta_R > \pi + \theta_S$, *i.e.* the receiver is beyond the shadow boundary as described in Section 4.2.1. Thus occlusion relative to an edge occurs when

$$\pi + \theta_S - \theta_R = \varphi_2 < 0. \tag{7.1}$$

If φ_2 is negative for *all three* edges of a face, the face occludes the direct sound. An example is shown in Figure 7.1. Because this test is carried out for every face, *i.e.* the coordinate system is aligned such that each face under test is in the $\theta = 0$ plane, it is not necessary to consider the shadow boundary associated with φ_3 and the face at $\theta = \theta_W$.

This method for determining occlusion can be confirmed geometrically by the following. Each edge of a face is contained by an infinite line, and each such line divides the plane of the face into two half-planes: one that contains the face and one that does not. For a given edge, $\varphi_2 < 0$ implies that that the line segment between the source and the receiver intersects the half-plane that contains the face, as can be seen by the intersection of the horizontal line representing the face and the line segment between S and R_2 in Figure 7.1(a). Once φ_2 has been evaluated for all three edges, the point at which the path from the source to the receiver passes through the plane of the face can be localized to the intersection of three half-planes, each dictated by the sign of one φ_2 value. As seen in Figure 7.1(b), the intersection of the three half-planes defined by $\varphi_2 < 0$ for all edges is exactly the face, and thus three negative values imply that the path from the source to the receiver goes through the face, *i.e.* is occluded by it. No other combination of three half-planes contains any portion of the face, so a single case of $\varphi_2 > 0$ for a given face eliminates that face from the list of possible occluders of the direct sound. The case of $\varphi_2 = 0$, when the segment between S and R intersects an edge of a face and thus the receiver is on the shadow boundary, is discussed in Section 7.3 below.

7.2.2 First-Order Specular Reflections

The test for a specular reflection from a face involves evaluating φ_4 for each of the face's three edges. As defined in Eq. (3.4) and discussed in Section 4.2.1 $\varphi_4 = \pi - \theta_S - \theta_R$ and thus it measures the angular distance of the receiver from the specular boundary $\pi - \theta_S$ for the face at $\theta = 0$. As shown in Figure 7.2, when

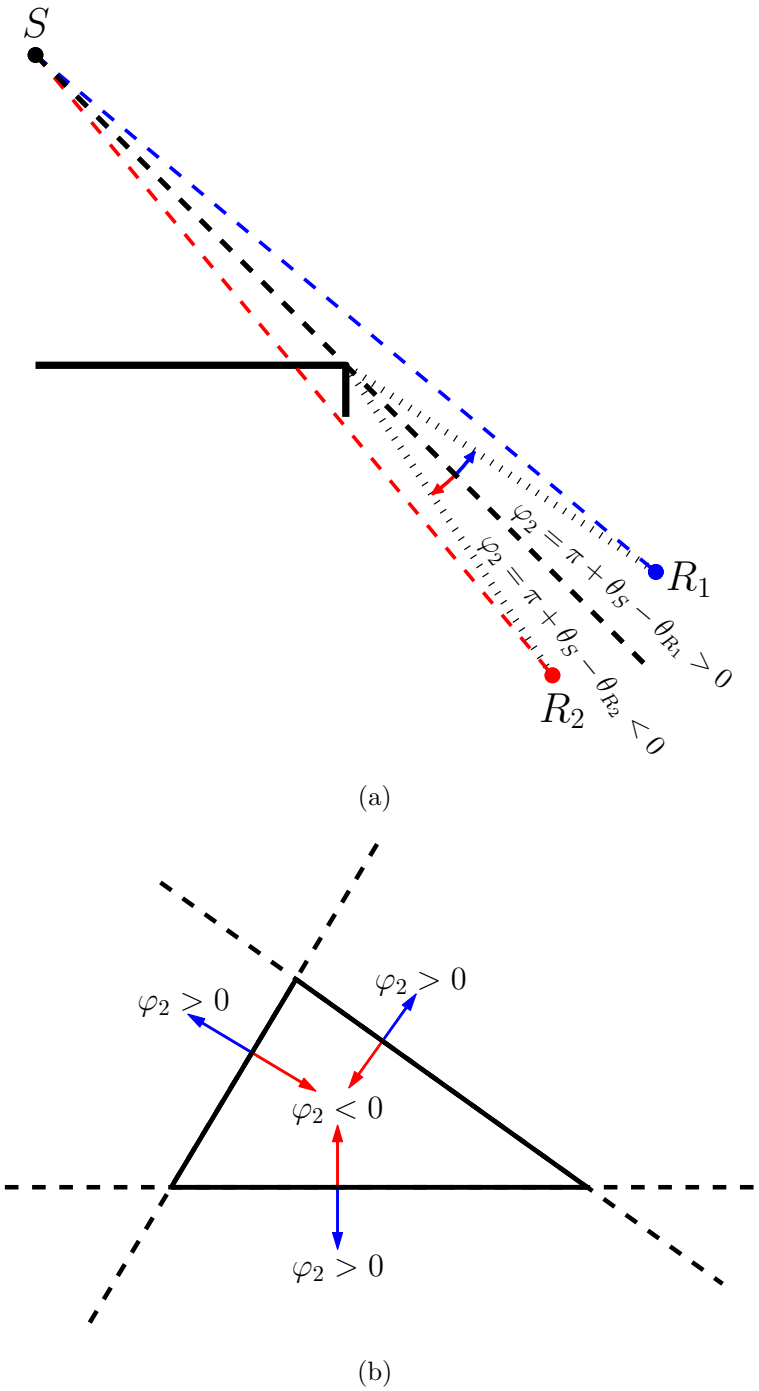

Figure 7.1: Checking for occlusion of the direct sound. (a) The face under test is shown as a horizontal line, and the edge under test is perpendicular to the page. The diffraction parameter $\varphi_2 = \pi + \theta_S - \theta_R$ measures the angular distance of the receiver from the shadow boundary. If $\varphi_2 < 0$ (e.g. for R_2), the receiver is beyond the shadow boundary relative to the edge under test. (b) If $\varphi_2 < 0$ for all three edges of the face, the face occludes the direct sound.

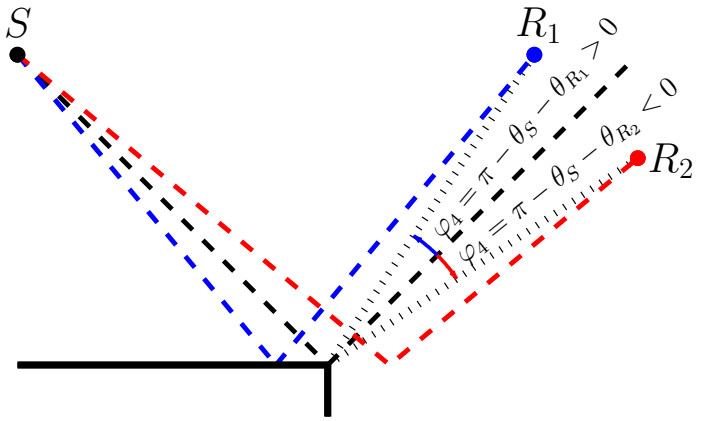

(a)

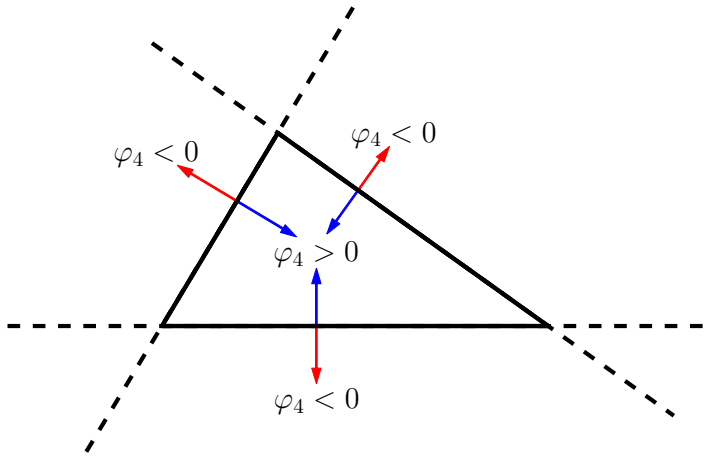

(b)

Figure 7.2: Confirming a specular reflection. (a) The face under test is shown as a horizontal line, and the edge under test comes out of the page. The diffraction parameter $\varphi_4 = \pi - \theta_S - \theta_R$ measures the angular distance of the receiver from the specular boundary. If $\varphi_4 > 0$ (e.g. for R_1), the receiver is within the specular zone relative to the edge under test. (b) If $\varphi_4 > 0$ for all three edges of a triangular face, the face creates a specular reflection.

$\varphi_4 > 0$, the receiver is within the specular zone relative to the edge from which θ_S and θ_R are measured. If $\varphi_4 > 0$ for all edges of a face, the face creates a specular reflection. Note that the evaluation of φ_4 need only be done if both $\theta_S < \pi$ and $\theta_R < \pi$. If either is greater than π, there can be no specular reflection from the reference face.

A similar geometric argument to that for the direct-sound occlusion case holds in the reflection case as well. For a given face and one of its edges, $\varphi_4 > 0$ implies that that the point of specular reflection lies in the half-plane that contains the face, as

can be seen by the reflection path between S and R_1 in Figure 7.2(a). The three φ_4 values localize the reflection point to the intersection of three half-planes, and this intersection for three positive φ_4 values is exactly the face as shown in Figure 7.2(b). If $\varphi_4 = 0$ for an edge, the reflection point is on the edge and the receiver is on the reflection boundary. This case is discussed in Section 7.3 below.

Once a face has been found to create a specular reflection, the source could be mirrored about the plane of the face and the reflection point could be determined by the intersection of the line segment connecting the image source and the receiver with the face. However, it is also possible to find the point of reflection using the diffraction parameters. This method involves deriving the barycentric coordinates of the point within the reflecting (triangular) surface, and is similar to one that is commonly used in computer graphics, specifically in ray-tracing applications, to find line-triangle intersections.

To find the coordinates of the specular-reflection point, it is helpful first to consider a 2D example as shown in Figure 7.3(a). Given a source, receiver, and a line segment, the goal is to find the distance x of the reflection point from the end of the segment in terms of the diffraction parameters r_S, r_R, θ_S, and θ_R. With the constraint that $\alpha_1 = \alpha_2$ (true for a specular reflection), x is given by the equation

$$x = \frac{r_S r_R \sin(\theta_S + \theta_R)}{r_S \sin(\theta_S) + r_R \sin(\theta_R)}. \tag{7.2}$$

For a 3D case, consider the source S, receiver R, and triangular face $\triangle ABC$ in Figure 7.3(b) for which $\varphi_4 > 0$ for all three edges. The first-order specular reflection path from S to R must go through a point P in the interior of the face, and the value x in Eq. (7.2) corresponds to the perpendicular distance from P to the edge from which r_S, r_R, θ_S, and θ_R are measured. Therefore, using side BC as a reference yields x_{BC}, using side CA yields x_{CA}, and using side AB yields x_{AB}. The triple (x_{BC}, x_{CA}, x_{AB}) represents the location of P in exact trilinear coordinates. This triple can be converted into barycentric coordinates (t_1, t_2, t_3) [287], where

$$t_1 = \frac{x_{BC} \cdot a}{n}, \quad t_2 = \frac{x_{CA} \cdot b}{n}, \quad t_3 = \frac{x_{AB} \cdot c}{n}, \tag{7.3}$$

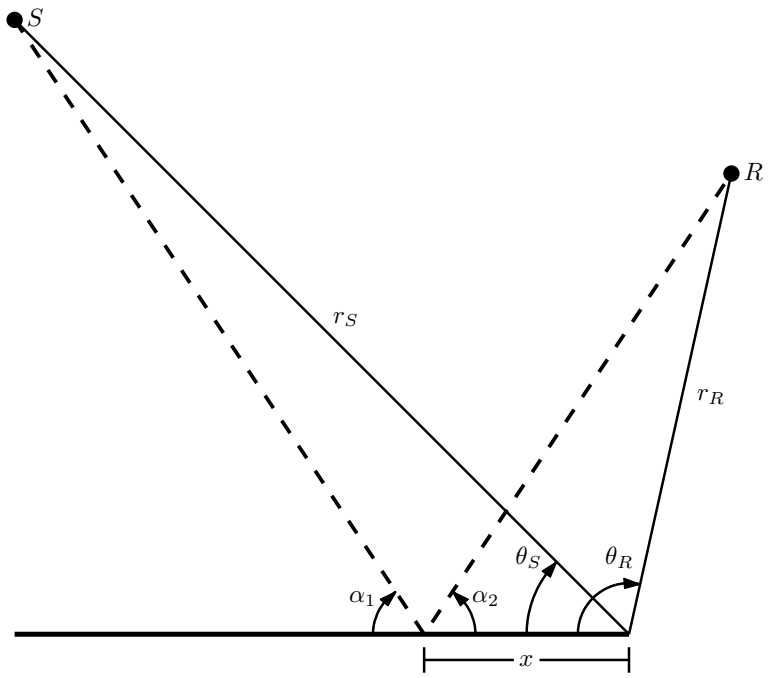

(a)

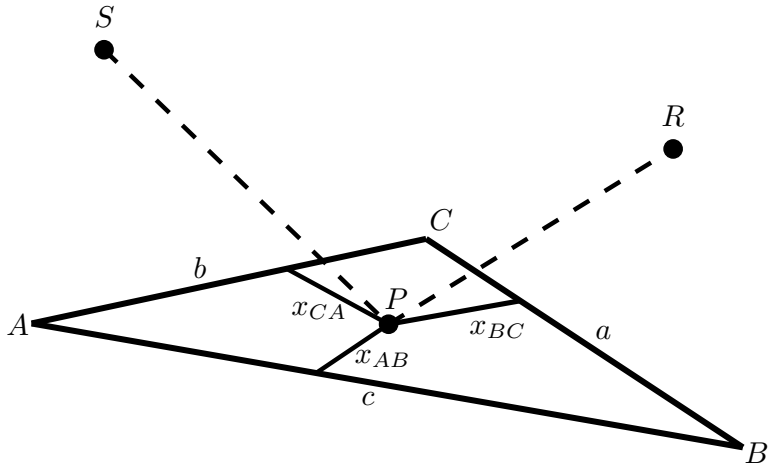

(b)

Figure 7.3: Finding the reflection point P. (a) 2D geometry used to find the distance x of P from an edge. (b) Values x_{AB}, x_{BC}, and x_{CA}, each calculated with Eq. (7.2) relative to one of the three edges, give the location of P in exact trilinear coordinates. These can be converted into barycentric coordinates using Eqs. (7.3) and (7.4), which in turn give the Cartesian coordinates of P through Eq. (7.5).

a, b, and c are the lengths of the sides of the face as shown in Figure 7.3 (b), and

$$n = a \cdot x_{BC} + b \cdot x_{CA} + c \cdot x_{AB}. \tag{7.4}$$

Using the known Cartesian coordinates of the triangle vertices A, B, and C, the Cartesian coordinates of the specular reflection point can be found with the equation

$$P = A \cdot t_1 + B \cdot t_2 + C \cdot t_3. \tag{7.5}$$

The value $r_S \sin(\theta_S)$ in Eq. (7.2) is the distance from the source to the plane containing the face, and $r_R \sin(\theta_R)$ is the distance from the receiver to that plane. These distances are constant for all edges of a face, and thus must be calculated only once per face. The value $r_S r_R \sin(\theta_S + \theta_R)$ must be computed for each edge.

7.3 Discussion

7.3.1 Accuracy

The benefit of this integrated method in terms of simulation accuracy is most pronounced for a receiver that is on (or very close to) a zone boundary. For such a case involving a specular-zone boundary, the reflection point lies on an edge of a surface, and the reflection arrival time and diffraction onset time are equal. To maintain a continuous sound field across the boundary, the combined amplitude of the specular reflection and the first sample of the diffraction IR should be one half the expected reflection value as described in Section 4.3.5. Because $\varphi_4 = 0$ for such a case, it is easy to note such a condition when processing the related edge (using a small ϵ to avoid numerical inaccuracies), and adjust the diffraction and specular reflection strengths accordingly to achieve the proper amplitude. However, using separate GA and diffraction methods, such a condition would have to be found by the two methods consistently and accurately. In particular, the technique for finding the specular reflections would be required to find path/edge intersections within the same ϵ as the diffraction-modeling technique to ensure proper amplitudes for both components. Failure to detect and combine the two components properly could lead to a response with double the correct amplitude, zero amplitude due to destructive interference, or incorrect diffraction polarity.

7.3.2 Efficiency

This method also provides improved efficiency over the classical image-source method (although methods such as beam tracing, and more advanced image-source implementations such as in [235] that employ spatial subdivision schemes can detect specular reflections more efficiently). With the image-source method (ISM), faces are evaluated for specular reflections by: mirroring the source about the plane containing the face to create an image source; finding the intersection of that plane with the line between the image source and the receiver; determining whether the intersection point is inside (valid reflection) or outside (invalid reflection) the boundaries of the face. With the new integrated method, the existence of a reflection is determined by simply examining the φ_4 counter for each face. If the counter value is less than 3, nothing more needs to be done. If the counter value is 3, we can either use the method described in Section 7.2.2 to find the exact reflection point, or follow the steps used in the ISM. For the latter, we need only carry out the first two steps. Since the surface, rather than just the plane in which it lies, is known to create a valid specular reflection, the intersection of the path between the image source and receiver with the reflecting plane must be inside the boundaries of the face, so the final step is not necessary.

7.4 Summary

This chapter describes a time-domain method for virtual-acoustic modeling that integrates geometrical-acoustics components and edge diffraction. Parameters generated for the diffraction calculations also are used to confirm an unobstructed direct-sound path and to find first-order specular reflections, thus eliminating the need for a separate GA technique such as the image-source method. This approach is particularly well suited for use with receivers at or near reflection and shadow boundaries, where the proper combination of GA and diffraction components is essential to ensure a physically accurate, continuous sound field across the boundary.

Chapter 8

Conclusions and Future Work

8.1 Summary of Contributions

The goal of this thesis is to explore the use of edge diffraction in virtual-acoustic simulations. In particular, we have focused on a line-integral formulation of the time-domain Biot-Tolstoy-Medwin diffraction expression that provides an exact first-order diffraction impulse response for rigid wedges of finite length. In this context, our contributions comprise four main advances.

First, we have explored the singular behavior of the diffraction integrand near reflection and shadow boundaries, and specifically described the relationship between the periodic singularity and higher-order reflections within wedges with an open angle less than 180°. This singularity is necessary to maintain a continuous sound field where the geometrical-acoustics components are discontinuous, and thus its proper treatment is critical for physically accurate simulations.

Second, we have evaluated three edge-subdivision strategies to provide discrete-time impulse responses from continuous-time, line-integral diffraction formulations. The first, in which the edge is segmented such that each portion contributes to exactly one sample of the IR, is the most accurate but suffers from high computation time. The second, in which all segments within an edge are of equal length, provides a significant reduction in computation time but is numerically problematic when a segment spans the apex point on an edge. The third, a hybrid of the two using sample-aligned segments near the apex point and even segments elsewhere, allows

for fast computations with low error and straightforward numerical evaluation. Given the singular behavior of the diffraction integrand near the apex point and the resultant high onset amplitude of the diffraction IR, this hybrid technique has the advantage of concentrating the computational effort on the portion of the edge that contributes the most diffracted energy, and allows for relaxed numerical accuracy for numerically and perceptually less important segments.

Third, we have addressed the combinatorial increase in the computational complexity of virtual-acoustic simulations due to the inclusion of diffracted paths. Through objective and subjective analysis, we have shown that only a small subset of diffracted paths must be processed to maintain high levels of numerical and, in certain cases (dependent on the source material), perceptual accuracy. In addition, we have described a method for culling insignificant, singly diffracted paths in a virtual-acoustics simulation. By predicting diffraction amplitudes through the singular behavior of the diffraction onset near reflection and shadow boundaries, we can identify strong components to be retained and weak components to be omitted before they are fully processed.

Finally, we have described a time-domain method for virtual-acoustic modeling that integrates geometrical-acoustics components and edge diffraction. Parameters generated for the diffraction calculations are used to confirm an unobstructed direct-sound path and to find first-order specular reflections, thus eliminating the need for a separate GA technique such as the image-source method. This approach is particularly well suited for use with receivers at or near reflection and shadow boundaries, where the proper combination of GA and diffraction components is essential to ensure a physically accurate, continuous sound field across the boundary.

8.2 Future Work

The research summarized in this thesis suggests several avenues for future work related to diffraction calculations and acoustic simulations.

8.2.1 Direct Extensions of This Thesis

Clearly, the edge subdivision and culling techniques described in Chapters 5 and 6, respectively, must be integrated into an interactive modeling system to determine the full benfits of the associated reductions in computation time. Various authors (*e.g.* see [37, 271]) have mentioned using BTM diffraction in their simulation systems as a more accurate alternative to the UTD, while others (see [270]) have expressed concern about its computational complexity. Integration of BTM diffraction into an interactive system not only will allow our acceleration techniques to be evaluated more fully, but will provide a framework for comparing UTD and BTM diffraction in terms of numerical and perceptual differences, and a vehicle for more general studies of the audibility of diffraction in virtual-acoustic simulations.

In regard to further perceptual studies, our auralizations described in Chapter 6 were made with omnidirectional impulse responses and were presented diotically, so we did not take into consideration the directional aspects of the diffracted components and how these might affect their audibility. Torres *et al.* [265] have suggested a method for binaural auralization of diffraction based on the arrival direction of the least-time path, and this may be a suitable way to study diffraction in a three-dimensional sound field simulation. In addition, diffraction arrival time may also be an important factor to evaluate perceptually. For environments in which the direct sound may be occluded, a diffracted path can represent the first arrival at a receiver and thus may be critical for proper localization. Arrival time may also be important when the simulated impulse response is sparse and the diffracted components are temporally isolated, and thus are less likely to be masked by the GA components. Torres *et al.* also describe results from perceptual tests which indicate that second-order diffraction was inaudible in their simulations, but second and higher orders should be studied in other environments, specifically ones where they represent the shortest or only propagation paths from source to receiver or around obstacles. Finally, the audibility of sound-field discontinuities at reflection

and shadow boundaries is given as a motivation for simulating diffraction in Chapter 6 and in [271], but this has not been explored rigorously. Further perceptual studies should be carried out to determine the circumstances under which these discontinuities are indeed problematic and thus GA-only simulations are insufficient.

In regard to the method of integrating diffraction and GA modeling described in Chapter 7, one aspect that demands further study is the need for visibility checks for the specular reflections. In traditional GA systems, rays are cast along each reflection-path segment, and tested for intersection with the surfaces in the model. If one of these rays intersects a surface before arriving at the expected reflecting surface, the reflection is considered invalid. This technique could be used with our method. Another possibility is to check for occlusions for each segment of a reflection path using the approach to check for occlusions of the direct sound described in Section 7.2.1. A reflection path $S \rightarrow P \rightarrow R$ could be evaluated by first searching for obstructions with S as the source and P as the receiver, and then for obstructions with P as the source and R as the receiver. It may be possible to incorporate such visibility checks into the calculations for higher-order sound-field components.

A second augmentation of our diffraction/GA integration method involves extension beyond first-order specular reflections and diffraction. As in the first-order case, diffraction compensates for discontinuities at higher-order specular-zone boundaries, so our integrated method should be applicable. However, additional tests will be necessary to validate each segment of higher-order specular reflection path.

Finally, it should be possible to use convex faces other than triangles, with a modified process for finding specular reflection points. This could increase the method's efficiency by reducing the number of edges and faces to process.

8.2.2 Novel Simulation Techniques

One aspect of existing techniques and systems for virtual-acoustic simulations, particularly those based on geometrical-acoustics assumptions, that invites further study is the use of single-resolution geometric models. While frequency-dependent scattering coefficients can be used to provide variations in the scattering behavior of surfaces between octave or third-octave bands, and the *strength* of specular reflec-

tions can vary with frequency due to surface size and absorption, the *direction* of specular reflections is typically modeled as a frequency-independent characteristic. Clearly this is not physically realistic, but is an artifact of the GA assumption that wave/surface interactions occur at infinitesimally small points rather than over finite, wavelength-dependent areas (*i.e.* Fresnel zones [14]). A specularly reflected ray or the reflection path determined by the image-source model only considers the local surface normal at the path/surface intersection to determine the outgoing propagation direction.

One approach to address this problem involves using multiple geometric models for a simulation, perhaps one for each octave band across the spectrum of interest. If each model contained a level of detail appropriate for the simulation frequency/wavelength, reflection and scattering behavior could be simulated more accurately. The additional computation time for such an approach would likely make it inappropriate for interactive systems, but the improved accuracy could be valuable for offline simulations. The commercially available software CATT Acoustic [52] currently uses a separate ray tracing pass for each octave band to model frequency-dependent scattering, so multiresolution geometry perhaps could be incorporated with limited computational overhead. The necessity to create multiple models for the same space could be quite tedious and thus is a serious impediment to the multi-model approach, but this could be overcome through the use of automatic geometry simplification.

Geometric simplification has been thoroughly explored in computer graphics, and various techniques have been described to reduce the level of detail in 3D meshes including edge collapses [88], low-pass filtering [260], local planar approximation [44], and others [87, 165]. It has also been applied to a limited extent in acoustics, although the goal typically has been to reduce model complexity to a single, computationally more manageable level in the context of BEM/FEM modeling [92, 99] (a process known as mesh coarsening) or room-acoustics simulation [116, 239, 240]. If the simplification algorithm includes a frequency-dependent termination criterion, *e.g.* a minimum surface dimension to wavelength ratio, it could take a highly detailed model as input and create a series of output models, one for each frequency band with an appropriate level of detail. A 2D example of this is described by Hoshi *et al.* [106], who use elliptic Fourier descriptors to create multiresolution models for acoustic ray-tracing. Further work in this area could yield interesting results.

One possible problem with existing simplification methods is that they act solely on the geometry and ignore other potentially important aspects of a simulation such as the source and/or receiver positions. Fresnel zones [14], the grating equation for scattering from periodic surfaces [26], and the Rayleigh criterion for rough-surface scattering [197] all include various source-related parameters such as distance and angle of incidence in addition to frequency, suggesting that a new multiresolution modeling approach should incorporate these parameters as well. To this end we have considered a technique based on image-source clustering. Given a highly detailed model (represented as a triangle mesh) and the location of a sound source within it, we compute the image sources for all of the facets and group them with a wavelength-dependent clustering criterion to find specular reflection paths appropriate for different frequencies. Higher-order reflections can be found by mirroring the cluster centers and reclustering the resulting image sources. This is effectively equivalent to geometric simplification in "image-source space," and while not yet completely developed it seems to be a promising technique worthy of further work.

Overall, the demand for realistic virtual environments continues to grow, in particular from the computer-gaming community. With this growth comes the need for further advances in all steps of the acoustic-simulation pipeline, as well as the opportunity to leverage new results in diverse research areas such as three-dimensional geometry acquisition, wave-propagation modeling, and the perception of sound by human listeners. The desire for improvement, coupled with the limitations of current algorithms and systems, should provide the impetus for continued work toward better virtual-acoustic simulations for many years to come.

Bibliography

[1] W. Ahnert. *EASE Simulation Software Manual*. http://www.ada-acousticdesign.de/set_en/setsoft.html.

[2] J. B. Allen and D. A. Berkley. Image method for efficiently simulating small-room acoustics. *J. Acoust. Soc. Am.*, 65(4):943–950, 1979.

[3] J. Allred and A. Newhouse. Applications of the Monte Carlo method to architectural acoustics. *J. Acoust. Soc. Am.*, 30(1):1–3, 1958.

[4] J. Allred and A. Newhouse. Applications of the Monte Carlo method to architectural acoustics II. *J. Acoust. Soc. Am.*, 30(10):903–904, 1958.

[5] J. Amanatides. Ray tracing with cones. In *Proc. ACM Computer Graphics (SIGGRAPH'84)*, pages 129–135, 1984.

[6] F. Antonacci, M. Foco, A. Sarti, and S. Tubaro. Accurate and fast audio-realistic rendering of sounds in virtual environments. In *Proc. 2004 IEEE Workshop on Multimedia Signal Processing*, pages 271–274, Siena, 2004.

[7] F. Antonacci, M. Foco, A. Sarti, and S. Tubaro. Fast modeling of acoustic reflections and diffraction in complex environments using visibility diagrams. In *Proc. 12th European Signal Processing Conference (EUSIPCO '04)*, pages 1773–1776, 2004.

[8] F. Antonacci, M. Foco, A. Sarti, and S. Tubaro. Real time modeling of acoustic propagation in complex environments. In *Proc. 7th Intl. Conf. on Digital Audio Effects (DAFx'04)*, pages 274–279, Naples, 2004.

[9] F. Antonacci, M. Foco, A. Sarti, and S. Tubaro. Fast tracing of acoustic beams and paths through visibility lookup. *IEEE Trans. on Audio, Speech, and Language Processing*, 16(4):812–824, 2008.

[10] Audio Engineering Society. *Technical Committee on Audio for Games*. http://www.aes.org/technical/ag/.

[11] L. Aveneau, E. Andres, and M. Mériaux. The discrete tube: A spatial acceleration technique for efficient diffraction computation. In *Proc. 8th International Conference on Discrete Geometry for Computer Imagery (DGCI '99)*, pages 413–4246, 1999.

[12] C. A. Balanis. *Advanced Engineering Electromagnetics*. John Wiley and Sons, New York, 1989.

[13] M. Barron. *Auditorium Acoustics and Architectural Design*. E and FN Spon, London, 1998.

[14] P. Beckmann and A. Spizzichino. *The Scattering of Electromagnetic Waves from Rough Surfaces*. Artech House, 1987.

[15] L. Beranek. *Concert and Opera Halls: How They Sound*. Acoustical Society of America, Woodbury, NY, 1996.

[16] J. R. Berryhill. Diffraction response for nonzero separation of source and receiver. *Geophysics*, 42:1158–1176, 1977.

[17] M. Bertram, E. Deines, J. Mohring, J. Jegorovs, and H. Hagen. Phonon tracing for auralization and visualization of sound. In *Proc. IEEE Visualization 2005*, pages 151–158, 2005.

[18] M. A. Biot and I. Tolstoy. Formulation of wave propagation in infinite media by normal coordinates with an application to diffraction. *J. Acoust. Soc. Am.*, 29:381–391, 1957.

[19] J. Blauert, H. Lehnert, J. Sahrhage, and H. Strauss. An interactive virtual environment generator for psychoacoustic research. I: Architecture and implementation. *Acta Acustica united with Acustica*, 86(1):94–102, 2000.

[20] R. H. Bolt, P. E. Doak, and P. J. Westervelt. Pulse statistics analysis of room acoustics. *J. Acoust. Soc. Am.*, 22(3):328–340, 1950.

[21] J. Borish. Extension of the image model to arbitrary polyhedra. *J. Acoust. Soc. Am.*, 75:1827–1836, 1984.

[22] I. Bork. A comparison of room simulation software - The 2nd round robin on room acoustical computer simulation. *Acta Acustica united with Acustica*, 86(6):943–956, 2000.

[23] I. Bork. Simulation and measurement of auditorium acoustics - The round robins on room acoustical simulation. In *Proc. Inst. Acoust.*, volume 24(4), 2002.

[24] I. Bork. Report on the 3rd round robin on room acoustical computer simulation - Part I: Measurements. *Acta Acustica united with Acustica*, 91(4):740–752, 2005.

[25] I. Bork. Report on the 3rd round robin on room acoustical computer simulation - Part II: Calculations. *Acta Acustica united with Acustica*, 91(4):753–763, 2005.

[26] M. Born and E. Wolf. *Principles of Optics*. Macmillan Co., London, 2nd edition, 1964.

[27] D. Botteldooren. Finite-difference time-domain simulation of low-frequency room acoustic problems. *J. Acoust. Soc. Am.*, 98(6):3302–3308, 1995.

[28] J. Bowman and T. Senior. The Wedge. In J. Bowman, T. Senior, and P. Uslenghi, editors, *Electromagnetic and Acoustic Scattering by Simple Shapes*, chapter 6. Hemisphere Publishing Corporation, New York, 1969.

[29] C. A. Brebbia. *The Boundary Element Method for Engineers*. Pentech, 1984.

[30] J. H. Bremhorst. Impulse wave diffraction by wedges and plates. Master's thesis, Naval Postgraduate School, 1978.

[31] P. Calamia, B. Markham, and U. P. Svensson. Diffraction culling for virtual-acoustic simulations. *Acta Acustica united with Acusitca, Special Issue on Virtual Acoustics*, 94(6):907–920, 2008.

[32] P. Calamia and U. P. Svensson. Edge subdivision for fast diffraction calculations. In *Proc. 2005 IEEE Workshop on Applications of Signal Processing to Audio and Acoustics (WASPAA)*, pages 187–190, 2005.

[33] P. Calamia and U. P. Svensson. Culling insignificant diffraction components for interactive acoustic simulations. In *Proc. 19th Intl. Congress on Acoustics (ICA)*, Madrid, 2007.

[34] P. Calamia and U. P. Svensson. Fast time-domain edge-diffraction calculations for interactive acoustic simulations. *EURASIP Journal on Advances in Signal Processing, Special Issue on Spatial Sound and Virtual Acoustics*, 2007. Article ID 63560.

[35] P. Calamia, U. P. Svensson, and T. Funkhouser. Integration of edge-diffraction calculations and geometrical-acoustics modeling. In *Proc. Forum Acusticum*, pages 2499–2504, 2005.

[36] J. Chambers and Y. Berthelot. Time-domain experiments on the diffraction of sound by a step discontinuity. *J. Acoust. Soc. Am.*, 96(3):1887–1892, 1994.

[37] A. Chandak, C. Lauterbach, M. Taylor, Z. Ren, and D. Manocha. AD-Frustum: Adaptive frustum tracing for interactive sound propagation. *IEEE Trans. on Visualization and Computer Graphics*, 14:1707–1722, 2008.

[38] C. L. Christensen. *ODEON Room Acoustics Program ver. 8 Manual*. http://www.odeon.dk.

[39] D. Chu. Impulse response of density contrast wedge using normal coordinates. *J. Acoust. Soc. Am.*, 86(5):1883–1896, 1989.

[40] D. Chu. Exact solution for a density contrast shallow-water wedge using normal coordinates. *J. Acoust. Soc. Am.*, 87(6):2442–2450, 1990.

[41] D. Chu, T. Stanton, and A. Pierce. Higher-order acoustic diffraction by edges of finite thickness. *J. Acoust. Soc. Am.*, 122:3177–3194, 2007.

[42] R. D. Ciskowski and C. A. Brebbia, editors. *Boundary Element Methods in Acoustics*. Elsevier Applied Science, 1991.

[43] C. S. Clay and W. A. Kinney. Numerical computations of time-domain diffractions from wedges and reflections from facets. *J. Acoust. Soc. Am.*, 83:2126–2133, 1988.

[44] D. Cohen-Steiner, P. Alliez, and M. Desbrun. Variational shape approximation. *ACM Trans. Graph.*, 23(3):905–914, 2004.

[45] T. J. Cox, B.-I. Dalenbäck, P. D'Antonio, J. J. Embrechts, J. Y. Jeon, E. Mommertz, and M. Vorländer. A tutorial on scattering and diffusion coefficients for room acoustic surfaces. *Acta Acustica united with Acustica*, 92:1–15, 2006.

[46] T. J. Cox and Y. W. Lam. Evaluation of methods for predicting the scattering from simple rigid panels. *Applied Acoustics*, 40:132–140, 1993.

[47] T. J. Cox and Y. W. Lam. Prediction and evaluation of the scattering from quadratic residue diffusers. *J. Acoust. Soc. Am.*, 95(1):297–305, 1994.

[48] A. Craggs. A finite element method for free vibration of air in ducts and room with absorbing walls. *J. Sound Vib.*, 173(4):568–576, 1994.

[49] Creative Labs. *EAX*. http://www.soundblaster.com/technology/ welcome.asp?j1=eax.

[50] Creative Labs. *OpenAL*. http://connect.creativelabs.com/openal/default.aspx.

[51] L. Cremer and H. A. Müller. *Principles and Applications of Room Acoustics*. Applied Science Publishers, 1982.

[52] B.-I. Dalenbäck. *CATT-Acoustic v8 Manual*. http://www.catt.se/.

[53] B.-I. Dalenbäck. Room acoustic prediction based on a unified treatment of diffuse and specular reflection. *J. Acoust. Soc. Am.*, 100(2):899–909, 1996.

[54] B.-I. Dalenbäck, M. Kleiner, and U. P. Svensson. A macroscopic view of diffuse reflection. *J. Aud. Engr. Soc.*, 42:793–807, 1994.

[55] S. M. Dance, J. P. Roberts, and B. M. Shield. Computer prediction of sound distribution in enclosed spaces using an interference pressure model. *Applied Acoustics*, 44:53–65, 1995.

[56] J. Daniel. Spherical arrays for capturing 3D sound fields: Prototype measurements versus analytical models. In *Proc. 19th Intl. Congress on Acoustics (ICA)*, Madrid, 2007.

[57] J. Daniel, R. Mozeau, and S. Moureau. Further investigations of high order ambisonics and wavefield synthesis for holophonic sound imaging. In *Proc. 114th Aud. Eng. Soc. Conv.*, Amsterdam, 2003. Preprint no. 5788.

[58] A. Davis and R. Scharstein. The complete extension of the Biot-Tolstoy solution to the density contrast wedge with sample calculations. *J. Acoust. Soc. Am.*, 101:1821–1835, 1997.

[59] P. J. Davis and P. Rabinowitz. *Methods of Numerical Integration*. Academic Press, 2nd edition, 1984.

[60] N. de Rycker. Theoretical and numerical study of sound diffraction-application to room acoustics auralization. Rapport de stage D'Option scientifique, Ècole Polytechnique, Paris, France, 2002.

[61] E. Deines, M. Bertram, J. Mohring, J. Jegorovs, F. Michel, H. Hagen, and G. M. Nielson. Comparative visualization for wave-based and geometric acoustics. In *Proc. IEEE Visualization 2006*, pages 1173–1180, 2006.

[62] E. Deines, F. Michel, M. Bertram, H. Hagen, and G. M. Nielson. Visualizing the phonon map. In *Proc. Eurovis 2006*, pages 291–298, 2006.

[63] E. Deines, F. Michel, M. Hering-Bertram, J. Mohring, and H. Hagen. Simulation, visualization and virtual reality based modeling of room acoustics. In *Proc. 19th Intl. Congress on Acoustics (ICA)*, Madrid, 2007.

[64] Denon Records. *Anechoic Orchestral Music Recording*, 1995. Audio CD.

[65] J.-F. Dindart and C. Sémidor. Generalizing the reflection model by the use of a particle tracing method. In *First COST-G6 Workshop on Digital Audio Effects (DAFx'98)*, Barcelona, 1998.

[66] J. L. Dohner, R. Shoureshi, and R. J. Bernhard. Transient analysis of three-dimensional wave propagation using the boundary element method. *Intl. J. for Num. Methods in Engr.*, 24(3):621–634, 1987.

[67] I. Drumm and Y. Lam. The adaptive beam-tracing algorithm. *J. Acoust. Soc. Am.*, 107(3):1405–14112, 2000.

[68] R. Duraiswami, D. Zotkin, and N. Gumerov. Fast evaluation of the room transfer function using multipole expansion. *IEEE Trans. on Audio, Speech, and Language Processing*, 15(2):565–576, 2007.

[69] N. I. Durlach, R. W. Pew, W. A. Aviles, P. A. DiZio, and D. L. Zeltzer. Virtual environment technology for training (VETT). Report no. 7661, Bolt Beranek and Newman, Cambridge, MA, 1992.

[70] V. Easwaran and A. Craggs. On further validation and use of the finite element method to room acoustics. *J. Sound Vib.*, 187(2):195–212, 1995.

[71] T. F. W. Embleton. Line integral theory of barrier attenuation in the presence of the ground. *J. Acoust. Soc. Am.*, 67:42–45, 1980.

[72] J. J. Embrechts. Simulation of first and second order scattering by rough surfaces with a sound ray formalism. *J. Sound Vib.*, 229(1):56–87, 2000.

[73] J. Escolano, J. López, and B. Pueo. On the implementation of a room acoustics modeling software using finite-differences time-domain method. In *Proc. 122nd Aud. Engr. Soc. Conv.*, 2007. Paper Number 7090.

[74] C. F. Eyring. Reverberation time in "dead" rooms. *J. Acoust. Soc. Am.*, 1:217–241, 1930.

[75] A. Farina. Pyramid tracing vs. ray tracing for the simulation of sound propagation in large rooms. In *Proc. of Int. Conf. on Comput. Acoustics and its Environmental Applications (COMACO95)*, Southampton, 1995.

[76] A. Farina. RAMSETE - A new pyramid tracer for medium and large scale acoustic problems. In *Proc. Euro-Noise 95*, Lyon, 1995.

[77] A. Farina. Verification of the accuracy of the pyramid tracing algorithm by comparison with experimental measurements of objective acoustic parameters. In *Proc. 15th Intl. Congress on Acoustics (ICA)*, Trondheim, 1995.

[78] A. Farina. Introducing the surface diffusion and edge scattering in a pyramid-tracing numerical model for room acoustics. In *Proc. 108th Aud. Engr. Conv.*, Paris, 2000.

[79] C. Feuillade. Rapid computation of acoustic impulse scattering for rough penetrable surfaces. *Applied Acoustics*, 68:437–457, 2007.

[80] C. Feuillade, D. Chu, and C. S. Clay. Spacetime variations of the acoustic field scattered from a penetrable isovelocity wedge. *J. Acoust. Soc. Am.*, 116(2):777–789, 2004.

[81] H. Fouad. *SoundScape3D Software from VRSonic*. http://www.vrsonic.com/.

[82] E. R. Freniere, G. G. Gregory, and R. A. Hassler. Edge diffraction in Monte Carlo ray tracing. In *Proc. SPIE Optical Design and Analysis Software*, Denver, 1999.

[83] T. Funkhouser, I. Carlbom, G. Elko, G. Pingali, M. Sondhi, and J. West. A beam tracing approach to acoustic modeling for interactive virtual environments. In *Proc. ACM Computer Graphics (SIGGRAPH'98)*, pages 21–32, 1998.

[84] T. Funkhouser, P. Min, and I. Carlbom. Real-time acoustic modeling for distributed virtual environments. In *Proc. ACM Computer Graphics (SIGGRAPH'99)*, pages 365–374, 1999.

[85] T. Funkhouser, N. Tsingos, I. Carlbom, G. Elko, J. West, G. Pingali, P. Min, and A. Ngan. A beam tracing method for interactive architectural acoustics. *J. Acoust. Soc. Am.*, 115(2):739–756, 2004.

[86] A. C. Gade, M. Lisa, C. Lynge, and J. H. Rindel. Roman theatre acoustics: Comparison of acoustic measurement and simulation results from the Aspendos Theatre, Turkey. In *Proc. Proc. 18th Intl. Congress on Acoustics (ICA)*, Kyoto, 2004.

[87] M. Garland. Multiresolution modeling: Survey and future opportunities. In *Proc. Eurographics (State of the Art Report)*, pages 111–131, 1999.

[88] M. Garland and P. S. Heckbert. Surface simplification using quadric error metrics. In *Proc. ACM Computer Graphics (SIGGRAPH'97)*, pages 209–216, New York, NY, USA, 1997.

[89] E. D. Geest and H. Pätzold. Comparison between room transmission functions calculated with a boundary element method and a ray tracing method including phase. In *Proc. Internoise 96*, pages 3177–3180, 1996.

[90] M. Gensane and F. Santon. Prediction of sound fields in rooms of arbitrary shape: Validity of the image sources method. *J. Sound and Vibration*, 63(1):97–108, 1979.

[91] M. Gibbs and D. K. Jones. A simple image method for calculating the distribution of sound pressure levels within an enclosure. *Acustica*, 26(1):24–32, 1972.

[92] D. Giljohann. Mesh coarsening for the finite and the boundary element method in acoustics. *J. Comp. Acoust.*, 11(3):351–361, 2003.

[93] M. Gomes, S. Gerges, and R. Tenenbaum. On the accuracy of the assessment of room acoustics parameters using MLS technique and numerical simulation. *Acta Acustica united with Acustica*, 86(5):891–895, 2000.

[94] C. Goral, K. Torrance, D. Greenberg, and B. Battaile. Modeling the interaction of light between diffuse surfaces. In *Proc. ACM Computer Graphics (SIGGRAPH'84)*, pages 213–222, 1984.

[95] B. Gover, J. Ryan, and M. Stinson. Measurements of directional properties of reverberant sound fields in rooms using a spherical microphone array. *J. Acoust. Soc. Am.*, 116(4):1710–1720, 2004.

[96] J. Hargreaves and T. Cox. A transient boundary element method for room acoustics. In *Proc. 5th Intl. Postgrad. Res. Conf. of the Res. Inst. for the Built and Human Environment (BuHu)*, Salford, 2005.

[97] J. A. Hargreaves and T. J. Cox. A transient boundary element method model of Schroeder diffuser scattering using well mouth impedance. *J. Acoust. Soc. Am.*, 124(5):2942–2951, 2008.

[98] T. Hargreaves, T. J. Cox, Y. W. Lam, and P. D'Antonio. Surface diffusion coefficients for room acoustics: Free-field measures. *J. Acoust. Soc. Am.*, 108(4):1710–1720, 2000.

[99] N. Hattangady. Coarsening of mesh models for representation of rigid objects in finite element analysis. *Int. J. Numer. Meth. Eng.*, 44:313–326, 1999.

[100] P. Heckbert and P. Hanrahan. Beam tracing polygonal objects. *C*, 18(3):119–127, 1984.

[101] R. Heinz. Binaural room simulation based on an image source model with addition of statistical methods to include the diffuse sound scattering of walls and to predict the reverberant tail. *Applied Acoustics*, 38:145–159, 1993.

[102] F. J. Hilterman. Three-dimensional seismic modeling. *Geophysics*, 35(6):1020–1037, 1970.

[103] F. J. Hilterman. Amplitude of seismic waves - A quick look. *Geophysics*, 40:745–762, 1975.

[104] M. Hodgson. Evidence of diffuse surface reflections in rooms. *J. Acoust. Soc. Am.*, 89(2):765–771, 1991.

[105] M. Hodgson and E.-M. Nosal. Experimental evaluation of radiosity for room sound-field prediction. *J. Acoust. Soc. Am.*, 120(2):808–819, 2006.

[106] K. Hoshi, H. Toshiki, and K. Sekiguchi. Generating room shapes using elliptic Fourier descriptors for geometrical acoustic simulation. In *Proc. 19th International Congress on Acoustics (ICA)*, Madrid, September 2007.

[107] D. Immel, M. Cohen, and D. Greenberg. A radiosity method for non-diffuse environments. In *Proc. ACM Computer Graphics (SIGGRAPH'86)*, pages 133–142, 1986.

[108] International Standards Organization. *ISO Standard 3382: Acoustics - Measurement of the reverberation time of rooms with reference to other acoustical parameters*, 1997.

[109] International Standards Organization. *ISO Standard 17497-1: Acoustics - Sound-scattering properties of surfaces - Part 1: Measurement of the random-incidence scattering coefficient in a reverberation room*, 2004.

[110] G. Jebsen and H. Medwin. On the failure of the Kirchhoff assumption in backscatter. *J. Acoust. Soc. Am.*, 72(5):1607–1611, 1982.

[111] G. M. Jebsen. Acoustic diffraction by a finite barrier: Theories and experiments. Master's thesis, Naval Postgraduate School, 1981.

[112] M. Jedrzejewski and K. Marasek. Computation of room acoustics using programmable video hardware. In *Proc. Intl. Conf. on Computer Vision and Graphics (ICCVG)*, pages 587–592, Warsaw, 2004.

[113] H. W. Jensen. *Realistic Image Synthesis Using Photon Mapping*. A K Peters, 2001.

[114] Z. Jiang and X. Qiu. Receiving radius determination in ray-tracing sound prediction of rectangular enclosure. *J. Sound Vib.*, 301:391–399, 2007.

[115] H. G. Jonasson. Diffraction by wedges of finite acoustic impedance with applications to depressed roads. *J. Sound. Vib.*, 25(4):575–585, 1972.

[116] C. Joslin and N. Magnenat-Thalmann. Significant facet retrieval for real-time 3d sound rendering in complex virtual environments. In *VRST '03: Proc. ACM Symp. on Virtual Reality Software and Technology*, pages 15–21, Osaka, 2003.

[117] J. Kajiya. The rendering equation. In *Proc. ACM Computer Graphics (SIGGRAPH'86)*, volume 20, pages 143–150, 1986.

[118] B. Kapralos, M. Jenkin, and E. Milios. Sonel mapping: Acoustical modeling with an acoustical version of photon mapping. In *Proc. IEEE Intl. Workshop on Haptic Audio Visual Environments and their Applications (HAVE 2004)*, pages 1–6, 2004.

[119] B. Kapralos, M. Jenkin, and E. Milios. Sonel mapping: A stochastic acoustical modeling system. In *Proc. IEEE Intl. Conf. on Acoustics, Speech and Signal Processing (ICASSP 2006)*, pages 421–424, 2006.

[120] B. Kapralos, M. Jenkin, and E. Milios. Acoustical modeling with sonel mapping. In *Proc. 19th Intl. Congress on Acoustics (ICA)*, 2007.

[121] M. Karjalainen, P. Huang, and J. O. Smith. Digital waveguide networks for room response modeling and synthesis. In *Proc. 118 Aud. Engr. Soc. Conv.*, 2005. Paper Number 6394.

[122] T. Kawai. Sound diffraction by a many-sided barrier or pillar. *J. Sound Vib.*, 79(2):229–242, 1981.

[123] Y. Kawai. Calculation of a transient response in a rigid cubic room by using boundary integral equations - In connection with a benchmark problem in AIJ-BPCA. Tech. Report AA2005-28, Acoust. Soc. Jpn., 2005.

[124] Y. Kawai and T. Terai. A numerical method for the calculation of transient acoustic scattering from thin rigid plates. *J. Sound Vib.*, 141(1):83–96, 1990.

[125] R. S. Keiffer. On the validity of the wedge assemblage method for pressure-release sinusoids. *J. Acoust. Soc. Am.*, 93:3158–3168, 1993.

[126] R. S. Keiffer and J. C. Novarini. A time domain rough surface scattering model based on wedge diffraction: Application to low-frequency backscattering from two-dimensional sea surfaces. *J. Acoust. Soc. Am.*, 107:27–39, 2000.

[127] R. S. Keiffer, J. C. Novarini, and G. V. Norton. The impulse response of an aperture: Numerical calculations within the framework of the wedge assemblage method. *J. Acoust. Soc. Am.*, 95:3–12, 1993.

[128] R. S. Keiffer, J. C. Novarini, G. V. Norton, and J. R. Dubberley. Benchmarking the wedge assemblage method. *Math. Modell. Sci. Comput.*, 4:414–419, 1994.

[129] J. Keller. The scope of the image method. *Comm. Pure and App. Math.*, 6:595–512, 1953.

[130] J. Keller. Geometrical theory of diffraction. *J. Optical Soc. Am.*, 52(2):116–130, 1962.

[131] W. A. Kinney and C. S. Clay. The spatial coherence of sound scattered from a wind-driven surface: Comparison between experiment, Eckart theory and the facet-ensemble method. *J. Acoust. Soc. Am.*, 75:145–148, 1984.

[132] W. A. Kinney, C. S. Clay, and G. A. Sandness. Scattering from a corrugated surface: Comparison between experiment, Helmholtz-Kirchhoff theory, and the facet-ensemble method. *J. Acoust. Soc. Am.*, 73:183–194, 1983.

[133] J. Kirszenstein. An image source computer model for room acoustics analysis and electroacoustic simulation. *Applied Acoustics*, 17(4):275–290, 1984.

[134] M. Kleiner, B.-I. Dalenbäck, and U. P. Svensson. Auralization - An overview. *J. Audio Engr. Soc.*, 41(11):861–875, 1993.

[135] S. Kopuz and N. Lalor. Analysis of interior acoustic fields using the finite element method and the boundary element method. *Applied Acoustics*, 45:193–210, 1995.

[136] N. Korany, J. Blauert, and A. Alim. Acoustic simulation of rooms with boundaries of partially specular reflectivity. *Applied Acoustics*, 62(7):875–887, 2001.

[137] R. G. Kouyoumjian and P. H. Pathak. A uniform geometrical theory of diffraction for an edge in a perfectly conducting surface. In *Proc. IEEE*, volume 62, pages 1448–1461, 1974.

[138] Y. A. Kravtsov and Y. I. Orlov. On the validity conditions of the geometrical-optics method. In *Recent Problems of Propagation and Scattering of Waves*. Moscow, 1979.

[139] U. Kristiansen, A. Krokstad, and T. Follestad. Extending the image method to higher-order reflections. *Applied Acoustics*, 38:195–206, 1993.

[140] A. Krokstad, S. Strøm, and S. Sørsdal. Calculating the acoustical room response by the use of a ray-tracing technique. *J. Sound Vib.*, 8:118–125, 1968.

[141] A. Kulowski. Error investigation for the ray tracing technique. *Applied Acoustics*, 15(4):263–274, 1982.

[142] U. Kulowski. Algorithmic representation of the ray tracing technique. *Applied Acoustics*, 18:449–469, 1985.

[143] U. J. Kurze. Noise reduction by barriers. *J. Acoust. Soc. Am.*, 55(3):504–518, 1974.

[144] H. Kuttruff. A simple iteration scheme for the computation of decay constants in enclosures with diffusely reflecting boundaries. *J. Acoust. Soc. Am.*, 98(1):288–293, 1995.

[145] H. Kuttruff. Energetic sound propagation in rooms. *Acta Acustica united with Acustica*, 83:622–628, 1997.

[146] H. Kuttruff. *Room Acoustics*. Spon Press, 4th edition, 2000.

[147] K. H. Kuttruff. Auralization of impulse responses modeled on the basis of ray-tracing results. *J. Aud. Engr. Soc.*, 41(11):876–880, 1993.

[148] S. Laine, S. Slitanen, T. Lokki, and L. Savioja. Accelerated beam tracing algorithm. *Applied Acoustics*, 70(1):172–181.

[149] Y. W. Lam. A comparison of three diffuse reflection modeling methods used in room acoustics computer models. *J. Acoust. Soc. Am.*, 100(4):2181–2192, 1996.

[150] A. LeBot. A functional equation for the specular reflection of rays. *J. Acoust. Soc. Am.*, 112(4):1276–1287, 2002.

[151] A. LeBot and A. Bocquillet. Comparison of an integral equation on energy and the ray-tracing technique in room acoustics. *J. Acoust. Soc. Am.*, 108(4):1732–1740, 2000.

[152] H. Lee and B.-H. Lee. An efficient algorithm for the image model technique. *Applied Acoustics*, 24(2):87–115, 1988.

[153] E. Lehmann and A. Johansson. Prediction of energy decay in room impulse responses simulated with an image-source model. *J. Acoust. Soc. Am.*, 124(1):269–277, 2008.

[154] E. Lehmann, A. Johansson, and S. Nordholm. Reverberation-time prediction method for room impulse responses simulated with the image-source model. In *Proc. 2007 IEEE Workshop on Applications of Signal Processing to Audio and Acoustics (w)*, New Paltz, October 2007.

[155] H. Lehnert. Systematic errors of the ray-tracing algorithm. *Applied Acoustics*, 38:207–221, 1993.

[156] T. Lentz, D. Schröder, M. Vorländer, and I. Assenmacher. Virtual reality system with integrated sound field simulation and reproduction. *EURASIP Journal on Advances in Signal Processing, Special Issue on Spatial Sound and Virtual Acoustics*, 2007. Article ID 70540.

[157] T. Lewers. A combined beam tracing and radiant exchange computer model of room acoustics. *Applied Acoustics*, 38:161–178, 1993.

[158] S. Li, D. Chu, and C. Clay. Time-domain reflections and diffractions from facet-wedge constructions: Acoustic experiments including double diffractions. *J. Acoust. Soc. Am.*, 96(6):3715–3720, 1994.

[159] S. Li and C. Clay. Sound transmission experiments from an impulsive source near rigid wedges. *J. Acoust. Soc. Am.*, 84(6):2135–2143, 1988.

[160] T. Lokki and V. Pulkki. Measurement and theoretical validation of diffraction from a single edge. In *Proc. 18th International Congress on Acoustics (ICA), Vol. II*, pages 929–932, Kyoto, 2004.

[161] T. Lokki, V. Pulkki, and P. Calamia. Measurement and modeling of diffraction from an edge of a thin panel. *Applied Acoustics*, 69(9):824 – 832, 2007.

[162] T. Lokki, U. P. Svensson, and L. Savioja. An efficient auralization of edge diffraction. In *Proc. Aud. Engr. Soc. 21st Intl. Conf. on Architectural Acoustics and Sound Reinforcement*, pages 166–172, 2002.

[163] J. LoVetri, D. Mardare, and G. Soulodre. Modeling of the seat dip effect using the finite-difference time-domain method. *J. Acoust. Soc. Am.*, 100(4):2204–2212, 1996.

[164] A. Løvstad and U. P. Svensson. Diffracted sound field from an orchestra pit. *Acoustical Science and Technology*, 26(2):237–239, 2005.

[165] D. Luebke. A developer's survey of polygonal simplification algorithms. *IEEE Computer Graphics and Applications*, 21(3):24–35, 2001.

[166] T. M. Macdonald. A class of diffraction problems. *Proc. Lond. Math. Soc.*, 14:410–427, 1915.

[167] D. A. McNamara, C. W. I. Pistorius, and J. A. G. Malherbe. *Introduction to the Uniform Geometrical Theory of Diffraction*. Artech House, Boston, 1990.

[168] F. P. Mechel. Improved mirror source method in room acoustics. *J. Sound. Vib.*, 256:873–940, 2002.

[169] H. Medwin. Shadowing by finite noise barriers. *J. Acoust. Soc. Am.*, 69:1060–1064, 1981.

[170] H. Medwin, E. Childs, and G. M. Jebsen. Impulse studies of double diffraction: A discrete Huygens interpretation. *J. Acoust. Soc. Am.*, 72:1005–1013, 1982.

[171] P. Menounou, I. Busch-Vishniac, and D. Blackstock. Directive line source model: A new model for sound diffraction by half planes and wedges. *J. Acoust. Soc. Am.*, 107:2973–2986, 2000.

[172] P. Menounou and J. H. You. Experimental study of the diffracted sound field around jagged edge noise barriers. *J. Acoust. Soc. Am.*, 116:2843–2854, 2004.

[173] J. Merimaa and V. Pulkki. Spatial impulse response rendering I: Analysis and synthesis. *J. Aud. Engr. Soc.*, 53(12):1115–1127, 2005.

[174] J. Meyer and G. W. Elko. Spherical microphone arrays for 3D sound recording. In Y. Huang and J. Benesty, editors, *Audio Signal Processing for Next Generation Multimedia Communication Systems*, chapter 3, pages 67–90. Kluwer Academic Publishers, Boston, 2004.

[175] F. Michel, E. Deines, M. Hering-Bertram, M. Garth, and H. Hagen. Listener-based analysis of surface importance for acoustic metrics. In *Proc. IEEE Visualization*, Sacramento, 2007.

[176] Microsoft. *Microsoft Connect: XAudio 2*. http://connect.microsoft.com/XAudio2Beta.

[177] Microsoft. *Microsoft Developer Network: DirectSound*. http://msdn.microsoft.com/en-us/library/bb318665(VS.85).aspx.

[178] MIDI Manufacturers Association. *Interactive Audio Special Interest Group.* http://www.iasig.org/.

[179] J. R. Milner and R. J. Bernhard. An investigation of the modal characteristics of nonrectangular reverberation rooms. *J. Acoust. Soc. Am.*, 85(2):772–779, 1989.

[180] P. Min and T. Funkhouser. Priority-driven acoustic modeling for virtual environments. *Computer Graphics Forum*, 19(3):179–188, 2000.

[181] M. Monks, B. Oh, and J. Dorsey. Acoustic simulation and visualization using a new unified beam tracing and image source approach. In *Proc. Audio Engineering Society Convention*, pages 153–174, 1996.

[182] R. K. Morley and P. Shirley. *Realistic Ray Tracing.* A K Peters, 2003.

[183] R. T. Muehleisen and C. W. Beamer. Steady-state diffuse acoustic radiosity for sound level prediction in rooms. In *Proc. 2006 Architectural Engineering National Conference*, pages 1–14, Omaha, 2006.

[184] J. Mullen, D. M. Howard, and D. T. Murphy. Digital waveguide mesh modeling of the vocal tract acoustics. In *Proc. 2003 IEEE Workshop on Applications of Signal Processing to Audio and Acoustics (WASPAA)*, pages 119–122, 2003.

[185] D. Murphy and M. Beeson. Modeling spatial sound occlusion and diffraction effects with the digital waveguide mesh. In *Proc. Aud. Eng. Soc. 24th Intl. Conf.*, pages 207–216, Banff, 2003.

[186] D. Murphy, M. Beeson, S. Shelley, A. Southern, and A. Moore. RenderAIR - Room acoustics simulation using a hybrid digial waveguide mesh approach. In *Proc. 124th Aud. Eng. Soc. Conv.*, Amsterdam, 2008. Preprint no. 7429.

[187] D. Murphy and D. Howard. 2-D digital waveguide mesh topologies in room acoustics modeling. In *Proc. 3rd Int. Conf. Digital Audio Effects (DAFx'00)*, pages 211–216, 2000.

[188] D. Murphy, A. Kelloniemi, J. Mullen, and S. Shelley. Using the digital waveguide mesh. *IEEE Signal Processing Magazine*, 24(2):55–66, 2007.

[189] G. M. Naylor. ODEON - Another hybrid room acoustical model. *Applied Acoustics*, 38:131–143, 1993.

[190] G. V. Norton, J. C. Novarini, and R. S. Keiffer. An evaluation of the Kirchhoff approximation in predicting the axial impulse response of hard and soft disks. *J. Acoust. Soc. Am.*, 93(6):3049–3056, 1963.

[191] E.-M. Nosal, M. Hodgson, and I. Ashdown. Improved algorithms and methods for room sound-field prediction by acoustical radiosity in arbitrary polyhedral rooms. *J. Acoust. Soc. Am.*, 116(2):970–980, 2004.

[192] E.-M. Nosal, M. Hodgson, and I. Ashdown. Investigation of the validity of radiosity for sound-field prediction in cubic rooms. *J. Acoust. Soc. Am.*, 116(6):3505–3514, 2004.

[193] J. Novarini and R. Keiffer. Impulse response of a density contrast wedge: Practical implementation and some aspects of its diffracted component. *Applied Acoustics*, 58:195–210, 1999.

[194] J. C. Novarini and H. Medwin. Computer modeling of resonant scattering from a periodic assemblage of wedges: Comparison with electromagnetic theories of diffraction gratings. *J. Acoust. Soc. Am.*, 77:1754–1759, 1985.

[195] F. Oberhettinger. Diffraction of waves by a wedge. *Comm. Pure Appl. Math.*, 7(3):551–563, 1954.

[196] A. O'Donovan, R. Duraiswami, and D. Zotkin. Imaging concert hall acoustics using visual and audio cameras. In *Proc. IEEE Intl. Conf. on Acoustics, Speech, and Signal Processing (ICASSP)*, pages 5284–5287, Las Vegas, 2008.

[197] J. A. Ogilvy. *Theory of Wave Scattering from Random Rough Surfaces*. IOP Publishing Ltd., New York, 1991.

[198] N. Okamoto, R. Tomiku, T. Otsuru, T. Okuzono, and Y. Yasuda. Accuracy of large-scale finite element sound field analysis in rooms by use of a benchmark platform. In *Proc. Internoise*, Honolulu, 2006.

[199] A. Ondet and J. Barbry. Modeling of sound propagation in fitted workshops using ray tracing. *J. Acoust. Soc. Am.*, 85(2):787–796, 1989.

[200] T. Otsuru, Y. Uchinoura, R. Tomiku, N. Okamoto, and Y. Takahashi. Basic concept, accuracy and application of large-scale finite element sound field analysis of rooms. In *Proc. 18th Intl. Congress on Acoustics (ICA)*, Kyoto, 2004.

[201] D. Ouis. Scattering by a barrier in a room. *Applied Acoustics*, 56:1–24, 1999.

[202] D. Ouis. Scattering of a spherical wave by a thin hard barrier on a reflecting plane. *Applied Acoustics*, 59:19–66, 2000.

[203] D. Ouis. Diffraction by a hard half-plane: Useful approximations to an exact formulation. *J. Sound and Vibration*, 252(2):191–221, 2002.

[204] D. Ouis. Sound scattering by a hard half-plane: Experimental evidence of the edge-diffracted wave. *J. Sound and Vibration*, 252(3):469–477, 2002.

[205] D. Paini, J. H. Rindel, A. C. Gade, and G. Turchini. The acoustics of public squares/places: A comparison between results from a computer simulation program and measurements in situ. In *Proc. Internoise 2004*, Prague, 2004.

[206] M. Park and B. Rafaely. Sound-field analysis by plane-wave decomposition using spherical microphone array. *J. Acoust. Soc. Am.*, 118(5):3094–3103, 2005.

[207] A. D. Pierce. Diffraction of sound around corners and over wide barriers. *J. Acoust. Soc. Am.*, 55(5):941–955, 1974.

[208] A. D. Pierce. *Acoustics*. McGraw-Hill, New York, 1981.

[209] A. Pietrzyk. Computer modeling of the sound field in small rooms. In *Proc. Aud. Engr. Soc. 15th Intl. Conf. on Audio, Acoustics and Small Spaces*, pages 24–31, Copenhagen, 1998.

[210] J. R. Power. Measurement of absorption in rooms with sound absorbing ceilings. *J. Acoust. Soc. Am.*, 10:98–101, 1938.

[211] V. Pulkki, T. Lokki, and L. Savioja. Implementation and visualization of edge diffraction with image-source method. In *Proc. 112th Aud. Engr. Soc. Conv.*, Munich, 2002. Preprint no. 5603.

[212] N. Raghuvanshi and M. C. Lin. Interactive sound synthesis for large scale environments. In *ACM SIGGRAPH Symp. on Interactive 3D Graphics and Games (I3D)*, pages 101–108, 2006.

[213] S. Rasmussen and K. B. Rasmussen. On loudspeaker cabinet diffraction. *J. Aud. Engr. Soc.*, 42(3):147–150, 1994.

[214] J. H. Rindel and C. L. Christensen. Room acoustic simulation and auralization - How close can we get to the real room? In *Proc. 8th Western Pacific Acoustics Conference*, Melbourne, 2003.

[215] J. H. Rindel, S. H, C. L. Christensen, and A. C. Gade. Comparisons between computer simulations of room acoustical parameters and those measured in concert halls. In *Proc. of 137th Meeting of ASA, 2nd Convention of EAA, and 25th DAGA Conference*, Berlin, 1999.

[216] N. Röber, U. Kaminski, and M. Masuch. Ray acoustics using computer graphics technology. In *Proc. 10th Intl. Conf. on Digital Audio Effects (DAFx'07)*, pages 274–279, Bordeaux, 2007.

[217] H. Rushmeier and K. Torrance. Extending the radiosity method to include specularly reflecting and translucent materials. *ACM Transactions on Graphics*, 9(1):1–27, 1990.

[218] S. Sakamoto. Phase-error analysis of high-order finite difference time domain scheme and its influence on calculation results of impulse response in closed sound field. *Acoust. Sci. and Tech.*, 28:295–309, 2007.

[219] S. Sakamoto, H. Nagatomo, A. Ushiyama, and H. Tachibana. Calculation of impulse responses and acoustic parameters in a hall by the finite-difference time-domain method. *Acoust. Sci. and Tech.*, 29(4):256–265, 2008.

[220] S. Sakamoto, T. Seimiya, and H. Tachibana. Visualization of sound reflection and diffraction using finite difference time domain method. *Acoust. Sci. and Tech.*, 23:34–39, 2002.

[221] T. Sakuma and S. S. T. Otsuru. A benchmarking framework for wave-based computational methods in architectural acoustics. In *Proc. Proc. 18th Intl. Congress on Acoustics (ICA)*, pages 281–284, Kyoto, 2004.

[222] T. Sakuma, U. P. Svensson, A. Franck, and S. Sakamoto. A round-robin test program on wave-based computational methods for room-acoustic analysis. In *Proc. Forum Acusticum*, Sevilla, 2002.

[223] Y. Sakurai and K. Ishida. Multiple reflections between rigid plane panels. *J. Acoust. Soc. Jpn. (E)*, 3:183–190, 1982.

[224] Y. Sakurai and K. Nagata. Sound reflections of a rigid plane and of the "live end" composed by those panels. *J. Acoust. Soc. Jpn. (E)*, 2:5–14, 1981.

[225] J. Sandvad. Dynamic aspects of auditory virtual environments. In *Proc. 100th Aud. Engr. Soc. Conv.*, Copenhagen, 1996. Preprint 4226.

[226] L. Savioja, J. Backman, A. Järvinen, and T. Takala. Waveguide mesh method for low-frequency simulation of room acoustics. In *Proc. 15th Intl. Congress on Acoustics (ICA)*, pages 637–640, Trondheim, 1995.

[227] L. Savioja, J. Backman, A. Järvinen, and T. Takala. Improved discrete-time modeling of multi-dimensional wave propagation using the interpolated digital waveguide mesh. In *Proc. Int. Conf. on Acoustics, Speech and Signal Processing (ICASSP)*, pages 459–462, Munich, 1997.

[228] L. Savioja, J. Huopaniemi, T. Lokki, and R. Väänänen. Virtual environment simulation - Advances in the DIVA project. In *Proc. 3rd Intl. Conf. on Auditory Display (ICAD)*, pages 43–46, Palo Alto, 1997.

[229] L. Savioja, J. Huopaniemi, T. Lokki, and R. Väänänen. Creating interactive virtual auditory environments. *IEEE Comp. Graphics and Applications*, 22(4):49–57, 2002.

[230] L. Savioja, T. Lokki, and J. Huopaniemi. Auralization applying the parametric room acoustic modeling technique - the DIVA auralization system. In *Proc. 2002 Intl. Conf. on Auditory Display (ICAD)*, Kyoto, 2002.

[231] L. Savioja, T. J. Rinne, and T. Takala. Simulation of room acoustics with a 3-D finite difference mesh. In *Proc. Intl. Comp. Music Conf. (ICMC)*, Århus, 1994.

[232] L. Savioja and V. Välimäki. Interpolated rectangular 3-D digital waveguide mesh algorithms with frequency warping. *IEEE Trans. on Speech and Audio Processing*, 11:783–790, 2003.

[233] B. Schiettecatte, A. Nackaerts, and B. D. Moor. Real-time acoustics simulation using mesh-tracing. In *Proc. Intl. Comp. Music Conf. (ICMC)*, Singapore, 2003.

[234] O. Schmitz, S. Feistel, W. Ahnert, and M. Vorländer. Merging software for sound reinforcement systems and for room acoustics. In *Proc. 110th Aud. Eng. Soc. Conv.*, Amsterdam, 2001. Preprint no. 5352.

[235] D. Schröder and T. Lentz. Real-time processing of image sources using binary space partitioning. *J. Audio Eng. Soc.*, 54(7/8):604–619, 2006.

[236] M. R. Schroeder. Digital simulation of sound transmission in reverberant spaces. *J. Acoust. Soc. Am.*, 47(2):424–431, 1970.

[237] F. X. Sillion and C. Puech. *Radiosity and Global Illumination.* Morgan Kaufmann, 1994.

[238] S. Siltanen, T. Lokki, S. Kiminki, and L. Savioja. The room-acoustic rendering equation. *J. Acoust. Soc. Am.*, 122(3):1624–1635, 2007.

[239] S. Siltanen, T. Lokki, and L. Savioja. Geometry reduction in room acoustics modeling. In *Proc. Institute of Acoustics (IOA) 6th International Conference On Auditorium Acoustics*, pages 409–416, May 2006.

[240] S. Siltanen, T. Lokki, L. Savioja, and C. L. Christensen. Geometry reduction in room acoustics modeling. *Acta Acustica united with Acustica*, 94(3):410–418, 2008.

[241] J. O. Smith. Principles of digital waveguide models of musical instruments. In M. Kahrs and K. Brandenburg, editors, *Applications of Digital Signal Processing to Audio and Acoustics*, pages 417–466. Kluwer, Boston, 1998.

[242] A. Sommerfeld. Mathematical theory of diffraction. *Math. Ann.*, 47:317–374, 1896.

[243] E. Stavrakis, N. Tsingos, and P. Calamia. Topological sound propagation with reverberation graphs. *Acta Acustica united with Acustica - Special Issue on Virtual Acoustics (to appear)*, 2008.

[244] U. Stephenson. The sound particle simulation technique - An efficient prediction method for room acoustical parameters of concert halls. In *Proc. 86th Aud. Engr. Soc. Conv.*, Hamburg, 1989.

[245] U. Stephenson. Comparison of the mirror image source method and the sound particle simulation method. *Applied Acoustics*, 29:35–72, 1990.

[246] U. Stephenson. Quantized pyramidal beam tracing - A new algorithm for room acoustics and noise immission prognosis. *Acta Acustica united with Acustica*, 82(3):517–525, 1996.

[247] U. Stephenson and U. Kristiansen. Pyramidal beam tracing and time dependent radiosity. In *Proc. 15th Intl. Congress on Acoustics (ICA)*, pages 657–660, Trondheim, 1995.

[248] U. Stephenson and U. P. Svensson. An improved energetic approach to diffraction based on the Uncertainty Principle. In *Proc. 19th Intl. Congress on Acoustics (ICA)*, Madrid, 2007.

[249] J. S. Suh and P. A. Nelson. Measurement of transient response of rooms and comparison with geometrical acoustic models. *J. Acoust. Soc. Am.*, 105:2304–2317, 1999.

[250] J. Summers. *Reverberant acoustic energy in auditoria that comprise systems of coupled rooms*. PhD thesis, Rensselaer Polytechnic Institute, 2003.

[251] J. Summers, K. Takahashi, Y. Shimizu, and T. Yamakawa. Assessing the accuracy of auralizations computed using a hybrid geometrical-acoustics and wave-acoustics method (A). *J. Acoust. Soc. Am.*, 115(5):2514, 2004.

[252] J. E. Summers, R. R. Torres, Y. Shimizu, and B.-I. Dalenbäck. Adapting a randomized beam-axis-tracing algorithm to modeling of coupled rooms via late-part ray tracing. *J. Acoust. Soc. Am.*, 118(3):1491–1502, 2005.

[253] H. Suzuki, A. Omoto, and K. Fujiwara. Treatment of boundary conditions by finite difference time domain method. *Acoust. Sci. and Tech.*, 28:16–26, 2007.

[254] U. P. Svensson. Edge Diffration Toolbox for Matlab, 2006. http://www.iet.ntnu.no/˜svensson/Matlab.html.

[255] U. P. Svensson and P. Calamia. Edge-diffraction impulse responses near specular-zone and shadow-zone boundaries. *Acta Acustica united with Acustica*, 92(4):501–512, 2006.

[256] U. P. Svensson and P. Calamia. Edge diffraction in computer modeling of room acoustics (A). *J. Acoust. Soc. Am.*, 120:2998, 2006.

[257] U. P. Svensson, P. Calamia, and S. Nakanishi. Frequency-domain edge diffraction for finite and infinite edges. *Accepted for publication in Acta Acustica united with Acustica*, 2009.

[258] U. P. Svensson, R. I. Fred, and J. Vanderkooy. An analytic secondary source model of edge diffraction impulse responses. *J. Acoust. Soc. Am.*, 106:2331–2344, 1999.

[259] U. P. Svensson and K. Wendlandt. The influence of a loudspeaker cabinet's shape on the radiated power. In *Proc. Baltic Acoustic 2000, J. Vibroengineering*, pages 189–192, Vilnius, 200. 3(4).

[260] G. Taubin. Geometric signal processing on polygonal meshes. In *Proc. Eurographics (State of the Art Report)*, pages 81–96, 2000.

[261] E. Thorsos. The validity of the Kirchhoff approximation for rough surface scattering using a Gaussian roughness spectrum. *J. Acoust. Soc. Am.*, 83(1):78–92, 1988.

[262] R. Tomiku. Benchmark Platform on Computational Methods for Architectural/Environmental Acoustics, 2006. http://gacoust.hwe.oita-u.ac.jp/AIJ-BPCA/index.html.

[263] R. Torres. *Studies of edge diffraction and scattering: Applications to room acoustics and auralization*. PhD thesis, Chalmers University of Technology, Göteborg, Sweden, 2000.

[264] R. Torres, N. de Rycker, and M. Kleiner. Edge diffraction and surface scattering in concert halls: Physical and perceptual aspects. *J. Temporal Design in Architecture and the Environment*, 4:52–58, 2004.

[265] R. R. Torres, U. P. Svensson, and M. Kleiner. Computation of edge diffraction for more accurate room acoustics auralization. *J. Acoust. Soc. Am.*, 109:600–610, 2001.

[266] W. Trorey. A simple theory for seismic diffractions. *Geophysics*, 35:762–784, 1970.

[267] W. Trorey. Diffraction for arbitrary source receiver locations. *Geophysics*, 42:1177–1182, 1977.

[268] N. Tsingos, I. Carlbom, G. Elko, T. Funkhouser, and R. Kubli. Validation of acoustical simulations in the Bell Labs box. *IEEE Computer Graphics and Applications*, 22(4):28–37, 2002.

[269] N. Tsingos, C. Dachsbacher, S. Lefebvre, and M. Dellepiane. Extending geometrical acoustics to highly detailed architectural environments. In *Proc. 19th Intl. Congress on Acoustics (ICA)*, Madrid, September 2007.

[270] N. Tsingos, C. Dachsbacher, S. Lefebvre, and M. Dellepiane. Instant sound scattering. In *Proc. 18th Eurographics Symp. on Rendering (EGSR)*, July 2007.

[271] N. Tsingos, T. Funkhouser, A. Ngan, and I. Carlbom. Modeling acoustics in virtual environments using the Uniform Theory of Diffraction. In *Proc. ACM Computer Graphics (SIGGRAPH'01)*, pages 545–552, 2001.

[272] N. Tsingos, E. Gallo, and G. Drettakis. Perceptual audio rendering of complex virtual environments. *ACM Transactions on Graphics (Proc. SIGGRAPH)*, 23(3):249–258, 2004.

[273] N. Tsingos and J.-D. Gascuel. Acoustic simulation using hierarchical time-varying radiant exchanges. Unpublished tech. report, iMAGIS-GRAVIR/IMAG, 1997.

[274] N. Tsingos and J.-D. Gascuel. A general model for simulation of room acoustics based on hierarchical radiosity, 1997. Technical Sketches, SIGGRAPH 97 Visual Proceedings.

[275] N. Tsingos and J.-D. Gascuel. Soundtracks for computer animation: Sound rendering in dynamic environments with occlusions. In *Proc. Graphics Interface97*, Kelowna, BC, 1997.

[276] N. Tsingos and J.-D. Gascuel. Fast rendering of sound occlusion and diffraction effects for virtual acoustic environments. In *Proc. 104th Aud. Engr. Soc. Conv.*, 1998. Preprint no. 4699.

[277] K. van den Doel, D. Knott, and D. Pai. Interactive simulation of complex audiovisual scenes. *Presence: Teleoperators and Virtual Environments*, 13:99–111, 2004.

[278] S. Van Duyne and J. Smith. Physical modeling with the 2-D digital waveguide mesh. In *Proc. Intl. Comp. Music Conf. (ICMC)*, pages 40–47, Tokyo, 1993.

[279] D. van Maercke and J. Martin. The prediction of echograms and impulse responses within the Epidaure software. *Applied Acoustics*, 38:93–114, 1993.

[280] J. Vanderkooy. A simple theory of cabinet edge diffraction. *J. Aud. Eng. Soc.*, 39:923–933, 1991.

[281] M. Vorländer. Simulation of the transient and steady-state sound propagation in rooms using a new combined ray-tracing/image-source algorithm. *J. Acoust. Soc. Am.*, 86(1):172–178, 1989.

[282] M. Vorländer. International round robin on room acoustical computer simulation. In *Proc. 15th Intl. Congress on Acoustics (ICA)*, pages 577–580, Trondheim, June 1995.

[283] M. Vorländer. *Auralization: Fundamentals of Acoustics, Modelling, Simulation, Algorithms, and Acoustic Virtual Reality*. Springer-Verlag, 2008.

[284] M. Vorländer and E. Mommertz. Definition and measurement of random-incidence scattering coefficients. *Applied Acoustics*, 60:187–199, 200.

[285] G. Wadsworth and J. Chambers. Scale model experiments on the insertion loss of wide and double barriers. *J. Acoust. Soc. Am.*, 107(5):2344–2350, 2000.

[286] J. Wayman and J. Vanyo. Three-dimensional computer simulation of reverberation in an enclosure. *J. Acoust. Soc. Am.*, 62(1):213–215, 1977.

[287] E. W. Weisstein. Trilinear Coordinates. *MathWorld–A Wolfram Web Resource*. http://mathworld.wolfram.com/TrilinearCoordinates.html.

[288] E. Wenzel. Analysis of the role of update rate and system latency in interactive virtual acoustic environments. In *Proc. 103rd Aud. Engr. Soc. Conv.*, New York, 1997. Preprint 4633.

[289] E. Wenzel, J. Miller, and J. Abel. Sound Lab: A real-time, software-based system for the study of spatial hearing. In *Proc. 108th Aud. Engr. Soc. Conv.*, Paris, 2000.

[290] Z. Xiangyang, C. Ke'an, and S. Jincai. Modeling the sound fields in rooms with multiple sources using a hybrid image method including phase. *Acta Acustica united with Acustica*, 88:88–92, 2002.

[291] Z. Xiangyang, C. Ke'an, and S. Jincai. On the accuracy of the ray-tracing algorithms based on various sound receiver models. *Applied Acoustics*, 64:433–441, 2003.

[292] R. Yagel and J. Meeker. Priority-driven ray tracing. *Journal of Visualization and Computer Animation*, 8(1):17–32, 1997.

[293] W. Yang and M. Hodgson. Auralization study of optimum reverberation times for speech intelligibility for normal and hearing-impaired listeners in classrooms with diffuse sound fields. *J. Acoust. Soc. Am.*, 120(2):801–807, 2006.

[294] P. Zahorik, D. J. Kistler, and F. L. Wightman. Sound localization in varying virtual acoustic environments. In *Proc. 2nd Intl. Conf. on Auditory Display (ICAD)*, pages 179–186, Santa Fe, 1994.

[295] O. C. Zienkiewicz. *The Finite Element Method*. McGraw Hill, 1977.

[296] P. Zurek, R. Freyman, and U. Balakrishnan. Auditory target detection in reverberation. *J. Acoust. Soc. Am.*, 115(4):1609–1620, 2004.